Dissertation
submitted to the
Combined Faculties of the Natural Sciences and Mathematics
of the Ruperto-Carola-University of Heidelberg, Germany
for the degree of
Doctor of the Natural Sciences

Put forward by
Pavel Filianin
born in Saint-Petersburg, Russia

Oral examination: June 5, 2019

Measurements of low decay energies of beta-processes using Penning traps

Referees: Prof. Dr. Klaus Blaum
                     Priv.-Doz. Dr. Teresa Marrodan

Zusammenfassung

In der fundamentalen Physik gibt es zwei Themengebiete für die Nuklide mit niederenergetischen Betazerfällen besonders relevant sind: Die nukleare Astrophysik und die Neutrinophysik. Einige Grundzustands-Grundzustands Betazerfallsübergänge wurden mit Hilfe der Penningfallen-Massenspektrometerie (PT-MS) an den Experimenten SHIPTRAP (GSI, Darmstadt) und ISOLTRAP (CERN, Genf) vermessen.

Für die nukleare Astrophysik ist die Zerfallsenergie eines Nuklids eine wichtige spektroskopische Bestimmungsgröße. Im Falle des Nuklids ^{123}Te, das ausschließlich im s-Prozess entsteht, konnte gezeigt werden, dass die komplette Zerfallskette in einer heißen stellaren Umgebung durch präzise und genaue Messung der Zerfallsenergie rekonstruiert werden kann. Weiterhin wurde gezeigt, dass bei typischen Umgebungsbedingungen für den s-Prozess die Halbwertszeit für den Zerfall von ^{123}Te um viele Größenordnungen kleiner sein kann als bei erdähnlichen Umgebungsbedingungen. Diese Resultate können für Tests von astrophysikalischen Modellen in der Massenregion um $A = 123$ verwendet werden.

In der Neutrinophysik sind niederenergetische Betazerfälle für die Bestimmung der Restmasse des Neutrinos relevant. Die Zerfallsenergien (Q-Werte) von ^{131}Cs und ^{202}Pb wurden gemessen. Es wurde gezeigt, dass ^{202}Pb nicht für die Bestimmung der Neutrinomasse in Frage kommt da der Q-Wert zu hoch ist. In ^{131}Cs kann der vermessene Betazerfall ausgeschlossen werden da dieser energetisch nicht möglich ist. Der direkt gemessene Q-Wert von ^{187}Re konnte bestätigen, dass bei der erreichten Genauigkeit von 33 eV keine unerwarteten Unsicherheiten bei der kryogenen, mikrokalorimetrischen Messung (CM) des Betazerfallsspektrums von ^{187}Re auftreten. Eine gezielte Fragestellung der Neutrinophysik ist die Existenz von sterilen Neutrinos, speziell derer, die zur warmen Dunklen Materie beitragen. Hier wurde gezeigt, dass die Kombination von PT-MS und CM bei der Untersuchung von Elektroneinfangszerfällen bei einer Vielfalt von Nukliden zur Suche nach sterilen Neutrinos im keV Massenbereich beitragen kann.

Abstract

Two topics of fundamental physics are considered where nuclides with a low β-decay energy are of high interest, namely nuclear astrophysics and neutrino physics. A few relevant ground-to-ground β-transitions were addressed by Penning-trap mass spectrometry (PT-MS), employing the SHIPTRAP (GSI, Darmstadt) and ISOLTRAP (CERN, Geneva) facilities.

In nuclear astrophysics the decay energy of a nuclide is an important spectroscopic parameter. Thus, in the case of the pure s-process nuclide ^{123}Te, it was shown that when its decay energy is accurately and precisely known, the complete decay scheme in a hot stellar environment can be reliably reconstructed. It is shown that at typical s-process conditions the half-life of ^{123}Te can be by many orders of magnitude shorter than the terrestrial value. This circumstance may be used, for example, for tests of astrophysical models in the $A = 123$ mass region.

In neutrino physics, low-energy β-transitions can be used for determination of the neutrino rest mass. The decay energies (Q-values) of ^{131}Cs and ^{202}Pb were determined. It turned out that the nuclide ^{202}Pb can hardly be used for the neutrino mass determination due to its too high Q-value, whereas ^{131}Cs can be confidently excluded from the consideration since the examined β-transition is energetically forbidden. The directly measured Q-value of ^{187}Re has shown that on the level of our present accuracy of 33 eV there are no unexpected systematic effects inherent in cryogenic microcalorimetry (CM), which was used for the β^--spectra acquisition of ^{187}Re. A specific problem in neutrino physics is the existence of sterile neutrinos, especially those which can contribute to the so-called Warm Dark Matter. It is shown that the combined efforts of PT-MS and CM may contribute to the keV sterile neutrino search in electron capture in a variety of nuclides.

Contents

1. Introduction

In this introductory chapter a few topics of fundamental physics, where nuclides with a low β-decay[1] energy play an important role, are highlighted. Penning-trap mass spectrometry (PT-MS) is also introduced as the method of choice for the β-decay energy determination.

To give a feeling of what "low" energy is, Fig. 1.1 is given, where all the experimentally known ground-to-ground β-decay energies are shown [1]. Most of the cases have decay energies of about few MeV. However, there is a fraction of nuclides whose decay energy significantly deviates from the global trend. In the framework of this thesis we consider only those cases which decay with relatively low energy, namely below 100 keV [2]. Nuclides in this particular decay energy range can be utilized for the absolute neutrino mass search, and/or have to be carefully treated in the stellar nucleosynthesis network.
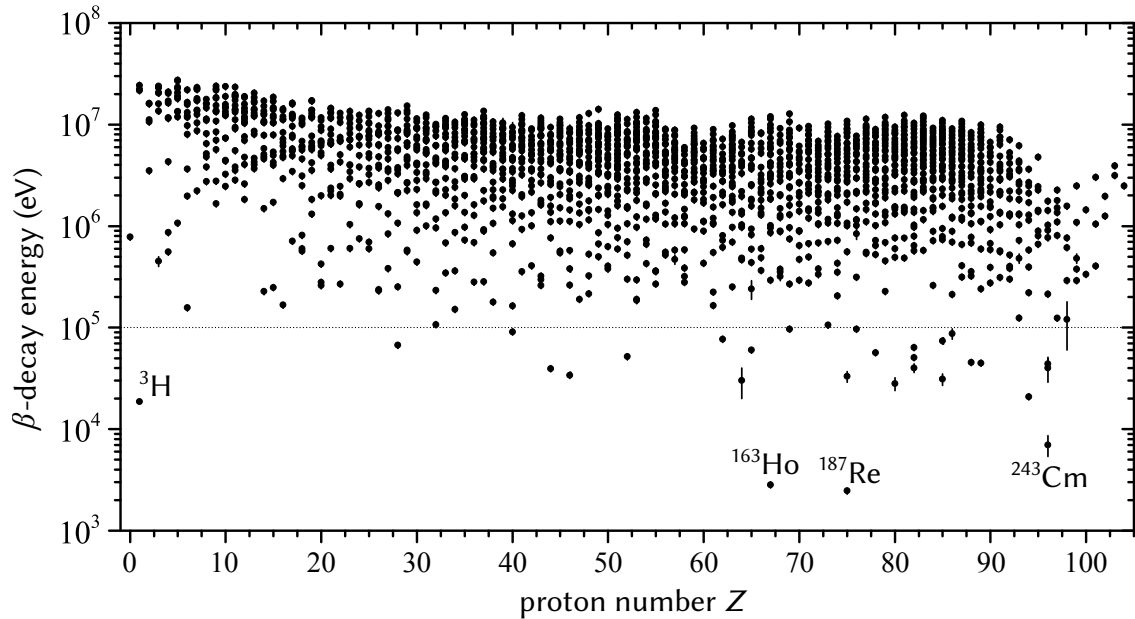
Figure 1.1: Decay energies of all experimentally known ground-to-ground β-transitions. Data is taken from [1].

Primarily it is also worth clarifying the mass-to-energy relation $E = mc^2$, since it will be intensively used within the scope of the thesis. Einstein's famous formula states that

---

[1]There are three main types of weak decay of nuclei, namely β^--decay, β^+-decay and electron capture, but where it is not necessary to distinguish between them it is simply said β-decay.

[2]In general, it is not necessary to be ground-to-ground, but can also be ground-to-excited state transition, which, however, are not shown in Fig. 1.1.

the equivalent energy E can be calculated as the mass m multiplied by the speed of light c squared. In nuclear physics, the conventional energy unit is an electron-Volt (eV). It means that the mass unit is now electron-Volt over the speed of light squared (eV/c^2). However, where it does not cause any ambiguity, the coefficient c^2 is omitted and it is simply said that the mass is in eV units.

1.1 Neutrino physics with low-energy β-processes

Neutrino physics has provided very impressive progress in our understanding of particle physics during recent years. These advances are of primary relevance for a better description of neutrino properties, and presumably they also contain profound implications in the general picture of fundamental interactions and their connections with astrophysics and cosmology. The central role of neutrinos is even more evident when considering that neutrino masses require physics beyond the Standard Model. At present, however, we do not have a clear picture of such new physics and its energy scale.

One of the most intriguing questions in elementary particle physics is the neutrino rest mass[1]. The neutrino rest mass is the key feature not only in particle physics, but also in astrophysics and cosmology, being an essential ingredient to answering the question of the neutrino mass generation mechanism, and an important input parameter to reduce degeneracies in cosmological models.

The neutrino was introduced by Wolfgang Pauli in 1930 as a hypothetical non-charged and presumably very light particle in order to conserve energy, momentum, and angular momentum in β-decay, and therefore naturally explaining a continuous β-decay spectrum. Due to its very small interaction cross section with matter the existence of the neutrino was experimentally proven only in 1956 [2]. It took another few decades in order to show and prove the existence of three different neutrino kinds – flavors.

Investigations of neutrinos from the Sun [3] and of neutrinos created in the atmosphere by cosmic rays [4], have given first strong evidence for massive neutrinos indicated by neutrino oscillations. Additionally, investigations of accelerator, reactor and geo neutrinos also contributed to a better understanding of the neutrino physics. In 2015 the Nobel Prize in physics was jointly awarded to Takaaki Kajita and Arthur B.McDonald for their key contributions to the experiments which demonstrated that neutrinos change identities.

Neutrino oscillations imply that a neutrino from one specific weak interaction flavor, e.g. an electron neutrino ν_e, transforms into another weak flavor eigenstate, i.e. a muon neutrino ν_μ or a tau neutrino ν_τ, while traveling from the source to the detector. Consequently, the existence of neutrino oscillations requires a non-trivial mixing between the weak interaction eigenstates $(\nu_e, \nu_\mu, \nu_\tau)$ and the corresponding neutrino mass states $(m_{\nu_e}, m_{\nu_\mu}, m_{\nu_\tau})$ and, moreover, that the mass eigenvalues (m_1, m_2, m_3) differ from each other. In other words, the neutrino ν_α, created with flavor α in a weak interaction process, is a quantum superposition

---

[1]Here it is worth noting that throughout this paper, the mass of a neutrino and the mass of an antineutrino is not distinguished, because it should be the same if the CPT theorem holds. Therefore, the common term "neutrino" is used when speaking of neutrinos and of antineutrinos, and they will be explicitly distinguished only where it is necessary.

of the neutrino mass eigenstates ν_i:

$$|\nu_\alpha\rangle = \sum_i U_{\alpha i}|\nu_i\rangle, \tag{1.1}$$

where index $\alpha = \{e, \mu, \tau\}$ marks three known kinds of the active[1] flavor neutrinos ν_e, ν_μ and ν_τ. The index $i = \{1,2,3\}$ denotes the individual neutrino mass eigenstates with mass m_i, and $U_{\alpha i}$ are the elements of the Pontecorvo-Maki-Nakagawa-Sakata neutrino mixing matrix [5].

Unfortunately, oscillation experiments can't give absolute neutrino masses m_{ν_α}[2], but only yield the differences of squares of the neutrino masses $\Delta m^2_{\nu_{\alpha\beta}} = m^2_{\nu_\alpha} - m^2_{\nu_\beta}$ or at least their absolute values $|\Delta m^2_{\nu_{\alpha\beta}}|$. Since experimentally measured $|\Delta m^2_{\nu_{\alpha\beta}}|$ values do not equal zero, it means that at least two neutrino mass eigenvalues are nontrivial (nonzero). Consequently, the mass ordering is also unknown and all three options are likely: $m_1 < m_2 < m_3$ – the normal hierarchy, $m_3 < m_1 < m_2$ – the inverted hierarchy, or $m_1 \simeq m_2 \simeq m_3$ – the quasi-degenerate hierarchy. Discrimination between these possible mass scenarios thus requires a sub-eV sensitivity to the absolute neutrino mass. In addition, the key role of neutrino masses in understanding which of the possible extensions or new theories beyond the Standard Model is correct [6, 7] makes the quest for the absolute value of the neutrino mass one of the most urgent questions of nuclear and particle physics.

Neutrinos are produced by weak interactions, therefore the neutrino mass can be determined by investigation of the kinematics of weak decays. The kinematic method is essentially based on energy and momentum conservation only, and thus is model-independent. However, in any search for the kinetic neutrino mass, neutrino energy should be as small as possible, otherwise the effect of relativity hides the mass. That's why low-energy β-decay nuclides are highly demanded for the absolute neutrino mass search. Basics of the kinematic neutrino mass determination and the search for relevant nuclides are given in the dedicated Chapter 2.

1.2 Nuclear astrophysics in connection to low-energy β-processes

More than half a century has passed since the foundation of nuclear astrophysics. Since then, this discipline has reached its maturity. Today, nuclear astrophysics constitutes a multidisciplinary crucible of knowledge that combines the achievements in theoretical astrophysics, observational astronomy, cosmochemistry, atomic and nuclear physics. New tools and developments have revolutionized our understanding of the origin of the elements: supercomputers have provided astrophysicists with the required computational capabilities to study the evolution of stars in a multidimensional framework; the emergence of high-energy astrophysics with space-borne observatories has opened new windows to observe the Universe; cosmochemists have isolated tiny pieces of stardust embedded in primitive meteorites, giving clues on the processes operating in stars; and nuclear physicists have widely measured

---

[1]As will be described in Sec. 2.3, an additional fourth eigenstate - sterile neutrino - has been suggested to explain anomalies resulted from several oscillation experiments and cosmological observations.

[2]Actually they are effective mass values, however we will omit the word "effective" below.

spectroscopic data such as nuclear reactions cross sections, nuclear level structures, nuclear decay energies, half-lives and masses.

In general, nuclear astrophysics requires the development of hypotheses and models that describe what happens deep inside stars and stellar explosions. These models must then be compared with data to determine whether they indeed reflect what happens in nature. Without such model validation, progress is not possible. The challenge is that the data on stellar interiors cannot be obtained directly. In most cases only a limited amount of radiation from the stellar surfaces or the debris of the explosion can be measured. Nuclear physics opens a unique validation path for astrophysical models by linking such observables to the conditions in the deep interiors. This is done by exploiting the strong dependence of nuclear processes on temperature, density, and composition, but requires accurate nuclear spectroscopic data. Once the nuclear physics is fixed, observables related to nuclear processes can be used to validate or falsify stellar models. Thus, the key parameter of nuclear astrophysics is the accurate and precise nuclear spectroscopic data, which can be achieved in the corresponding laboratory experiments.

Stellar nucleosynthesis starts with ^{12}C and ^{16}O produced during H and He burning. In subsequent stages of stellar evolution, the light elements up to the mass region 50 are produced by charged particle reactions during C, Ne, and O burning [8]. Ultimately, Si burning leads to very high temperatures so that only the most stable nuclei around Fe are abundantly produced [9], giving rise to the outstanding abundance maximum at $A = 56$. From this point on, further build-up of heavier nuclei by charged particle reactions ceases due to the increasing Coulomb barriers and the decreasing binding energies per nucleon. All remaining abundances up to the actinides are essentially shaped by neutron capture nucleosynthesis. The concept of neutron capture reactions in stars as the origin of the heavy elements has been first formulated in the fifties by Burbidge, Burbidge, Fowler and Hoyle (shortly B^{2}FH) [10] with the distinction of a slow and a rapid process.

For the slow neutron capture process (s-process) the time scale for β-decay of unstable isotopes is generally shorter than that of neutron captures. S-process elements are created when iron peak elements capture free neutrons. When reaching an unstable isotope, β-decay forms a nucleus of another element with one more proton and one less neutron. Therefore the s-process path runs close to the valley of stability and creates stable target nuclei along this path. The low neutron densities which are required to meet the conditions for the s-process are approximately $n \approx 10^7 \mathrm{cm}^{-3}$ to $10^{10} \mathrm{cm}^{-3}$ [11] and take place on a long time-scale, ranging from 100 to $\sim 10^5$ years.

The rapid neutron capture process (r-process) on the other hand, is characterised by neutron densities higher than $10^{20} \mathrm{cm}^{-3}$ on a very short time-scale, $\sim 0.01 - 10$ sec [12]. These have the effect that the time scale of a successive neutron capture of an unstable isotope is shorter than the one of its β-decay. However, the high temperature phase of the r-process and other explosive processes have nothing to do with the low-energy β-decay nuclides studied within the scope of this thesis and are mentioned here only for the completeness.

Naturally, the s-process is more easily accessible to laboratory experiments as well as to stellar models and astronomical observations [13]. The main nuclear physics input for

s-process studies are the (n,γ) cross sections of all nuclei along the reaction path from Fe to Bi as well as the β-decay rates at the branching points. As the s-process capture path follows the valley of β-stability, the neutron capture cross sections of most of the involved nuclei can be measured experimentally. The advent of suited accelerators and detector technologies led to the present situation where the stellar (n,γ) rates for s-process applications start to be reliable enough for interpreting the observed abundance patterns as a critical test for models of stellar helium burning. But still further improvements are definitely needed for the (n,γ) cross sections of radioactive branching nuclides.

The second necessary ingredient for s-process flow determination is the half-lives or β-decay rates λ_β. When the neutron capture rate λ_n becomes comparable to the β-decay rate $(\lambda_n \approx \lambda_\beta)$, the resulting competition leads to branchings in the s-process nucleosynthesis path. Thus, β-decay rates of all possible branching nuclides have to be measured. Nowadays, the ground state β-decay rates of many necessary nuclides are well known owing to a variety of modern techniques and methods. However, for some nuclides the β-decay rates measured in terrestrial experiment may significantly deviate from the stellar ones. Indeed, nuclides, which are exposed to high temperatures and densities in a stellar plasma, may experience a dramatic change of their decay rate. This idea was formulated for the first time by Cameron [14] and was detailed later in [15, 16]. The changes result from different effects related to the thermal population of excited nuclear states in the hot photon bath or through atomic effects in the highly ionized, dense stellar plasma. These effects make weak-interaction rates in the stellar interior sensitive functions of temperature and density, especially for those nuclides which have low β-decay energies in terrestrial conditions. Thereby, direct highly accurate β-decay energy measurements of relevant nuclides are necessary, being a crucial ingredient for the reliable predictions of the β-decay rates in a stellar medium, and therefore for the s-process flow determination. More details concerning the low energy β-decay nuclides involved into s-process can be found in the dedicated Chapter 3.

1.3 Penning-trap mass spectrometry

Since our interest is focused on the nuclides with the low β-decay energies, the determination of these energies with high accuracy faces many difficulties if extracted from the decay spectra. Although the analysis of the decay spectra may give a highly precise decay energy value, however not accurate. In the scope of the PT-MS it is important to distinguish the terms accuracy and precision. A measured value can have high precision (low statistical uncertainty), but may be shifted relative to the true value (may have a systematic offset). Thus, a performed measurement can be precise but not accurate. PT-MS is one of the most straightforward methods and, if carefully applied, gives both high accuracy and precision [17]. The accuracy is basically secured by the comparison (direct or indirect) of the PT-MS outputs with ^{12}C nuclide, which is a mass standard by definition.

A Penning trap is a tool where confinement of the charged particles is founded on the superposition of a strong homogeneous magnetic field, providing radial confinement, and a weak electrostatic quadrupole field, providing axial confinement. The reason for the

outstanding opportunities of a Penning trap is that a charged particle (an ion) can be confined in a tiny volume for a very long time. Furthermore, the mass measurement method is based on a fundamental cyclotron principle: in a uniform magnetic field the cyclotron frequency of a particle is proportional to its charge-to-mass ratio. Thus, provided that the charge and the magnetic field are known, by measuring the cyclotron frequency the mass of the particle can be directly derived. In Chapter 4 the basics of PT-MS are introduced.

The goal of the current research is to measure the energy release of dedicated β-decaying nuclides in the straightforward way: as the mass difference between parent and daughter atoms using PT-MS. Generally, Penning-trap methods and technology have been making steady progress. Nowadays there are about 10 Penning trap systems which are involved in precision tests of fundamental physics. Each Penning-trap system has its own technical features and limitations and is usually attributed to a certain part of the nuclear chart to be investigated, but all together they cover a very wide range of fundamental problems. The choice of the facility for the current mass measurements of the dedicated case was based on the ability to achieve necessary precision and/or the accessibility of the ions of interest. The high precision decay energy measurement $\Delta M/M < 5 \cdot 10^{-10}$ of ^{123}Te, ^{163}Ho and ^{187}Re were performed using the off-line version of the mass spectrometer SHIPTRAP at GSI (see Chapter 5), while the moderate precision $1.5 \cdot 10^{-9} < \Delta M/M < 2 \cdot 10^{-8}$ was achieved using the on-line mass spectrometer ISOLTRAP at CERN (see Chapter 6).

2. Search for the absolute neutrino mass

The compelling evidence for non-zero neutrino masses from atmospheric, solar and reactor neutrino experiments - as briefly discussed in Sec. 1.1 - provides squared neutrino mass differences, but not the absolute neutrino masses. Three main approaches to determine the absolute neutrino mass with the focus on the kinematic method, where low-energy β-decay transitions are of the primary interest, are considered in the following.

1) Cosmology. The Big Bang has left over a dense, blackbody radiation of so-called relic neutrinos, similar to the cosmic microwave background. These neutrinos cooled down by adiabatic expansion over time to a temperature of about 2.7 K and populate the Universe with an average density of 339 cm^{-3} [18]. Due to the large abundance of relic neutrinos and their low masses they act as hot dark matter: neutrinos have smeared out fluctuations at small scales. This smearing effect depends on the sum of the neutrino mass eigenstates

$$\Sigma m_i \equiv \sum_{i=1}^{3} m_i. \tag{2.1}$$

Up to now, a combination of cosmological probes set the limit of $\Sigma m_i < 120$ meV (95% C.L.) [19]. Future experiments aim to reach an uncertainty level of $\delta m_{\nu_e} = 21$ meV [20]. However, this will not be a measurement of the neutrino mass, but a result from fitting a model with many parameters, of which some have not yet even found a physical explanation. Thus, it is important to note, that the neutrino mass determination results based on cosmological observations are indirect and highly dependent on the underlying cosmological model.

2) Neutrinoless double β-decay. Neutrinoless double β-decay ($0\nu\beta\beta$) is a forbidden decay in the Standard Model of particle physics, but it could exist in case neutrinos are their own antiparticles (so called Majorana particles). Its discovery would be a direct observation of lepton number violation and could yield information on the neutrino mass. The decay rate scales with the absolute square of the so-called effective Majorana neutrino mass:

$$m_{\beta\beta}^2 \equiv \left| \sum_{i=1}^{3} U_{ei}^2 m_i \right|^2, \tag{2.2}$$

which takes into account the neutrino mixing matrix elements. Assuming that the $0\nu\beta\beta$ decay proceeds dominantly via the emission and subsequent absorption of a virtual neutrino, the decay rate $\Gamma_{0\nu\beta\beta}$ can be expressed as

$$\Gamma_{0\nu\beta\beta} = G_{0\nu\beta\beta} |M_{0\nu\beta\beta}|^2 m_{\beta\beta}^2, \tag{2.3}$$

where $G_{0\nu\beta\beta}$ is the exactly calculable kinematic factor, in contrast to the value of the nuclear matrix element (NME) $|M_{0\nu\beta\beta}|^2$, which depends on the applied nuclear model. The $0\nu\beta\beta$ decay has not been observed yet, and the best limits on $m_{\beta\beta}$ have been obtained in experiments with ^{76}Ge, ^{100}Mo, ^{130}Te and ^{136}Xe. The author of [21] made a brief review of all known so far results on $m_{\beta\beta}$ experiments and in combination with the most reliable NME have set the present conservative limit as $m_{\beta\beta} < 0.24$ eV.

3) Direct Neutrino Mass Determination. The direct neutrino mass determination is based purely on kinematics without further assumptions. Essentially, the neutrino mass is determined by using the relativistic energy-momentum relationship

$$E^2 = p^2 + m^2 \tag{2.4}$$

and therefore it is sensitive to the neutrino mass squared $m_{\nu_e}^2$. In principle there are two methods: time-of-flight measurements and precision investigations of weak decay spectra. The former requires very long baselines and consequently very strong sources, which only cataclysmic astrophysical events like a core-collapse supernova could provide. The supernova explosion SN1987a in the Large Magellanic Cloud gave the limit of 5.8 eV (95% C.L.) [22]. However, nearby supernovae are rare and the neutrino emission characteristics depend somewhat on the underlying supernova model. Therefore, aiming for this sensitivity, the investigation of the kinematics of weak decays and more explicitly the investigation of the endpoint region of a β-decay spectrum (or an electron capture) is still the most sensitive model independent and direct method to determine the neutrino mass. Here the neutrino is not observed but the decay products are precisely measured. Using energy and momentum conservation, the neutrino mass can be obtained. In case of the investigation of a β-spectrum usually the "averaged" or "effective" electron neutrino mass m_{ν_e} is determined[1]

$$m_{\nu_e}^2 \equiv \sum_{i=1}^{3} |U_{ei}|^2 m_i^2. \tag{2.5}$$

It is worth noting the important difference between the composition of the masses m_{ν_e} (Eq. (2.5)) and $m_{\beta\beta}$ (Eq. (2.2)) presented in single and neutrinoless double β-decay, respectively: in the former case we measure an incoherent and unresolved sum of mass eigenstates m_i each leading with probability $|U_{ei}|^2$, whereas in the latter case a coherent sum of these masses with unknown phases is measured. If non-zero neutrino masses m_{ν_e} and $m_{\beta\beta}$ are found both in single β-decay and in neutrinoless double β-decay, respectively, their difference could be used to gain information on the Majorana phases, which are otherwise not accessible [23].

Hereby, the determination of the absolute neutrino mass via kinematic method based on the investigation of the endpoint region of a β-decay spectrum is the straightforward and least model-dependent approach. The overview of this approach is done in the following section.

---

[1]In order to measure the individual neutrino mass eigenstates m_i the instrumental resolution have to be better than the mass difference Δm_i between them, which is not feasible in the near future.

2.1 Kinematic determination of the neutrino mass

Kinematic determination of the neutrino mass means the investigation of kinematics of weak decays, i.e. measurement of the decay products of weak decays. For the masses of ν_μ and ν_τ the measurements have yielded the following upper limits [24]: $m_{\nu_\mu} < 190$ keV (90% C.L.) and $m_{\nu_\tau} < 18.2$ MeV (95% C.L.). The reason why this limit is so much higher than the uncertainties of the input parameters (mass and momentum of muon or tauon), is the trivial consequence of relativistic kinematics, namely, of the quadratic form of the energy–momentum relation (see Eq. (2.4)). Therefore, the given input uncertainties of neutrino energy ΔE_ν and momentum Δp_ν have to be scaled up with the full energy E_ν and momentum p_ν, when calculating the uncertainty of the derived neutrino mass squared:

$$\Delta m_\nu^2 \approx \Delta E_\nu^2 + \Delta p_\nu^2 \approx 2E_\nu \Delta E_\nu + 2p_\nu \Delta p_\nu. \tag{2.6}$$

In any search for a kinetic neutrino mass, neutrino energy should, therefore, be as small as possible, otherwise relativity hides the mass. This argument favours the search for the electron neutrino mass m_{ν_e} in low-energy nuclear β-decays by many orders of magnitude as compared with the case of the other neutrino flavours. However, any decay rate into neutrinos shrinks with their phase space density and hence with their energy squared (see Eq. (2.8)). In between these two poles little space is left, and tremendous effort will be required to reach sub-eV sensitivity on neutrino mass using the kinematic approach.

There are three types of single β-decay, namely β^+, β^- and electron capture (EC), but usually only β^- and EC are considered for kinematic determination of the neutrino mass. The reason is that β^--decay and EC processes are energetically allowed when $Q > 0$ (parent atom is just heavier then its daughter)[1], while β^+-decay can occur only if $Q > 2m_e$. The accurate investigation of a β^+-spectrum would be hampered by the strong background from the competing EC process. Thus, in the following only β^--decay and EC are introduced[2].

2.1.1 β^--decay

The β^--decay process is characterized by

$$(A,Z) \rightarrow (A,Z+1)^+ + e^- + \tilde{\nu}_e. \tag{2.7}$$

The released surplus energy Q_β is shared in a statistical way between the kinetic energy of the emitted electron e^- and anti-neutrino $\tilde{\nu}_e$, and a diminutive recoil energy of the daughter atom. The Q_β-value is given by the mass difference $\Delta M = M(A,Z) - M(A,Z+1)$ between the *neutral* mother and daughter atoms. The energy spectrum of the electrons is given by the well known Fermi theory of β-decay [25]:

$$\frac{\partial N}{\partial E} = C \times S_n F_0 p E (Q_\beta - E) \sqrt{(Q_\beta - E)^2 - m_{\nu_e}^2}, \tag{2.8}$$

---

[1]To be precise, EC process requires $Q > B_i$, where B_i is the electron binding energy, which can in principle be as low as a few eV for the outer atomic shells.

[2]However, despite of the difficulties with the strong background from competitive EC process, the two β^+-decaying nuclides with possibly very low decay energy are mentioned in Sec. 2.2.3.

where $S_n = S_n(E,Q_\beta,Z)$ – shape factor for n^{th}-forbidden transition; $F_0 = F_0(E,Z)$ – Fermi function; p, E – momentum and kinetic energy of the emitted electron; Q_β – the total β^- decay energy, and constant C is given by

$$C = G_F^2 \frac{m_e^5}{2\pi^3} \cos^2 \theta_C |M_{fi}|^2. \tag{2.9}$$

Here G_F^2 is the Fermi weak coupling constant, θ_C is the Cabibbo angle, m_e is the mass of the electron and $|M_{fi}|^2$ is the nuclear matrix element. For an allowed or superallowed transition the shape factor $S_n = 1$, and since both M_{fi} and $F(Z,E)$ are independent of m_{ν_e}, the dependence of the spectral shape on m_{ν_e} is given only by the phase space factor. A detailed derivation of the electron energy spectra of β^--decay can be found for example in [26, 27].

As can be seen from Eq. (2.8) the shape of the β-spectrum is sensitive to the anti-neutrino rest mass squared $m_{\nu_e}^2 = \sum_i |U_{ei}|^2 m_i^2$, since Eq. (2.8) is based on the relativistic energy-momentum relationship given in Eq. (2.4). The impact of the anti-neutrino mass is a reduction of the endpoint energy and a distortion of the spectrum close to the endpoint. Neglecting the small recoil of the heavy daughter nucleus, the outgoing electron can never obtain the entire decay energy Q_β, since the anti-neutrino takes away at least the amount of energy that corresponds to its mass. Consequently, the maximum electron energy is reduced and the spectrum is distorted in the close vicinity of the spectrum's endpoint, as shown in Fig. 2.1.
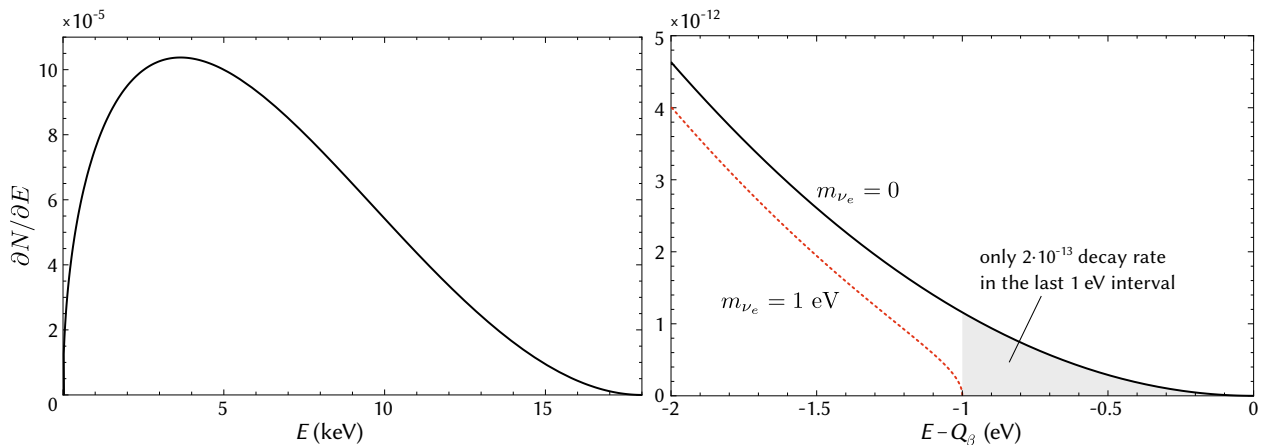

Figure 2.1: The electron energy spectrum of tritium β^--decay for $Q = 18.6$ keV. The right side shows a zoom into the endpoint region of the spectrum with the effect of a 1 eV neutrino mass indicated by the red dashed line.

Equation (2.8) represents only a simplified approach for the description of the electron energy spectrum in β^--decay. There are several higher order effects, which in case of the detection of only electron's spectrum can not be omitted, since their impact is compatible to the impact of the neutrino rest mass itself. For example, the recoil energy E_{rec} of the daughter nucleus or the sum over all possible final states (if β-emitter is a part of a molecule) have to be taken into account, otherwise it can cause not only a decrease in sensitivity to $m_{\nu_e}^2$, but can lead to erroneous conclusions.

2.1.2 Electron capture

The electron capture (EC) process is characterized by

$$(A,Z) + e^- \rightarrow (A,Z-1)^* + \nu_e \rightarrow (A,Z-1) + \nu_e + Q_{\mathrm{EC}}. \tag{2.10}$$

In the EC process a parent atom decays to an excited state of the daughter atom by capturing an electron from the inner shells and emitting an electron neutrino[1]. The de-excitation of the daughter atom to the ground state is a complex process, which includes cascades of both X-rays and electron emissions (Auger electrons and Coster-Kronig transitions). If we detect only charged decay products (electrons), the spectrum characterization is too difficult to reach even eV-sensitivity to the neutrino rest mass. However, the possibility to measure all the energy released in the decay process except for the energy taken away by the neutrino simplifies the description of the spectrum, and consequently increases the sensitivity to $m_{\nu_e}^2$, as it was pointed out for the first time in 1982 [28]. The expected shape of the calorimetrically measured EC spectrum, considering only first order excitations with only a single hole in the internal shell, is:

$$\frac{\partial \lambda}{\partial E_c} = A_{\mathrm{EC}} (Q_{\mathrm{EC}} - E_c)^2 \sqrt{1 - \frac{m_{\nu_e}^2}{(Q_{\mathrm{EC}} - E_c)^2}} \sum_i S_i \psi_i^2 \frac{\Gamma_H/2\pi}{(E_c - E_i)^2 + \Gamma_i^2/4}. \tag{2.11}$$

It shows Breit-Wigner resonances centered at an energy E_i, where E_i is the excitation energy of the final atom due to the electron hole in the i-shell resulting from the capture, which is within a few eV equal to the binding energy B_i of the i-shell electron in the daughter atom [29]. The resonances have an intrinsic width Γ_i related to the half-life of the excited states. The intensities of these lines are given mainly by the squared wave-function of the captured electron calculated at the nucleus ψ_H^2, containing also the squared overlap between the initial and the final atom orbital wave functions and the effect of electron exchange. These factors are then multiplied by the nuclear shape factors S_i. The Breit-Wigner resonances are modulated by the phase space factor, which depends on the square of the electron neutrino mass $m_{\nu_e}^2$ and the energy available to the decay Q_{EC}. A_{EC} in Eq. (2.11) contains, among other factors, the weak interaction coupling constant and the nuclear matrix element. It is worth noting that in this theoretical model, we have neglected higher order effects, such as two-hole peaks, de-excitations through virtual intermediate states, and interferences between de-excitation channels. The fractional occupancy of each considered atomic shell is set to 100%. The theoretical calorimeter spectrum of (2.11) is, thus, a single-hole approximation that assumes full collection of de-excitation energy by the calorimeter without pile-ups. The exemplary ^{163}Ho EC spectrum is shown in Fig. 2.2.

Similar to the β^--decay case, the shape of the EC spectrum is sensitive to the neutrino mass squared $m_{\nu_e}^2$. However, the spectrum is not smooth, but modulated by the Breit-Wigner resonances centered at the energies E_i. Thus, if the Q_{EC}-value happens to be close to one of these resonances at E_i, the rate near the endpoint will be greatly enhanced and the sensitivity to the neutrino mass is drastically increased. This fact will be used as a main criterion for the new candidates search for m_{ν_e} determination in the EC sector (see Sec. 2.2.2).

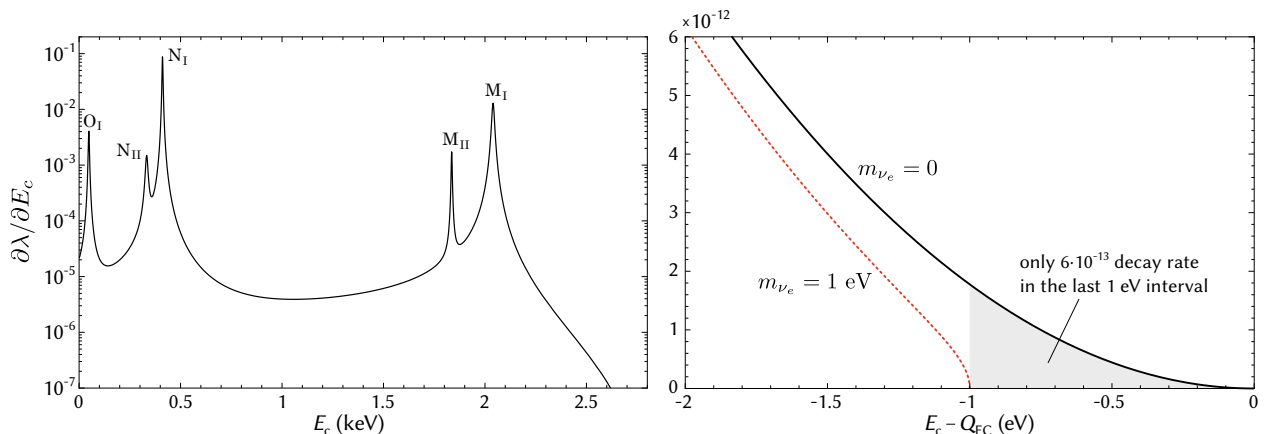[1]Unlike β^--decay, where an electron *anti-neutrino* is emitted, EC decay involves just a *neutrino*.

Figure 2.2: Left: de-excitation spectrum of ^{163}Ho for $Q_{EC} = 2.8$ keV. Right: a zoom into the endpoint region of the spectrum with the impact of 1 eV neutrino mass indicated by the red dashed line.

2.2 Suitable candidates for the neutrino mass search

The phase space region of low-energy neutrinos, where the highest sensitivity to the neutrino mass is achieved according to Eq. (2.6), corresponds to the very upper end of the β-spectrum. This extremely tiny part of the spectrum can be emphasized with respect to the neutrino mass by choosing β-transition with very low energy. Hence, the important selection criteria for the nuclide to be a good candidate for the neutrino mass determination using kinematic approach is the minimization of the total β-transition energy. The search for the low-energy β-transition can be done in the ground-to-ground, as well as in the ground-to-excited nuclear state decay domain.

2.2.1 Ground-to-ground state β^--decay transitions

The ground-to-ground nuclear state β^--decay sector has already been investigated for a century. For many nuclides which are not too far away from the valley of stability the β^--decay spectrum is measured and the Q_β-value is extracted. For some specific cases this energy is deduced by means of mass spectroscopy as the mass difference between parent and daughter atoms. Nowadays it is a well established fact that the lowest Q_β-value in the ground-to-ground state β^--decay domain is the nuclide ^{187}Re with $Q_\beta = 2.5$ keV, and the second lowest is ^{3}H (tritium) with $Q_\beta = 18.6$ keV. These two nuclides are near to the valley of β-stability, and the further away the nuclide is, the higher its β-decay energy. Therefore, it is not expected that there is any other nuclide, which has not yet been observed, but having even lower Q_β-value. Hence, nuclides ^{3}H and ^{187}Re are undoubtedly among the best candidates for the neutrino mass determination.

The majority of the published direct laboratory results on m_{ν_e} originate from the investigation of tritium β^--decay. The first "precise" tritium spectrum was reported in 1952 [30], giving $m_{\nu_e} < 250$ eV. To date, the study of ^{3}H spectrum using electrostatic spectrometers

yielded an upper limit on the electron anti-neutrino mass of 2 eV (95% C.L.) [27]. In the near future the promising tritium based experiment KATRIN (KArlsruhe TRItium Neutrino) [31, 32] aims to reduce the upper limit of the effective electron neutrino mass down to 0.2 eV (90% C.L.) with an absolute instrumental energy resolution on the order of 40 meV [33].

Despite ^{187}Re has 7.5 times lower Q_β-value as compared with tritium, its precise β-spectrum investigation is inhibited due to the complicated electronic structure. A break-through was made only two decades ago, when cryogenic microcalorimetric techniques were developed. The advantage of this approach is that all the released energy except that of the neutrino is measured by automatic integration of all the de-excitation processes within the detector, which acts as an absorber. Two pioneering groups have independently started the field of ^{187}Re β^--decay experiments at Milan (MiBeta) and Genoa (MANU). The MANU group used a single metallic rhenium crystal as absorber and managed to set an upper limit on the anti-neutrino mass of $m_{\nu_e} < 26$ eV (95% C.L.) [34], while MiBeta used an AgReO$_4$ absorber and set $m_{\nu_e} < 15$ eV (90% C.L.) [35]. Among the main limitations for further investigation of ^{187}Re spectrum are the low specific activity of about 1 Bq/mg and the relative slowness of the thermalization process in the detector. More details concerning the limitations one can find in Sec. 7.1.1.

In order to examine possible effects of the systematics, which can affect the spectrum and hinder neutrino mass determination, the direct Q_β-value as the mass-difference between parent and daughter atoms should be known with an uncertainty similar to the energy resolution of the detector. For example, in case of the KATRIN experiment it is of about 50 meV, which corresponds to $\Delta M/M \approx 10^{-11}$. Several attempts have been made to measure the Q-value of tritium by Penning-trap mass spectrometry (PT-MS)[1]. Although, a very high precision was achieved, there is a large discrepancy between different measurements, which sometimes is referred to as the "^{3}He puzzle" [36]. The Q_β-value of ^{187}Re was also measured by several groups, although never by PT-MS but only as the endpoint energy in the Kurie plot of the β-spectrum. In total there were 7 results published, which are also inconsistent. To make a cross check we performed for the first time a direct and independent Q_β-value determination of ^{187}Re using PT-MS [37]. The measurement procedure is described in Sec. 5.3.1, while a detailed discussion is done in Sec. 7.1.1.

2.2.2 Ground-to-ground state electron capture domain

Unlike β^--decay transitions, where the lower the Q-value, the higher the sensitivity to m_{ν_e}, the best candidate in EC domain would be a nuclide with not necessarily the lowest Q_{EC}-value, but rather lowest $(Q_{EC} - B_i)$-value (see Sec. 2.1.2 and Eq. (2.11)). The lowest Q_{EC}-value has the nuclide ^{163}Ho with $Q_{EC} = 2.833(34)$ keV, and correspondingly the lowest so far $(Q_{EC} - B_{MI}) = 0.79(3)$ keV [38], decaying with the half-life of 4570(50) years [39]. This Q_{EC}-value of ^{163}Ho was for the first time directly measured with the Penning-trap

---

[1]Penning-trap mass spectrometry is based on the measurements of the free cyclotron frequency, which is inversly proportional to the ion's mass. The PT-MS method is described in the dedicated Chapter 4.

mass spectrometer SHIPTRAP solving the long-standing problem of large discrepancies in the Q_{EC}-values determined by different techniques [38, 40].

Besides ^{163}Ho, there are 10 other nuclides with Q_{EC}-values of less than 100 keV, being in the range of their electron binding energies ranging up to $B_K = 88$ keV for the K-electron in lead. However, as one can see from Fig. 2.3 there are only 3 nuclides, namely ^{150}Pm, ^{194}Hg and ^{202}Pb, whose Q_{EC}-values are too imprecise to conclude whether their $(Q_{EC} - B_i)$-values can compete with ^{163}Ho. The nuclide ^{150}Pm decays mostly via β^--decay with $T_{1/2} = 2.7$ h having a very small EC decay branching. Its EC decay has never been observed so far and the Q_{EC}-value of 83(20) keV is known from the mass evaluation in [1], therefore ^{150}Pm is not feasible for the neutrino mass determination and can be omitted. Thus, only ^{194}Hg and ^{202}Pb are considered.
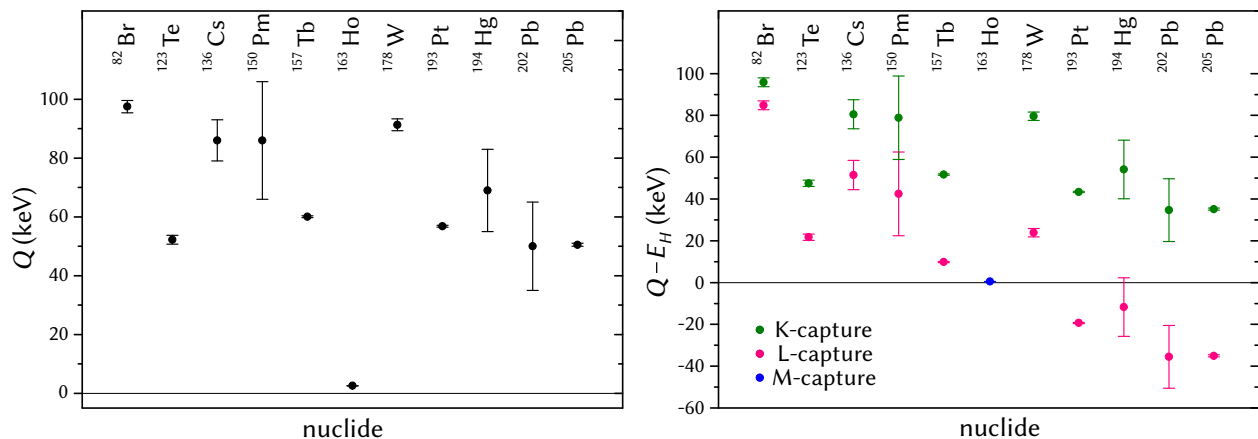

Figure 2.3: Nuclides with electron capture Q_{EC}-values below 100 keV. Data are taken from [41]. In the left graph Q_{EC}-values are plotted, in the right graph $- (Q_{EC} - B_i)$-values.

To make the final conclusion concerning the ^{194}Hg and ^{202}Pb applicability to the neutrino mass determination, their Q_{EC}-values have to be precisely and accurately measured using PT-MS. The proposal to the ISOLDE Committee at CERN was submitted in 2007 and accepted in 2008 [42]. This proposal aims for the precise Q-value measurements of ^{194}Hg and ^{202}Pb by the Penning-trap facility ISOLTRAP. In total 8 shifts of on-line beam at ISOLDE for absolute mass measurements of ^{194}Hg, ^{194}Au, ^{202}Pb and ^{202}Tl were accepted. Basic information about the nuclides ^{194}Hg, ^{202}Pb, and their daughters is presented in Table 2.1. The so far known neutrino total emitted energy for ^{194}Hg is $Q_\nu^K \equiv Q_{EC} - B_K = -12(14)$ keV and for ^{202}Pb is $Q_\nu^L = 35(15)$ keV, therefore an improvement of the precision by a factor of 3 would be sufficient to conclude whether these nuclides are good candidates or not. Hence, ultra-precise mass measurements in a future Penning-trap experiment should follow.

In 2010 the Q_{EC}-value measurement of ^{194}Hg was performed at the ISOLTRAP facility [43]. The masses of ^{194}Hg and ^{194}Au were measured in separate runs within a month in between. The resulting new Q_{EC}-value of ^{194}Hg was 29(4) keV. Taking this value it is clear that K-capture is energetically forbidden and the total energy of the neutrino in case of allowed L-capture is $Q_\nu = 15(4)$ keV. The measured Q_{EC}-value showed more than two standard deviations discrepancy compared to the value evaluated in AME2003 [41]. This discrepancy,

Table 2.1: Candidates and their daughter nuclides for neutrino-oriented precision mass spectrometry, as proposed in [42]. Relative precision on the absolute masses $\delta M/M$ and Q_{EC}-values are taken from [41]. To be a good candidate the neutrino total energy $Q_\nu^i = Q_{\mathrm{EC}} - B_i$ should be as small as possible. The uncertainties of the last digits are given in brackets.

Nuclide	$T_{1/2}$	$\delta M/M$	Q_{EC} (keV)	i-shell	B_i (keV)	Q_ν^i (keV)
^{194}Hg	440(80) y	$6.7\,\mathrm{E}-8$	69(14)	K	80.72	$-12(14)$
				L	14.35	55(14)
^{194}Au	38.02(10) h	$5.7\,\mathrm{E}-8$				
^{202}Pb	52.5(28) ky	$4.5\,\mathrm{E}-8$	50(15)	K	85.53	$-36(15)$
				L	15.35	35(15)
^{202}Tl	12.23(2) d	$5.4\,\mathrm{E}-8$				

however, was not too surprising, because it has already been shown that masses derived from β-decay spectroscopy might well be inaccurate in a broad range of mass numbers and can exhibit discrepancies as compared with PT-MS by more than 50 keV [44].

The last intriguing case proposed in [42] is ^{202}Pb, which is partly the subject of this thesis. The aim of this work is to measure the absolute mass of the daughter nuclide ^{202}Tl and finally derive the Q_{EC}-value of the EC in ^{202}Pb, since the absolute mass value of ^{202}Pb was already measured in the previous experimental run [45]. The ^{202}Tl mass measurement procedure is described in Sec. 5.3.3, while the discussion and conclusion can be found in Sec. 7.1.2.

2.2.3 Ground-to-excited state β-decay transitions

Besides the ground-to-ground state decay domain, one can consider ground-to-excited state weak decays. A thorough analysis of the existing nuclear physics data demonstrates that there are many β-transitions for which mass differences of the transition partners Q_{gg} are close to the values for the excited states of the daughter nuclides (including the electron-binding energies in case of EC). The expected β-decay energy transitions – Q_{ge}-values – to these excited states should be very small. However, the Q_{ge}-values are masked by a very large uncertainty in the Q_{gg}-values. In contrast, the energy of the nuclear excited states E^* is usually known with sufficient precision. Thus, the ground-to-ground state mass differences Q_{gg} of the selected β-transitions should be precisely measured in order to obtain definite information on the decay energy to the excited states. Presently, only PT-MS meets the required precision of < 1 keV as compared with all the other existing methods.

In 2009 it was announced that the β^--decay of ^{115}In to the nuclear excited state of 497 keV in ^{115}Sn with the branching ratio of $10^{-4}\%$ has the smallest decay energy $Q_{\mathrm{ge}} = 155(10)$ eV [46]. However, this case has not found yet its application for the kinematic neutrino mass determination due to its ultralong partial decay half-life of $4.1(6)\cdot 10^{20}$ y [46]. Therefore, it would be very challenging to find the neutrino mass fingerprint on top of the strongly dominant, but still very slow ($T_{1/2} = 4.41(25)\cdot 10^{14}$ y) ground-to-ground β-transition of ^{115}In. Moreover, the tiny decay energy would definitely require a cryocalorimetric detection method and a macroscopic ^{115}In sample in order to have decent count-rate, what in turn
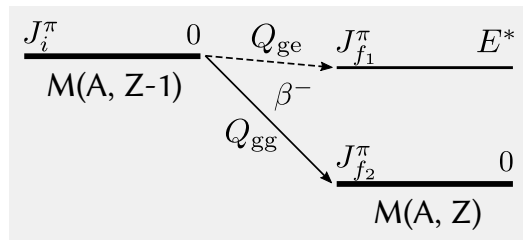
Figure 2.4: β-transition to the ground state with the decay energy Q_{gg} and to the excited state with presumably very low decay energy Q_{ge}.

causes many other technical challenges, which are insurmountable for the current cryogenic microcalorimeters (CM).

Meanwhile, a question arises whether there are other relevant β-transitions for the neutrino mass determination suitable for both PT-MS and CM. A thorough analysis was done only for those cases where ground-to-ground state decay energies (Q_{gg}-values) are smaller than 1 MeV. Table 2.2 summarizes appropriate β-transitions. From column 6 of Table 2.2 it can be seen that the absolute values of the β-transition energies are typically smaller than their uncertainties.

The most promising β-transitions to nuclear excited states are the allowed transitions in ^{131}I, ^{131}Cs, ^{134}Ce, ^{159}Dy, ^{175}Hf and ^{189}Ir. Actually, the branching ratios for β-transitions in ^{134}Ce and ^{159}Dy are known and equal to $2 \cdot 10^{-3}$ [47] and $2 \cdot 10^{-4}$ [48], respectively. All the other cases in Table 2.2 are forbidden transitions, and therefore their branching ratios are expected to be even smaller. Nevertheless, the partial half-life of all the nuclides in Table 2.2 is expected to be in the reasonable range, so that the calorimetric method to measure corresponding β-decay spectra can, in principle, be applicable. A proposal to the ISOLDE for measurements of the allowed EC transitions, namely ^{131}Cs, ^{134}Ce, ^{159}Dy and ^{175}Hf, was submitted and successfully accepted in 2014 [49]. In the proposal the four allowed EC transitions, whose decay energies to excited states can be in a sub-keV level, are suggested to be of the primary cases to be measured, whereas the other cases can be considered at the latter stage. The first measured Q_{gg}-value within the framework of the proposal was for the nuclide ^{131}Cs, and became a part of this thesis. The measurement procedure can be found in Sec. 6.1.2, while discussion of the achieved result is in Sec. 7.1.3.

Table 2.2: The most promising β-transitions to nuclear excited states with possibly ultra-low decay energies. The first part of the table represents nuclides which can be produced at ISOLDE and measured at ISOLTRAP as declared in our proposal in [49]. Nuclides in the second part of the table doesn't seem possible for the production at ISOLDE and are shown for the completeness. The ground-to-ground state decay energy values Q_{gg} with their uncertainties δQ_{gg} are taken from [1]. The data for the excited states E^* of daughter nuclides is from [50]. The half-lives $T_{1/2}^{\text{gg}}$ are for ground-to-ground state decays [51]. The maximum emitted neutrino energy Q_{ge}^{ν} is equal to $(Q_{\text{gg}} - E^*)$ for β^--transition, and $(Q_{\text{gg}} - E^* - B_i)$ for EC decay, where B_i is the binding energy of electron in i-shell of the daughter atom. Nuclide with the smallest, but positive Q_{ge}^{ν}-value will have the highest sensitivity to m_{ν_e}. Only nuclides with $(Q_{\text{ge}}^{\nu} \pm 2\delta Q_{\text{ge}}^{\nu}) \approx 0$ are given. Additional criteria for the nuclide of choice is that β-transition spin change is not more than 2, i.e. $\Delta J_{\text{ge}} \leq 2$. For more details see text.

β-transition	$\Delta J_{\text{ge}}^{\pi}$	$T_{1/2}^{\text{gg}}$	$Q_{\text{gg}} \pm \delta Q_{\text{gg}}$ (keV)	$E^* \pm \delta E^*$ (keV)	$Q_{\text{ge}}^{\nu} \pm \delta Q_{\text{ge}}^{\nu}$ (keV)	transition type
^{111}In $\rightarrow$ ^{111}Cd*	2^+	2.8 d	860 ± 3	855.6 ± 1	0.4 ± 3	L
					3.6 ± 3	M
^{130}Cs $\rightarrow$ ^{130}Ba*	1^+	29 min	362 ± 9	357.38 ± 0.08	4.6 ± 9	β^-
^{131}Cs $\rightarrow$ ^{131}Xe*	0^+	9.7 d	355 ± 5	364.490 ± 0.004	-15 ± 5	L
					-11 ± 5	M
^{134}Ce $\rightarrow$ ^{134}La*	1^+	3.2 d	386 ± 29	355.479 ± 0.012	-8 ± 29	K
					24 ± 29	L
^{140}Nd $\rightarrow$ ^{140}Pr*	$(2,3)^+$	3.4 d	429 ± 7	419.9 ± 0.3	2 ± 7	L
					8 ± 7	M
^{146}Pm $\rightarrow$ ^{146}Nd*	1^-	5.6 y	1472 ± 4	1470.6 ± 0.1	-5.7 ± 4	L
					-0.2 ± 4	M
^{149}Gd $\rightarrow$ ^{149}Eu*	1^-	9.3 d	1314 ± 4	1312 ± 4	-6 ± 6	L
					0.2 ± 6	M
^{155}Eu $\rightarrow$ ^{155}Gd*	2^-	4.7 y	251.8 ± 0.9	251.706 ± 0.001	0.1 ± 0.9	β^-
^{159}Dy $\rightarrow$ ^{159}Tb*	1^+	144 d	365.2 ± 1.2	363.545 ± 0.002	-0.3 ± 1.2	M
^{161}Ho $\rightarrow$ ^{161}Dy*	1^+	2.5 h	858.5 ± 2.2	804.388 ± 0.003	0.3 ± 2.2	K
	1^+			858.792 ± 0.002	-2.3 ± 2.2	M
^{171}Tm $\rightarrow$ ^{171}Yb*	2^+	1.2 y	96.5 ± 1.0	95.282 ± 0.002	1.3 ± 1	β^-
^{175}Hf $\rightarrow$ ^{175}Lu*	2^-	70 d	683.9 ± 2.0	626.53 ± 0.15	-6 ± 2	K
	1^+			672.83 ± 0.15	0 ± 2	L
^{201}Tl $\rightarrow$ ^{201}Hg*	$(2)^-$	72.9 h	482 ± 14	384.602 ± 0.018	14 ± 14	K
	2^-			464.41 ± 0.03	3 ± 14	L
^{77}As $\rightarrow$ ^{77}Se*	1^-	38.8 h	683.2 ± 1.7	680.103 ± 0.002	3.1 ± 1.7	β^-
^{131}I $\rightarrow$ ^{131}Xe*	1^+	8.02 d	970.8 ± 0.6	971.22 ± 0.13	-0.4 ± 0.7	β^-
^{188}W $\rightarrow$ ^{188}Re*	(1^+)	69.8 d	349 ± 3	353.57 ± 0.02	-4.6 ± 3	β^-
^{189}Ir $\rightarrow$ ^{189}Os*	1^+	13.2 d	537 ± 13	531.55 ± 0.03	-7.5 ± 13	L
					2.4 ± 13	M

2.3 keV-scale sterile neutrino

The number of neutrino flavours in the Standard Model is known from LEP-experiment (Large Electron Positron Collider) at CERN, where the decay width of the Z-boson was analysed. The conclusion was that there exist $N_\nu = 2.994 \pm 0.012$ neutrinos provided that they are only weakly interacting particles [52]. In the Standard Model, all of the leptons are said to be Dirac particles and, except for the neutrinos, they all have two polarization states. By convention it is said that they exist as left-handed and right-handed particles. However, neutrinos are different, because when measured in experiments where only weak interaction is considered, they are always left-handed, while anti-neutrinos are always right-handed. This effect is called parity violation. Therefore, if neutrinos are pure Dirac particles, there should also exist right-handed neutrinos and, correspondingly, left-handed anti-neutrinos[1]. In literature, they are called sterile neutrinos, as they do not participate in any Standard Model electro-weak interactions.

As it was already discussed in Sec. 1.1, the Standard Model doesn't predict any masses for the active neutrinos, but the masses are required by the experimentally verified neutrino oscillations. A simple way to incorporate the neutrino masses is to extend the model with the right-handed neutrinos - sterile neutrinos - as just discussed above. In principle it is possible to add an arbitrary number of sterile neutrinos, but at least three of them are needed to explain the neutrino oscillations, the baryon asymmetry, and the Dark Matter (DM) [53]. Interestingly, this is the same number as the number of leptonic families. The successful "three sterile neutrino extension" of the Standard Model is called the νMSM (neutrino Minimal Standard Model). In the νMSM the lightest of the sterile neutrinos plays the role of the DM particle. Nevertheless, it is worth noting that although νMSM is the minimal extension of the SM with no new physics other than three sterile neutrinos up to the Planck scale, there is a bulk of many other different models in the literature [54].

The sterile neutrino was originally proposed as a DM candidate by Dodelson and Widrow in 1994 [55] to solve the discrepancies between the Cold Dark Matter predicted structure formation and the observations. It is the sterile neutrino with a mass in the keV-range whose interaction is dominated by gravity. Nowadays the keV-scale sterile neutrino is also known as a Warm Dark Matter (WDM) candidate. There are two reasons to motivate a keV mass scale for a sterile neutrino DM candidate. First, fermionic DM can not have an arbitrarily small mass, since in dense regions (e.g. in galaxy cores) it cannot be packed within an infinitely small volume, due to the Pauli principle. This results in a lower bound on the mass, the so-called Tremaine-Gunn bound [56]. Second, sterile neutrinos presumably have mixing, although very small, with the active neutrinos, which would enable a DM particle to decay into an active neutrino and a mono-energetic photon. Since the decay rate scales with the fifth power of

---

[1]The neutrinos can also be of another type called Majorana particles, which by definition are their own anti-particles. If the neutrinos are pure Majorana particles they can be described as entirely left-handed, but then the lepton number conservation in electro-weak interactions involving neutrinos is violated. It is very difficult to distinguish experimentally between the two types of particles. But reality can be even more complicated if neutrinos are a mixture between Dirac and Majorana particles achieving characteristics from both types.

the initial state mass, a non-observation of the corresponding X-ray peak leads to an upper bound of a few tens of keV. It is these two general constraints, the phase space and X-ray bounds, which enforce keV-scale masses for sterile neutrinos acting as WDM (see Fig. 2.5).
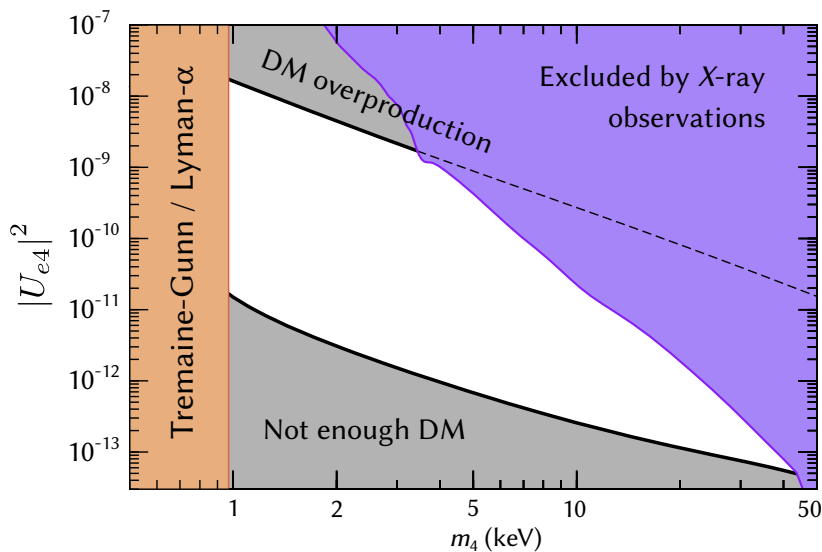

Figure 2.5: The allowed region of parameters of sterile neutrino WDM particles in the νMSM (white unshaded region) confronted with existing experimental bounds. For any combination of mass and mixing angle between two black curves the necessary amount of dark matter can be produced. The blue shaded region in the upper right corner is excluded by the non-observation of decaying DM transition lines in the X-ray regime. In the region below 1 keV the sterile neutrino is too light and is ruled out based on «Tremaine–Gunn» like arguments and on the Lyman-α analysis. Figure is reproduced from [57].

Despite the many existing beautiful theoretical models and stringent cosmological/astrophysical constrains, the direct Dark Matter experiments are an essential probe to complement indirect searches in a largely model-independent way. In general, two distinct paths for the direct DM search can be considered. The first option is to detect the DM particle present in our galaxy by using large-scale detectors. The ability of existing direct DM search experiments (e.g. Xenon [58] or LUX [59]) detect sterile neutrinos via elastic scattering with atoms [1]. On the other hand, as a second option, one may produce the DM particle in a laboratory setup and detect its presence via kinematic considerations. In kinematic approach the nuclides with low β-decay energies, namely in the range between 1 and 100 keV, are of the primary interest.

In 1980, a long time before the undoubted evidence for neutrino oscillations, Shrock examined a possibility of searching for any neutrino mass states m_4 also in β^--spectra [60]. An admixture of each of such states should produce a specific discontinuity (a kink) in the β^--spectrum at energy $Q_\beta - m_4$. The relative intensity of the kink observed at $Q_\beta - m_4$ would determine the value $|U_{e4}|^2$. This idea stimulated many scientists to search for an admixture of heavy neutrinos in their β^--spectra.

---

[1]Actually, the sterile neutrinos have no coupling to ordinary matter. Thus, the sterile neutrinos have to, first, mix with the "active" neutrinos, and the latter may already be detected in a direct detection detector over the scattering on electrons.

Simpson investigated the β^--spectrum of tritium implanted into a Si(Li) detector and observed a distortion in the spectrum part below 1.5 keV. He interpreted this distortion as the evidence of a heavy neutrino emission with the mass of about 17.1 keV and mixing probability of 3% [61]. Later, the study of the β^--spectrum of ^{63}Ni with magnetic spectrometers put the admixture of the 17 keV neutrino below $5 \cdot 10^{-4}$ at 95% CL and found $|U_{e4}|^2 < 1 \cdot 10^{-3}$ for all m_4 between 4 and 30 keV [62]. "The rise and fall of the 17 keV neutrino" is briefly described in [63]. At present, there are no β-spectroscopic indications for sterile neutrinos, and the relevant data are summarized in [24]. The best upper limits of $|U_{e4}|^2$ are shown in Fig. 2.6.
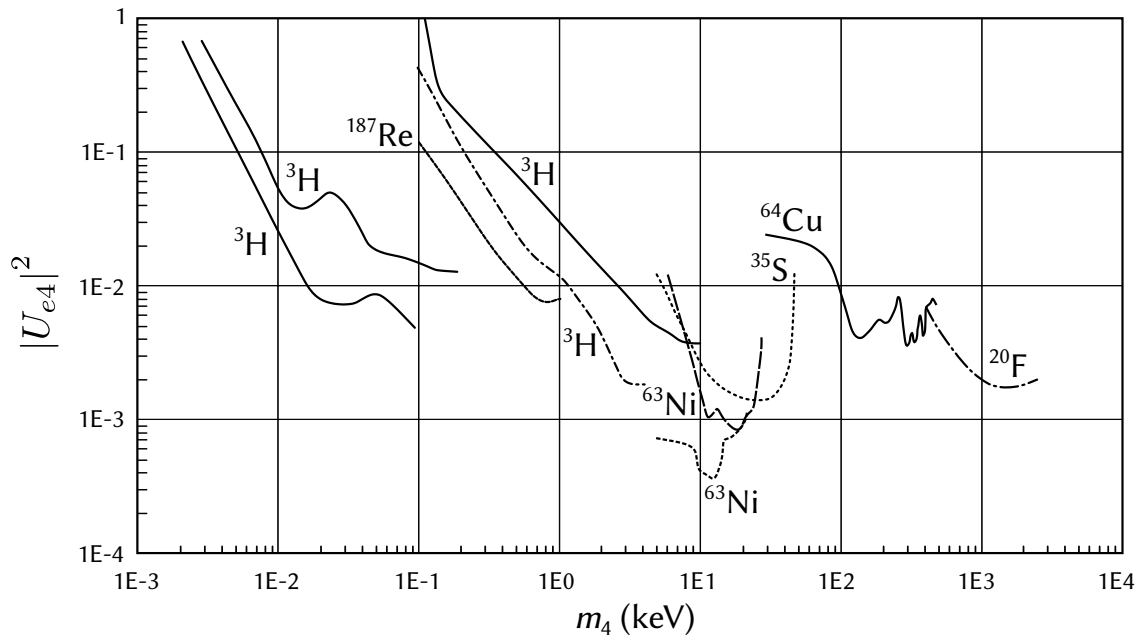

Figure 2.6: The best upper limits on the admixture $|U_{e4}|^2$ of sterile neutrinos derived from measured β^--decay spectra. The figure is reproduced from [64].

2.3.1 On the keV sterile neutrino search in electron capture

Besides investigation of continuous β^--spectra, a joint effort of cryogenic microcalorimetry (CM) and high-precision Penning-trap mass spectrometry (PT-MS) in investigating EC process can also shed light on the possible existence of heavy sterile neutrinos with masses from 0.5 to 100 keV [65]. This idea was suggested for the first time by us in [65]. Later, a more generalized theoretical approach was applied in [66].

In the similar way as in β^--decay, sterile neutrinos are expected to perturb the shape of the atomic de-excitation spectrum measured calorimetrically after EC decay. Although the perturbation effect is more conspicuous in β^--spectrum (because it is a smooth curve, while the de-excitation spectrum after EC shows many peaks), however in β^--decay (if conventionally measured) the possible excitations of the atoms or molecules are not disentangled while in EC the calorimeter collects all the energy independently of the excitation of the atom and of the de-excitation path, and one has higher statistics around the capture peaks.

Since the differential decay rates contain many peaks it is more convenient to consider integrated decay rates over specific energy ranges. This amounts to consider that the detector collects events within energy ranges $E_i \pm \Delta$ and $E_j \pm \Delta$ in two regions of the spectrum. A ratio R between the number of collected events in both regions is then performed, which corresponds to the theoretical expression:

$$R = \frac{\Lambda_i}{\Lambda_j} = \frac{\kappa_i^{\mathrm{act}} + \tan^2\theta \, \kappa_i^{\mathrm{st}}}{\kappa_j^{\mathrm{act}} + \tan^2\theta \, \kappa_j^{\mathrm{st}}}, \tag{2.12}$$

where $\Lambda_l = \cos^2\theta \, \kappa_l^{\mathrm{act}} + \sin^2\theta \, \kappa_l^{\mathrm{st}}$ (in the region where sterile mass eigenstates contribute) and $\Lambda_l = \cos^2\theta \, \kappa_l^{\mathrm{act}}$ (in the region where sterile mass eigenstates are energetically forbidden); index $l = \{i,j\}$ indicates different atomic electron orbits. The integrals κ are defined as

$$\kappa_l^{\mathrm{act}} = \int_{E_l-\Delta}^{E_l+\Delta} \frac{\partial\lambda}{\partial E_c}\bigg|_{m_\nu=0} \partial E_c\,, \quad \kappa_l^{\mathrm{st}} = \int_{E_l-\Delta}^{E_l+\Delta} \frac{\partial\lambda}{\partial E_c}\bigg|_{m_\nu=m_4} \partial E_c\,, \quad l = \{i,j\}\,, \tag{2.13}$$

where κ_l^{act} assumes the existence of only standard "active" neutrinos, which mass is, however, neglected, while κ_l^{st} includes only sterile neutrinos as m_4. It is straightforward to select i and j as the energies of two peaks in EC spectrum, and the integration intervals can be chosen as the width of these capture peaks.

Let us for simplicity approximate the peaks by delta functions using $\Delta \to 0$, and assume that $E_i \approx B_l$, where B_l is the binding energy of the electron in the l-shell. Then the integrals κ_l can be written as

$$\kappa_{l,k}^{\mathrm{act}} = A_{\mathrm{EC}}\, S_{l,k}\, \psi_{l,k}\, (Q_k - B_l)^2\,, \tag{2.14}$$

$$\kappa_{l,k}^{\mathrm{st}} = A_{\mathrm{EC}}\, S_{l,k}\, \psi_{l,k}\, (Q_k - B_l)^2 \sqrt{1 - \frac{m_4^2}{(Q_k - B_l)^2}}\, \mathrm{H}[(Q_k - B_l) - m_4]\,, \tag{2.15}$$

where A_{EC} contains, among other factors, the weak interaction coupling constant and the nuclear matrix element; index k denotes a certain nuclide; $\psi_{l,k}$ is the squared wave-function of the captured l-electron calculated within the nucleus, containing also the squared overlap between the initial and final atom orbital wave functions and the effect of electron exchange; $S_{l,k}$ is the nuclear shape factor, which contains the neutrino momentum dependence for the peak l coming from the leptonic matrix element squared for a nuclide k; Q_k is the total decay energy (Q-value) in a given isotope k; B_l is the energy position of a given peak l in the calorimeter spectrum; $\mathrm{H}[(Q_k - B_l) - m_4]$ is the Heaviside step function, which equals 1 when $m_4 \leqslant (Q_k - B_l)$, and 0 when $m_4 > (Q_k - B_l)$.

The considered ratio R between the intensity of two peaks in the electron capture spectrum of a given nucleus allows us to remove uncertainties related to the nuclear matrix element and to the values of overall constants. The physics parameters needed to determine the keV-sterile neutrino contribution $|U_{e4}|^2 = \sin^2\theta$ to the capture probability are the atomic mass difference Q_{EC} of the capture partners, the energy position B_l of a given peak l in the calorimeter spectrum and the electron density $\psi_{l,k}$ at the nucleus. Highly accurate Q_k-value is the matter of PT-MS; determination of peak positions B_l and experimental ratio of two

peaks R_{exp} are attributed to CM, whereas $\psi_{l,k}$ is an entirely theoretical quantity. Both the experimental measurement and the theoretical model must be accurate enough to detect differences in the expected versus the measured ratios.

In order to exclude the uncertainty of theoretical values $\psi_{l,k}$, the numerator and the denominator in Eq. (2.12) can be themselves ratios of numbers of events within the same peak but for different isotopes a and b of the same chemical element:

$$R' = \frac{\Lambda_{i,a}/\Lambda_{i,b}}{\Lambda_{j,a}/\Lambda_{i,b}} = \Re_{ijab} \left(\frac{1 + \eta_{ia}\tan^2\theta}{1 + \eta_{ja}\tan^2\theta} \right) \left(\frac{1 + \eta_{jb}\tan^2\theta}{1 + \eta_{ib}\tan^2\theta} \right), \tag{2.16}$$

where

$$\Re_{ijab} = \left[\frac{(Q_a - B_i)(Q_b - B_j)}{(Q_a - B_j)(Q_b - B_i)} \right]^{2(\gamma+1)} \tag{2.17}$$

and

$$\eta_{lk} = \text{H}[(Q_k - B_l) - m_4] \left[1 - \left(\frac{m_4}{Q_k - B_l} \right)^2 \right]^{\gamma+1/2}, \quad l = \{i,j\}, \quad k = \{a,b\}. \tag{2.18}$$

Here γ depends on the angular momenta of each lepton in a given ΔJ^π nuclear transition [66]. For instance, for allowed decays (such as EC in ^{163}Ho), $\gamma = 0$, whereas for first forbidden decays, $\gamma = 1$ for $s_{1/2}$ and $p_{1/2}$ peaks or $\gamma = 0$ for $p_{3/2}$ and $d_{3/2}$ peaks. For simplicity in Eq. (2.16) it is assumed that both peaks i and j are of the same type, namely $\gamma_i = \gamma_j = \gamma$.

From Eq. (2.16) one can see that the factors ψ_i and ψ_j cancel out in addition to the factor A_{EC}, which cancels out in both ratios (R and R'). However, the cancellation of atomic factors in R' is valid only to some extend. The inequality of the atomic factors for two different isotopes of the same chemical element comes from different mean square charge radii of the nuclei, and therefore affecting on electron density at the nucleus and on the exchange and overlap corrections between orbital electrons. In our paper [65] it was shown that the cancellation of atomic factors is valid on the level of 10^{-5}. The estimation of the sensitivity to the sterile neutrino contribution $|U_{e4}|^2$ in dependence on its mass m_4 for a bunch of relevant nuclides is discussed in Sec. 7.1.4.

3. Stellar enchancement of beta-decay rate

In Section 1.2 it was introduced that β-decay rates λ_β measured in terrestrial experiment may significantly differ from stellar ones. The enhancement results from different effects related to the thermal population of excited nuclear states in the hot photon bath or through atomic effects in the highly ionized, dense stellar plasma. The effect of enhanced β-decay has to be accurately considered when studying the slow neutron capture stellar nucleosynthesis process – the s-process.

To present knowledge, the s-process is expected to take place at the temperature $T \approx 3.5 \cdot 10^8$ K and the neutron density $n_{\mathrm{n}} \approx 10^8 \mathrm{cm}^{-3}$ on a time scale of about 10^3 years. It means that we have a hot and dense plasma environment for the nuclear reactions of interest. Having this hot plasma environment, lets consider the possible β-decay enhancement effects in more details.

3.1 Energy release in a β-transformation process

In a general case of hot stellar environment an atom with the proton number Z can be represented as the nucleus in a thermally populated exited state E^*, plus q-times ionized atomic shell, being also in an exited state ξ^*. The mass M^* of such an atom is

$$M^* = M_0 - q m_e + \sum_{k=1}^{q} B_k + \xi^* + E^*, \tag{3.1}$$

where M_0 is the ground state atomic mass, m_e is the electron mass, and $\sum_{i=1}^{q} B_i$ is the total binding energy of the q outermost electrons. Due to the energy conservation law and the mass-energy equivalent principle the energy released in a decay process is equal to the mass difference between initial and final states. Therefore, the energy release $Q^{(q)}$ for β-transition in case of β^--decay or EC can be written as

$$Q^{(q)} = Q_{\mathrm{neut}} + \left\{ \sum_{k=1}^{q} B_k + \xi^* + E^* \right\}_i - \left\{ \sum_{l=1}^{q} B_l + \xi^* + E^* \right\}_f, \tag{3.2}$$

where $Q_{\mathrm{neut}} = M_{0,i} - M_{0,f}$ is the mass difference between neutral atoms in the ground states. Subscript index i represents the atom in the initial state with proton number Z, index f - in the final state with $Z + 1$ protons for β^--decay or $Z - 1$ protons for EC. The screening of

the nuclear charge by continuum electrons is not considered for simplicity, however this effect may be non-negligible at low temperature and/or extremely high density of stellar interior.

For highly charged ionic states it may be more convenient to calculate the total electron binding energy as

$$\sum_{k=1}^{q} B_k = B_{\text{tot}} - \sum_{j=1}^{Z-q} B_j, \qquad (3.3)$$

where B_{tot} is the total electron binding energy of a neutral atom, and $\sum_{j=1}^{Z-q} B_j$ is the total binding energy of $(Z-q)$ left electrons in a q-times ionized atom with proton number Z. Values B_{tot} are tabulated in [67], whereas for H- and He-like ions binding energies can be found, for example, in [68] and [69], respectively.

In Fig. 3.1 one can see the impact of the $\{\sum_{k=1}^{q} B_k\}_i - \{\sum_{k=1}^{q} B_k\}_f$ term in Eq. (3.2). This effect leads to the shift in the β-transition energy for ionized atoms. The effect becomes significant for highly ionized atoms with low Q_{neut}-values. Consequently, the energy shift may open new or close previously possible, but now energetically forbidden β-transitions. This effect will be discussed in more detail in Sec. 3.2.
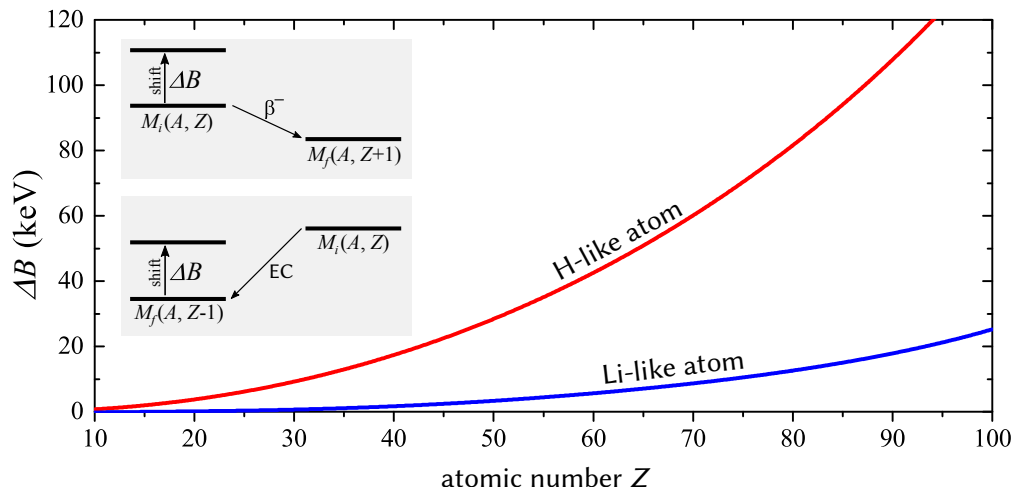

Figure 3.1: Value of the $\Delta B = \{\sum_{k=1}^{q} B_k\}_i - \{\sum_{k=1}^{q} B_k\}_f$ term in Eq. (3.2), which represents the energy shift of a β-transition for H- and Li-like ions in dependence on the proton number Z.

Usually, the atomic excitation energy difference $\xi_i^* - \xi_f^*$ in Eq. (3.2) can be neglected. In the contest of this thesis the relevant low-lying exited nuclear states E^* are usually well studied by means of nuclear spectroscopy, and the precision of their energy is on the order of a few tens of eV or better. The most well-known values are the electron binding energies, which can be theoretically calculated with a precision better than a few eV. Apparently, the least precise term in Eq. (3.2) is the Q_{neut}-value, which hinders precise calculation of $Q^{(q)}$-values and therefore makes prediction of β-transitions energetic spectrum in various stellar conditions less reliable. The importance of high precision and accurate determination of the Q_{neut}-values for low-energy β-decay nuclides is discussed in Sec. 7.2.

3.2 β-decay from thermally populated excited nuclear states

At high stellar temperatures the low-lying nuclear excited states are commonly involved into the decay process. If equilibrium between the excited state and the ground state has not been attained, then the excited nucleus must be treated as a component of the overall composition in the same way as the ground-state nucleus. In most cases of interest the excited states are in equilibrium with the ground state, even though general equilibrium of a star has not been attained. A test can be made by comparing the lifetime $\tau(I \to I^*)$ for photoexcitation from the ground to the excited state with the time scale t for the astrophysical circumstance under consideration. Equilibrium will be attained if $\tau(I \to I^*) \lesssim t$. The lifetime $\tau(I \to I^*)$ can be computed from the spontaneous decay lifetime of the excited state $\tau_{\mathrm{sp}}(I^* \to I)$, which is frequently known, by using the following equation [70]:

$$\frac{\tau(I \to I^*)}{\tau_{\mathrm{sp}}(I^* \to I)} = \frac{2J+1}{2J^*+1} \left[\exp\left(E^*/kT\right) - 1 \right], \tag{3.4}$$

where T is the ambient temperature of the environment, and k stands for the Boltzmann constant. A typical time scale t of the s-process is about 10^3 years. Thus, there are only a few low-energy long-lived isomeric cases, when the assumption of thermal equilibrium might not be warranted, but they are out of the scope of this work.

In thermal equilibrium the population probability is determined by the Boltzmann distribution:

$$p_i = \frac{(2J_i + 1) \times \exp\left(-E_i/kT\right)}{\sum_m (2J_m + 1) \times \exp\left(-E_m/kT\right)}, \tag{3.5}$$

where p_i is the population of the ith-level with energy E_i and spin J_i at temperature T. The sum over m also includes the ground state. Therefore, the actual stellar decay rate

$$\lambda^* = \sum_i \left(p_i \times \sum_j \lambda_{ij} \right), \tag{3.6}$$

includes the decays of all thermally populated excited states i into the accessible levels j of the daughter nucleus. At 30 keV thermal energy, nuclear states at 100 keV excitation energy are typically populated with 1% probability. If, for example, this state can energetically decay by β-transition and its induced probability $\log ft$ differs from the ground state probability by $\Delta \log ft = 5$, then such a state decays 10^5 times faster than the ground state, what implies, to a first approximation, a stellar enhancement by a factor $10^5 \cdot 0.01 = 10^3$ (see Fig.3.2).

Based on Fermi's golden rule the individual β-decay rate λ_{ij} is basically the superposition of the nuclear matrix element (NME) and the phase space factor (see Eq. (2.8) or Eq. (2.11)). The phase space factor can be measured experimentally, whereas the NME is the matter of theoretical calculation. However, reliable calculations of NMEs together with the estimation of their uncertainties are very challenging. Usually these calculations are done only for highly necessary cases such as, for example, neutrinoless double beta-decay or double electron capture [71].
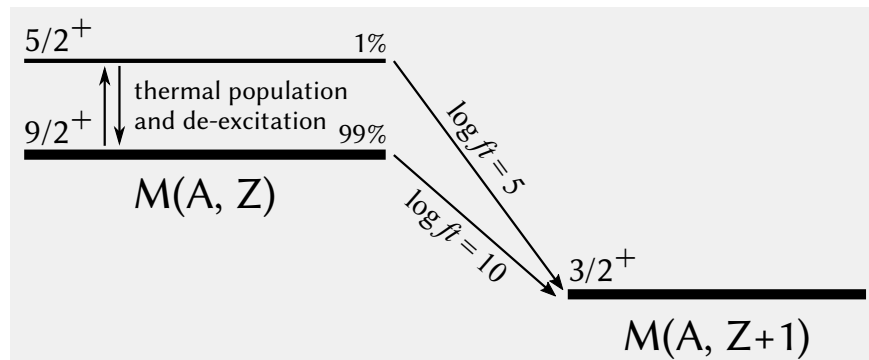
Figure 3.2: An example to demonstrate the β^--decay enhancement effect due to the allowed β^--decay from the thermally populated low-lying nuclear state. In such a case the enhancement factor would be about 10^3. For explanation see text.

An alternative approach to estimate β-decay rates is to use so-called $\log ft$-values, where f is the integral of the product of the Fermi function $F_0(E,Z)$ and terms depending on electron energy/momentum, whereas t is the half-life of the β-transition. The $\log ft$-value may be thought of as a comparative half-life of a transition corrected for differences in atomic number Z and the electron momentum p_e, and thus reducing all half-lives to a comparable basis. If, for example, $\log ft$-value of a $(I_i \to I_{f1})$ β-transition is 10, but $(I_i \to I_{f2})$ between the same nuclei is only 5 and the energies of the transitions are comparable, then the latter transition would occur approximately 5 orders of magnitude faster. Hereby, in order to estimate the total comparative half-life it is necessary to know the $\log ft$-value and the population of each relevant energetically possible β-transition. About 3900 $\log ft$-values of observed ground-to-ground or ground-to-excited states transitions are tabulated in [72]. Alternatively, in http://www.nndc.bnl.gov/logft/ web-page one can use an advanced $\log ft$-value calculator, which gives the $\log ft$-value if all the input parameters, including $T_{1/2}$ and Q_β, are already known. The $\log ft$-values for transitions from exited nuclear states are experimentally known only for long lived isomeric states with non negligible β-γ branching. For transitions from short-lived states the $\log ft$-values can be found after a survey of observed β-transitions between the same initial and final nuclear configurations (Nilsson states). However, the absolute decay rate for these estimated transitions may be uncertain by a factor of 2 or so.

Now, coming back to the β-decay at high temperature stellar environment, it is clear that β-transitions from low-lying thermally populated states may have "less forbidden" type[1] then terrestrially known transition from the ground state, and despite of their small population may have significant impact on the total effective half-life of the nuclide.

---

[1]Beta-transitions are characterized by various degrees of "forbiddenness" [73], depending on the angular momentum carried away by the electron and neutrino. "Allowed" transitions are those in which the nuclear spin doesn't change by more than one unit of angular momentum and the parity of the nuclear states is the same. The successively larger changes of angular momentum with alternating changes of parity are subdivided in numbers of degree of "forbiddenness".

3.3 Bound-state β^--decay

Apart from the well-known continuum β^--decay, there is a probability of a bound state β^--decay (shortly β_b-decay), when the β-particle (electron) is emitted not to the continuum, but to a non-occupied atomic orbit of the daughter atom, as shown in Fig. 3.3. For neutral or moderately ionized atoms, β_b-decay is restricted to very weakly bound electron states of the daughter atom, because the inner orbitals are Pauli blocked. The result is that β_b is only a marginal decay branch of neutral or moderately ionized atoms. Whereas in almost all EC decays a characteristic X-ray is signaling the transition, a corresponding signature after β_b-decay is in general missing[1]. This specific property makes the experimental investigation of β_b-decay rather difficult. Thus, for most of the s-process nuclides the impact on the total half-life of the β_b-decay process can only be theoretically calculated.

The possibility that β_b-decay process may exist was first considered in 1947 [74]. Since then many theoretical calculations have been performed for β_b-decay such as for a neutron, tritium, neutral and highly ionized heavy atoms. The investigations of highly ionized heavy atoms [75, 76] have shown the extreme importance of the β_b-decay process for the nuclides related to the nucleocosmochronometry. Several heavy ions such as, for example, fully ionized ^{163}Dy, ^{187}Re, and ^{205}Tl are expected to exhibit significant effects. Calculations say that these nuclides decay only through the β_b process, with the estimated half-lives of about 50 d, 14 yr, and 120 d, respectively [77], although the neutral atoms are stable or very long-lived. The reason of such a strong effect is due to their low Q_β-values. The low Q_β-values allow the energetics of the β-transitions to be highly depend on the degree of ionization, resulting in changes of rates for both of continuum-state and bound-state decays. This dependence is simply because the atomic binding energies liberated by ionization, i.e., the total electron binding in the neutral atom, B_{tot}, increases with Z as described in Sec. 3.1. Thus, for reliable calculations of β_b-decay probabilities of the relevant nuclides their low-energy Q_β-values have to be accurately and precisely measured.

3.4 Other effects

Nuclei that terrestrially decay via electron capture may decay in stellar interiors by the capture of free electrons (free EC) from the surrounding hot dense plasma. The rate of the free EC reaction is proportional to the probability that a continuum electron is present at the nucleus where it can be captured. The probability of finding an electron at the nucleus is in turn proportional to the electron density and inversely proportional to the average electron velocity, which for non-degenerate electrons depends on the square root of the temperature. Thus, the rate of free EC reaction depends strongly on the local electron temperature and density [79, 80]. At typical s-process densities, electron concentrations are of the order of 10^{27}cm^{-3}, which means that electron capture from the continuum is no longer negligible, especially at EC decay energies below 30 keV [13].

---

[1]Except for very special cases, when, for example, a bare or H-like parent atom β_b-decay to the L- or M-shell of the daughter atom with the subsequent characteristic X-ray emission.
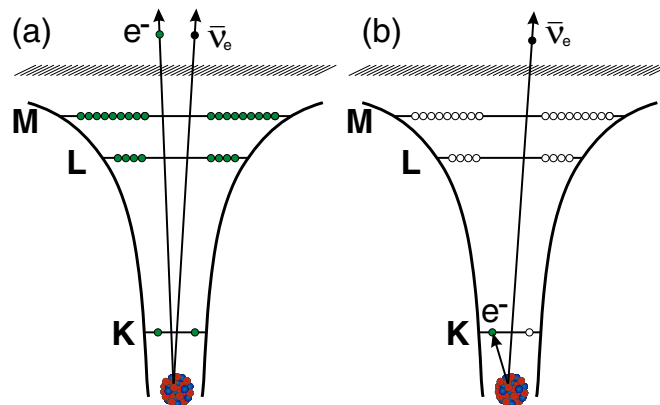
Figure 3.3: Continuum β^--decay of a neutral atom (a) and β_b-decay of a fully ionized atom to the K-shell of the daughter atom (b), "saving" the K binding energy and thereby raising the Q-value. Figure is taken from [78].

There are a few other effects to be taken into account for the calculation of β-decay in the stellar environment. For instance, the screening effect of the decaying nucleus by surrounding charged particles affect the radial dependence of the wave function for the created electron and hence alter the β^--decay rates. The screening changes the total β-decay rates by at most 10 to 15 percent for low-energy β-decaying nuclei [79]. Another effect which may arise is due to the exclusion principle. The free-electron concentrations that exist in stellar interiors are sometimes large enough and the Fermi-level is so high that the number of states available to the decay electron is significantly decreased in accordance with the exclusion Pauli principle [81].

All these additional effects are given here only for completeness. Estimations of these effects are hampered not by uncertain Q_{EC}-values of considered nuclei, but rather by imprecise knowledge of stellar medium conditions. A summary of all the thermal effects influencing stellar β-decay rates is given in [13]. In the framework of the thesis it was necessary to emphasize that the decay rates of nuclides with terrestrially low β-decay energies are highly affected by the hot and dense stellar environment. The most important influential factors are highlighted above with the focus on the necessity of highly accurate knowledge of the Q-values.

4. Basics of Penning traps

The first experimental realization of the device, where charged particles were confined by superposition of a homogeneous magnetic field and a quadrupolar electrostatic potential, was done by Dehmelt in 1959 [82]. In 1989 Dehmelt was honored with the Nobel Prize. He also coined the name "Penning trap", in recognition of F.M. Penning for the idea of the charged particle confinement, although Penning's idea was implemented in the context of vacuum gauges where only radial confinement by means of an axial magnetic field takes place. Since then, the Penning traps are commonly used for already 60 years, being mainly focused on the high-precision measurements of masses and magnetic moments. High precision is based on the tough confinement of the particle in space with consequent cyclotron frequency measurements. Tough confinement reduces all the possible systematic effects, whereas the frequency measurement principle is the most precise one: «Never measure anything but frequency!», - said Arthur Schawlow, the 1981 Nobel Prize winner in physics.

Nowadays, Penning-trap physics is well studied. There are hundreds of papers and theses explaining the Penning-trap physics in details. All of them start with the description of the ion motion in an ideal trap: perfectly homogeneous axial magnetic field with superimposed quadrupolar electric field. This is rather simple and for the consistency will be given in this thesis as well. Difficulties, however, arise in the real world, where there are many imperfections and instabilities, which limit the achievable precision or, if not properly taken into account, lead to an erroneous result. The higher we aim in precision, the more effects have to be taken into account. In Sec. 4.3 only those effects which pertain to the current measurement are highlighted. In Sec. 4.4 the used two different frequency detection methods are introduced, but again only necessary aspects are detailed.

4.1   The ideal Penning trap

The key condition for a high-precision experiment is the confinement of a particle in an as small as possible volume for an as long as possible time. Penning traps are the best tools so far which can provide these conditions. Moreover, Penning traps use the very basic concept for the mass measurements: in a uniform magnetic field the angular frequency of a particle is inversely proportional to its mass. Indeed, when an ion with the mass m and charge q is moving through a magnetic field $\vec{B} = B_0 \hat{z}$ it experiences the Lorentz force $\vec{F}_L = q[\, \vec{v} \times \vec{B}\,]$ and hence the ion is radially confined. By equating $\vec{F}$ to centripetal force $\vec{F}_c = m\vec{v}^2/r$ one

can deduce the so called "free cyclotron frequency"

$$\nu_c = \frac{1}{2\pi} \frac{|q|}{m} B. \tag{4.1}$$

For the full three-dimentional confinement the electrostatic field with a potential minimum in the axial direction has to be created[1]. Ideally, in order to attain a harmonic confinement (when the frequency is amplitude independent), an electrostatic potential has to have the quadratic form:

$$\phi(r,z) = \frac{C_2 U_0}{2d^2} \left(z^2 - \frac{r^2}{2} \right), \tag{4.2}$$

where U_0 is the voltage difference applied to a suitable electrode structure and (r,z) are cylindrical coordinates with $r = \sqrt{x^2 + y^2}$. The dimensionless coefficient C_2 reflects the strength of this potential determined by the trap geometry. The trap geometry is expressed in the characteristic trap dimension d term as

$$d^2 = \frac{1}{2} \left(z_0^2 + \frac{r_0^2}{2} \right), \tag{4.3}$$

where parameters z_0 and r_0 are depicted in Fig. 4.1.
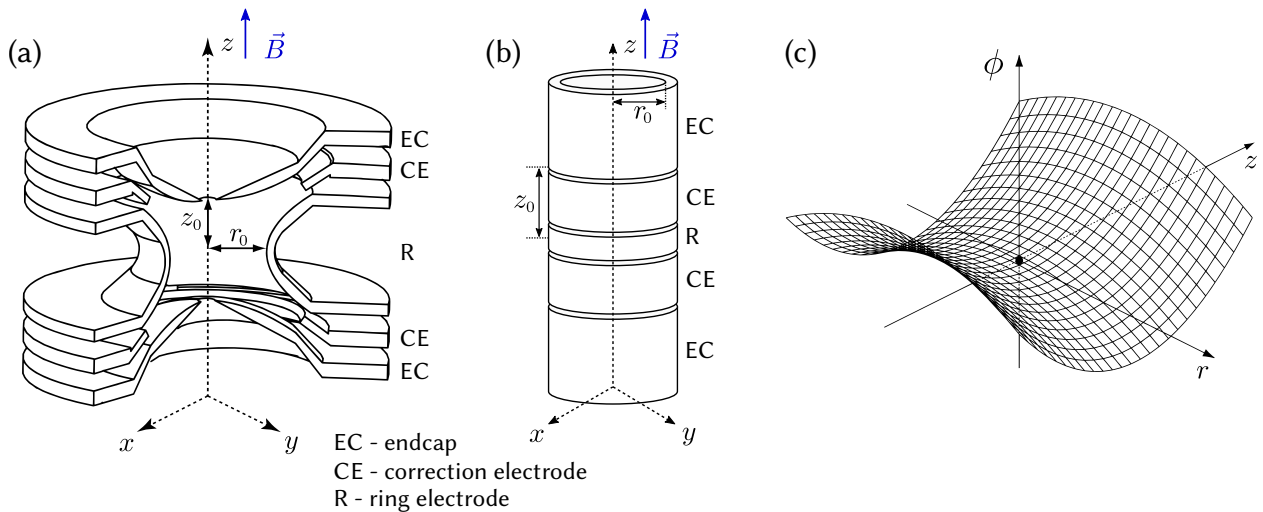
Figure 4.1: A sketch of a hyperboloidal (a) and a cylindrical (b) Penning trap. (c) the equipotential surface of the quadrupolar electrostatic potential ϕ created in the center of the trap for the ions' axial confinement.

Now, in the presence of both the quadrupolar electrostatic field and the homogeneous magnetic field, the equation of motion is governed by the total Lorentz force

$$\vec{F} = q \left(-\vec{\nabla}\phi + \vec{v} \times \vec{B} \right) = m\ddot{\vec{r}}. \tag{4.4}$$

---

[1]Earnshaw in 1842 pointed out that three-dimensional confinement of charged particles by purely electrostatic or, respectively, static magnetic fields is impossible [83].

The solutions are the three independent harmonic motions with frequencies

$$\nu_z = \frac{1}{2\pi}\sqrt{\frac{2qU_0C_2}{md^2}}, \quad \nu_- = \frac{1}{2}\left(\nu_c - \sqrt{\nu_c^2 - 2\nu_z^2}\right), \quad \nu_+ = \frac{1}{2}\left(\nu_c + \sqrt{\nu_c^2 - 2\nu_z^2}\right), \quad (4.5)$$

where ν_z, ν_-, ν_+ are the axial, magnetron and modified cyclotron frequencies, respectively (see Fig. 4.2). Typically, Penning traps make use of a strong homogeneous magnetic field and a weak electrostatic field, which results in the hierarchy

$$\nu_+ \gg \nu_z \gg \nu_-. \quad (4.6)$$

From these eigenfrequencies calculated for the ideal trap, one can derive the two very important relations:

$$\nu_c = \nu_+ + \nu_-, \quad (4.7)$$

$$\nu_c^2 = \nu_+^2 + \nu_-^2 + \nu_z^2. \quad (4.8)$$

Thus, the ion's free cyclotron frequency ν_c can be calculated after determination of the eigenfrequencies, either following Eq. (4.7) or Eq. (4.8). While the first relation holds exactly for the ideal trap, the latter one is more robust with respect to the trap imperfections and is usually referred to as the "Brown-Gabrielse Invariance Theorem" [84]. However, all the measurements performed in the framework of this thesis did use only Eq. (4.7), showing that relative precision of a few 10^{-10} can still be achieved.
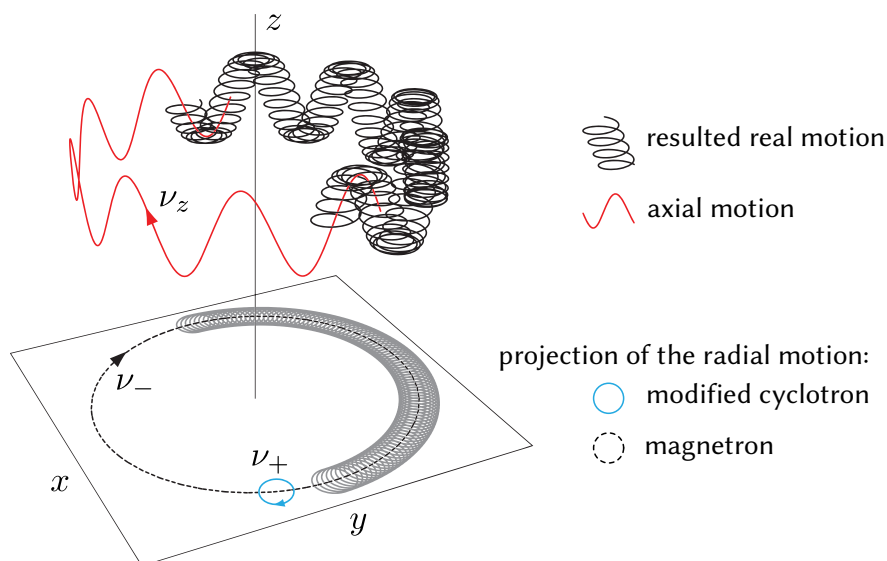

Figure 4.2: An example of a three-dimensional ion motion in a Penning trap and its projection onto the radial plane. Note that the amplitudes of the eigenmotions can be arbitrary and in this example are chosen such that the resulting motion is well visible.

An important feature of the Penning trap is the independence (to the first order) of the magnetron frequency on the particle properties. It can be seen after a series expansion of ν_- in Eq. (4.5):

$$\nu_- \approx \frac{1}{4\pi}\frac{C_2 U_0}{Bd^2}. \quad (4.9)$$

In particular, this peculiarity is used for the selective buffer-gas cooling technique, which is described in Sec. 4.3.

4.2 Mass determination principle

As it is seen from Eq. (4.1) the mass m of an ion is inversely proportional to the free cyclotron frequency ν_c, which can be measured to a very high precision in a Penning trap. However, another two ingredients, namely the absolute charge q and the strength B of the magnetic field, are not known to the similar precision. These uncertainties vanish to a large extend when using the mass ratios

$$\frac{m_1}{m_2} = \frac{q_1}{q_2} \cdot \frac{B(t_1)}{B(t_2)} \cdot \frac{\nu_{c_2}(t_2)}{\nu_{c_1}(t_1)},\qquad(4.10)$$

where t_1 and t_2 are the times at which the cyclotron frequencies of two different ion species are alternately measured. The ratio q_1/q_2 is a rational number due to the quantization of charge, and within this thesis it is equal to unity since only single charged ions were used. If the two cyclotron frequencies are measured at the same time, i.e. $t_1 = t_2$, the magnetic-field ratio cancels out and the relation reduces to the simple ratio

$$R \equiv \frac{m_1}{m_2} = \frac{\nu_{c_2}}{\nu_{c_1}}.\qquad(4.11)$$

The frequency ratio R can be used for the determination of the atomic mass differences. Thus, the mass of a singly charged ion is

$$m_{\text{ion}} = M - m_e + B_e,\qquad(4.12)$$

where M is the mass of the neutral atom and B_e is the binding energy of the valence electron. Thus, the mass difference between two atoms − the Q-value − can be expressed as

$$Q = M_1 - M_2 = (M_2 - m_e)(R - 1) + R \cdot B_2 - B_1.\qquad(4.13)$$

The difference in electron binding energies of valence electrons is in the order of a few eV or even below, and hence the last two summands in Eq. (4.13) can be neglected at the present limit of precision. Then the expression (4.13) is reduced to

$$Q \equiv M_1 - M_2 = (M_2 - m_e)(R - 1),\qquad(4.14)$$

and the final relative uncertainty of the measured Q-value is given by

$$\frac{\delta Q}{Q} = \sqrt{\left(\frac{\delta M_2}{M_2 - m_e}\right)^2 + \left(\frac{\delta m_e}{M_2 - m_e}\right)^2 + \left(\frac{\delta R}{R - 1}\right)^2}.\qquad(4.15)$$

Besides the Q-value, the frequency ratio $R = \nu_c^{\text{ref}}/\nu_c$ can be used for the absolute atomic mass M_{atom} determination if the mass M_{ref} of the reference atom is well known:

$$M_{\text{atom}} = \frac{\nu_c^{\text{ref}}}{\nu_c}(M_{\text{ref}} - m_e) + m_e.\qquad(4.16)$$

In this case both the uncertainty of the atomic mass of the reference ion δM_{ref} and the uncertainty of the frequency ratio R equally contribute to the uncertainty of the mass determination of the ion of interest according to

$$\frac{\delta M_{\text{atom}}}{M_{\text{atom}}} \simeq \sqrt{\left(\frac{\delta M_{\text{ref}}}{M_{\text{ref}}}\right)^2 + \left(\frac{\delta R}{R}\right)^2 + \left(\frac{\delta m_e(1-R)}{RM_{\text{ref}}}\right)^2}. \qquad (4.17)$$

Ideally ^{12}C or its clusters should be used as a reference ions due to the direct connection to the definition of the atomic mass unit [85]. Commonly, ^{133}Cs is used as the reference owing to its well known mass and the simplicity of the ion production. Nevertheless, the reference ion should have the closest mass to the ion of interest as possible, otherwise the systematic error due to the mass dependent frequency shifts may have the dominant contribution to the total error budget [86].

4.3   The real Penning trap

Equations (4.5)−(4.8) describe the undisturbed motion of a single particle in an ideal Penning trap, where eigenfrequencies are totally decoupled and dependent only on the dimension of the trap, the electric and magnetic field strengths, the mass m and charge q of the stored particle. However, this explanation turns out to be too simple for a real Penning trap, where several deviations from the ideal geometry due to the field inhomogeneities, field instabilities, axes misalignment and other imperfections have to be taken into account. The imperfections lead to systematic shifts of the ion frequencies. All the shifts have to be estimated and, if necessary, corrected for. The uncertainties in the shift corrections give rise to the systematic error of the measurement, which in some cases may fundamentally limit the final precision of the mass measurements.

In general, the source of the systematic shifts of the eigenfrequencies can be either common for all Penning traps (e.g. inhomogeneity of the B-field or anharmonicity of the E-field), or dependent on the used detection technique. In this section only the common sources of the systematic shifts are highlighted, whereas effects specific to the used detection method can be found in the corresponding sections of Chapter 5 and 6.

4.3.1   Magnetic field fluctuations

According to Eq. (4.10) the magnetic-field ratio cancels out only if the two cyclotron frequencies are measured exactly at the same time $t_1 = t_2 = t$. The SHIPTRAP [87] and ISOLTRAP [88] spectrometers are not capable of that, therefore the magnetic-field ratio doesn't cancel out and leads to a shift in the inferred mass ratio. The resulting uncertainty strongly depends on the actual temporal fluctuations of the magnetic field. The effects responsible for irregular changes of the magnetic field of a superconducting magnet are the following:

1. Every material is magnetic to some extend. The magnetic permeability of a material is temperature dependent. Therefore, the magnetic field dependents on the temperature of the materials surrounding the superconducting coil.

2. The boiling point and consequently the temperature of the liquid helium depends on the pressure. The temperature of a material which is in direct contact with the liquid helium depends on the pressure. Hence, the magnetic field depends on the pressure in the helium reservoir.

3. Ferromagnetic materials moving around or brought close to the superconducting magnet disturb the field.

4. The magnetic field steadily decays due to the reduction of the current circling in the superconducting coil (flux creep phenomenon [89]).

The first effect can be minimized by the temperature stabilization of the experimental hall or at least of the volume between the magnet bore and the vacuum tube. The second effect can be minimized by the stabilization of the pressure in the helium reservoir of the magnet. It is clear how to avoid the influence of the third effect, however the fourth effect being the feature of the superconductivity can not be controlled. The influence of the total residual magnetic field fluctuations on the frequency measurements can be further minimized by measuring in as short time intervals as possible and alternating between the ion species. In order to extract the frequency ratio R from alternating measurements, either a linear or polynomial interpolation method can be applied, which are described in the following subsections.

Linear interpolation method

In the linear interpolation method it is assumed that the magnetic field between two measurements can be well approximated by the linear function. Thus, the cyclotron frequency $\nu_{c_2}(t_a)$ of the reference ion at the time t_a when the cyclotron frequency $\nu'_{c_1}(t_a)$ of the ion of interest was measured is given by (see Fig. 4.3(a))

$$\nu'_{c_1}(t_a) = \nu_{c_1}(t_b) + \frac{t_a - t_b}{t_c - t_a}\left[\nu_{c_1}(t_c) - \nu_{c_1}(t_b)\right], \tag{4.18}$$

where t_b and t_c are the measurement times of the ion of interest. The single ratio $R_i(t_a)$ at the time t_a, when $\nu_{c_2}(t_a)$ is measured, is given by

$$R_i(t_a) = \frac{\nu_{c_2}(t_a)}{\nu'_{c_1}(t_a)}. \tag{4.19}$$

The relative uncertainty of R_i is given by

$$\frac{\delta R_i}{R_i} = \sqrt{\left(\frac{\delta\nu_{c_2}}{\nu_{c_2}}\right)^2 + \left(\frac{\delta\nu'_{c_1}}{\nu'_{c_1}}\right)^2}, \tag{4.20}$$

with $\delta\nu_{c_2}$ denoting the measurement uncertainty of the ion «2», and $\delta\nu'_{c_1}$ the total uncertainty of the interpolated frequency of the ion «1» which is defined as

$$\delta\nu'_{c_1} = \sqrt{\left(\delta\nu_{c_1}(t_b)\right)^2\left(\frac{t_c - t_a}{t_c - t_b}\right)^2 + \left(\delta\nu_{c_1}(t_c)\right)^2\left(\frac{t_a - t_b}{t_c - t_b}\right)^2}. \tag{4.21}$$

Non-linear fluctuations of the cyclotron frequencies are not covered within the linear interpolation. However, if such deviations are known as a function of time, they can in principle be taken into account by an additional non-linear uncertainty added quadratically.
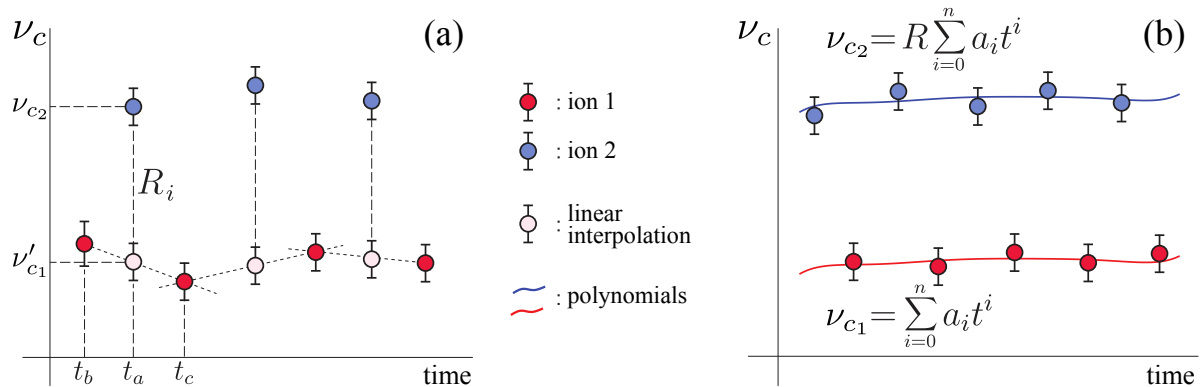
Figure 4.3: (a) Schematic diagram of the interpolation method. The frequency of the reference ion «2» measured at times t_b and t_c is linearly interpolated to the measurement time t_a, at which the ion of interest «1» is measured, and then the single ratio R_i is calculated. (b) Schematic diagram of the polynomial evaluation method. The polynomials $\nu_{c_1} = \sum_{i=0}^{n} a_i t^i$ and $\nu_{c_2} = R \sum_{i=0}^{n} a_i t^i$ are simultaneously fitted to the frequency data sets of the ion «1» and ion «2», and then the frequency ratio R being the fit parameter is directly extracted from the fit.

Polynomial method

An alternative way of the frequency ratio R determination from the alternating measurements is the approximation of the cyclotron frequency drift by a polynomial of n-th order

$$\nu_c(t) \approx \sum_{i=0}^{n} a_i t^i. \tag{4.22}$$

The ratio R can be determined from a simultaneous fit to both alternating frequency data the polynomials $P_1(t) = \sum_{i=0}^{n} a_i t^i$ and $P_2(t) = R \cdot P_1(t)$ as shown in Fig. 4.3(b). The advantage of this method over the linear interpolation is that it is less sensitive to random and fast fluctuations of the magnetic field which may show up as outlying data points. However, the choice of the order n of the polynomial and the duration of the fitted interval are important. If n is chosen too low, not all bumps of the long-term drift will be mapped, while a polynomial with too high order will tend to pin all the random noise and short-term fluctuations on top of the drift. In the absence of any knowledge concerning the real magnetic-field behavior besides the measured data points, the choice of the polynomial order is based on the statistical methods. The options for quantifying the fit quality are, for example, looking at χ^2_{red} or applying the so-called F-test. The detailed description and application of these methods can be found in [90] and the references therein.

4.3.2 Electrostatic anharmonicities

In a real Penning trap it is technically challenging to perfectly align the axis of the electrostatic field, defined by the trap electrodes, with the direction of the magnetic field given by the superconducting magnet. Furthermore, the electrostatic potential is never a perfect quadrupolar field due to the machining imperfections, the finite length of real trap electrodes, segmentation of the electrodes for ion manipulation, misalignment of the trap

electrodes or electrostatic potential offsets. In the presence of such imperfections the harmonic eigenmotions are no longer independent and become coupled.

The electrostatic potential near the trap center can be written as a fundamental solution to Laplace's equation $\nabla^2 \phi(r,z) = 0$ in spherical polar coordinates (r, θ, φ) using Legendre polynomials:

$$\phi(r, \theta) = \frac{U_0}{2} \sum_{i=0}^{\infty} C_i \left(\frac{r}{d}\right)^i P_i \left(\cos \theta\right). \tag{4.23}$$

This solution is cylindrically symmetric because the angular variable φ, which is the same for spherical and cylindrical coordinates, is absent. Hence, due to the cylindrical rather than spherical symmetry, the imperfections are best treated in cylindrical coordinates (r, z) [91]:

$$\phi(r, z) = \frac{U_0}{2} \sum_{i=0}^{\infty} \frac{C_i}{d^i} \sum_{j=0}^{i} \frac{i! \, (-1)^{j/2}}{(i-j)! \left(\frac{j}{2}!\right)^2 2^j} r^j z^{i-j}. \tag{4.24}$$

Since the cylindrical electrodes have reflection symmetry across the $z = 0$ plane, the potential $\phi(r, z)$ must be even in z, and as a result the coefficients C_i in Eq. (4.23) and Eq. (4.24) are non-zero only for even values of i, and zero for odd i. Thus, for clarity a first few terms of a real trap potential are

$$\begin{aligned}
\phi(r, z)/U_0 = {} & \frac{C_0}{2} \\
& + \frac{C_2}{2d^2} \left(z^2 - \frac{1}{2}r^2\right) \\
& + \frac{C_4}{2d^4} \left(z^4 - 3r^2 z^2 + \frac{3}{8}r^4\right) \\
& + \frac{C_6}{2d^6} \left(z^4 - \frac{15}{2}r^2 z^4 + \frac{45}{8}r^4 z^2 + \frac{5}{16}r^6\right) \\
& + \dots .
\end{aligned} \tag{4.25}$$

The dimensionless coefficients C_i are the pure functions of the electrode geometry and the applied voltages, which directly classify the anharmonicities within a real trap. In a real trap, higher-order coefficients such as C_4, C_6 and C_8 (octupole, dodecapole and hexadecapole components of the potential) are present, which is commonly undesirable since their presence makes the oscillation frequencies of confined particles energy-dependent and consequently oscillation amplitude dependent [92]. The value of the corresponding frequency shift is proportional to the expansion coefficients, where the largest contribution usually comes via a non-zero C_4. In a real cylindrical Penning trap, C_4 and C_6 will certainly have non-zero values because of the cylindrical shape of the electrodes, machining imperfections, misalignments and so forth. In precision measurements, it is necessary to remove higher-order coefficients so that frequencies remain independent from the oscillation amplitudes to a large extend. One method to eliminate these anharmonicities is to properly choose the trap geometry, whereas the fine-tuning can be done "on-line" by setting up appropriate potentials on compensation electrodes while detecting the ion's signal.

4.4 Ion manipulation and detection

For high-precision mass measurements, the preparation of a pure ion cloud of only a single species, cooling of the ion motions, and the determination of the free cyclotron frequency is essential. At SHIPTRAP and ISOLTRAP, the main technique for the ion cloud preparation is the mass-selective buffer gas cooling, while for the free cyclotron frequency determination either the ToF-ICR (Time-of-Flight Ion Cyclotron Resonance) or PI-ICR (Phase Imaging Ion Cyclotron Resonance) detection is used.

4.4.1 Buffer-gas cooling technique

The axial motion of an ion in a Penning trap as well as the reduced cyclotron motion can be damped by collisions with a neutral buffer gas. To avoid charge exchange processes, a noble gas, mainly purified helium, is used. At low collision energies of less than a few eV the interaction is dominated by a long-range interaction of an ion with a buffer-gas atom, which is polarized by the ion. This can be described by a viscous-drag model. A detailed description of damping effects in Penning traps can be found in [93, 94]. Here only the main conclusions are highlighted.

A damping force which acts on the ion with mass m and velocity v in the viscous-drag model is

$$\vec{F} = -2m\gamma\vec{v}, \tag{4.26}$$

where the damping coefficient γ derives from the ion mobility K as $2m\gamma = q/K$. By applying a quadrupolar excitation (π-pulse) at $\nu_{\mathrm{rf}} = \nu_- + \nu_-$ in the absence of the damping force we would observe a periodic interconversion of the radial motion modes (the so-called Rabi oscillations). In the presence of the damping force $\vec{F}$ the magnetron motion converts to the cyclotron motion with a subsequent cooling of the latter, i.e. the cyclotron radius shrinks, which is described as [93]

$$\left[\frac{\hat{r}_+(t)}{\hat{r}_-(0)}\right]^2 = \frac{exp^{-\tilde{\gamma}_1 t}}{1 - (\gamma/g)^2} \ \sin^2\left(t\sqrt{g^2 - \gamma^2}\right), \tag{4.27}$$

where g is a coupling constant proportional to the amplitude of the quadrupolar rf-field; $\tilde{\gamma}_1$ is a modified damping constant, which depends on the eigenfrequencies. Figure 4.4 shows behavior of the $\hat{r}_+(t)/\hat{r}_-(0)$ ratio in comparison to the non-damped pure Rabi oscillations. Since the interconversion process has a resonance at the ν_c frequency, which in turn depends on the charge-to-mass ratio, a reduction of the radii can be done mass selectively. Therefore, by applying a π-pulse at the side-band conversion frequency $\nu_{\mathrm{rf}} = \nu_- + \nu_- = \nu_c$ with a certain duration and amplitude, only ions of interest can be well centered and cooled in the presence of the buffer-gas. The application of this method for the purification of the ion cloud is described in Sec. 5.2.1.
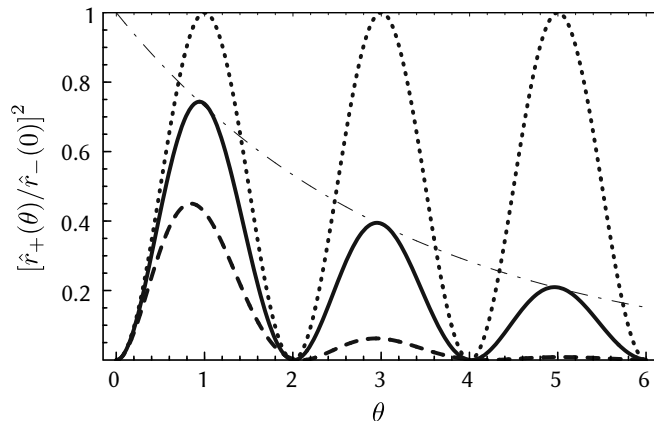
Figure 4.4: Degree of conversion of magnetron into modified cyclotron energy at exact resonance frequency $\nu_{\mathrm{rf}} = \nu_- + \nu_-$ as a function of time measured in units of the conversion time for the undamped case, $\theta = t/\tau_c$, where τ_c is the so-called "conversion time". In the absence of damping there is periodically full conversion and reconversion (dotted line), with damping the maxima are decreasing roughly exponentially (dash-dot line). Shown are curves for $\gamma/g = 0.1$ (solid line) and for $\gamma/g = 0.3$ (dashed line). The figure is reproduced from [93].

The ion cloud radial distribution can be described by the probability density function. Approximated by the Gaussian distribution, the full width at a half maximum W is given by[95]

$$W = \frac{2}{\pi\nu_+}\sqrt{\frac{\ln 2 \cdot kT}{m_{\mathrm{ion}}}} \approx \frac{3.3}{qB}\sqrt{m_{\mathrm{ion}}kT}, \tag{4.28}$$

where m_{ion} is the mass of an ion; T is the temperature of the buffer-gas. Thus the ultimate cooling performance is defined by the ion properties m and q, the strength of the magnetic field B and the temperature of the buffer-gas. For example, for ^{133}Cs$^+$ ions in a 7 Tesla magnetic field at room temperature buffer-gas the FWHM of their spatial radial distribution would be $W \approx 90\mu$m.

4.4.2 ToF-ICR technique

The Time-of-Flight Ion-Cyclotron-Resonance (ToF-ICR) detection technique is based on the measurement of the flight time of ions between the moments of ejection from the trap and hitting the detector (see Fig. 4.5). Being introduced in 1980 for proton-to-electron mass ratio determination [96] this technique was widely used for mass measurements of radioactive nuclides in Penning traps at many accelerator based facilities.

The ToF-ICR technique utilizes the orbital magnetic moment conservation low. The angular magnetic moment $\vec{\mu}$ of an ion in the Penning trap is given by

$$\vec{\mu} = -\pi q \left(\hat{r}_+^2 \nu_+ + \hat{r}_-^2 \nu_- \right) \vec{e}_z, \tag{4.29}$$

where $\hat{r}_+$ and $\hat{r}_-$ are the amplitudes of the corresponding radial motions. When the ion is ejected from the trap its magnetic moment interacts with the magnetic field gradient and the acting axial force is given by

$$\vec{F} = -\vec{\nabla}\left(-\vec{\mu}\vec{B}\right) = -\vec{\mu} \cdot \frac{\delta B}{\delta z}. \tag{4.30}$$
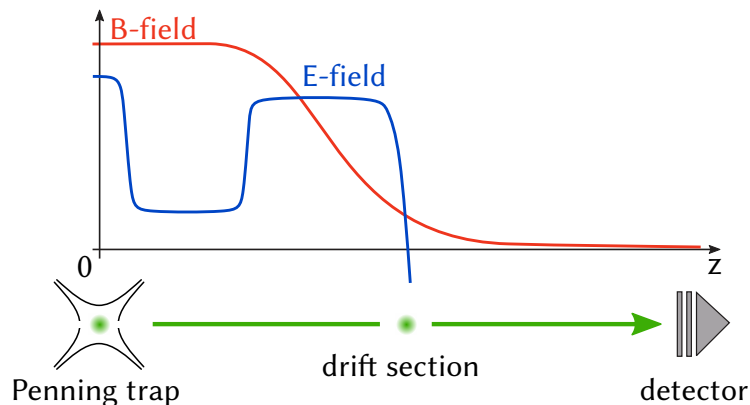
Figure 4.5: Schematic of the experimental setup for the TOF-ICR technique. The ions are ejected from the trap towards the detector through a magnetic field gradient (red line) in the drift section. In order to promote the adiabatic conversion of the radial into the axial ion energy the ions are slowed down in the magnetic field gradient by correspondingly applied electric potential (blue line) in the drift section.

Since the total energy of the ion motion has to be conserved, radial energy is converted into axial energy when the ion is ejected from the trap to a region with the vanishing magnetic field. It is worth noting, that Eq. (4.30), however, holds only if motion of the ion through the gradient of the magnetic field is performed adiabatically, i.e., slowly enough for the complete conversion of the radial into the axial ion energy[1] (see Fig. 4.5). Including the Coulomb force acting on the ion in a presence of electric potential $V(z)$ in the drift section, the time of flight is given by [97]

$$t(E_r) = \int_0^{z_{\mathrm{det}}} \sqrt{\frac{m/2}{E_{\mathrm{tot}}(E_r) - qV(z) - \mu(E_r)B(z)}} dz, \tag{4.31}$$

where $E_{\mathrm{tot}} = E_r + E_z$ is the total ion energy in the trap, $V(z)$ and $B(z)$ are the electric and magnetic fields along the ion path from the trap to the detector located at the position z_{det}. With good approximation of $\nu_+ \gg \nu_-$, the radial kinetic energy is given by $E_r \approx \mu B$. Therefore, as can be seen from Eq. (4.31) the time of flight depends on E_r, which in turn depends on the magnetic moment μ. Using this dependence, the measurement principle of the free cyclotron frequency of an ion is the following. After all the ion eigenmotions are cooled the magnetron motion is excited to a radius $\hat{r}_-$ by applying the dipolar excitation at ν_-. Consequently, the quadrupolar ν_{rf} pulse during a time T_{rf} is applied. For the resonant excitation pulse at $\nu_{\mathrm{rf}} = \nu_+ + \nu_- = \nu_c$ with the duration

$$T_{\mathrm{rf}} = \frac{4\pi^2 m(\nu_+ - \nu_-)}{qA_{\mathrm{rf}}}, \tag{4.32}$$

where A_{rf} is the amplitude of the rf-pulse, the slow magnetron motion is fully converted into the fast cyclotron motion and, thus, the radial kinetic energy E_r is maximized [97]. For non-resonant excitation with the detuning $\delta = \nu_c - \nu_{\mathrm{rf}}$, the conversion of the motions is

---

[1]Practically, in order to ensure this requirement the applied voltage profile on the extraction electrodes is set in such a way that the ion is slowed down in the strongest gradient of the magnetic field.

incomplete (see Fig. 4.6(a)). By sweeping the applied conversion frequency $\nu_{\rm rf}$ near ν_c and registering the time of flight of the ions, one can acquire the resonance spectrum. The center of the global resonance corresponds to ν_c. The typical ToF resonance is shown in Fig. 4.6(b).
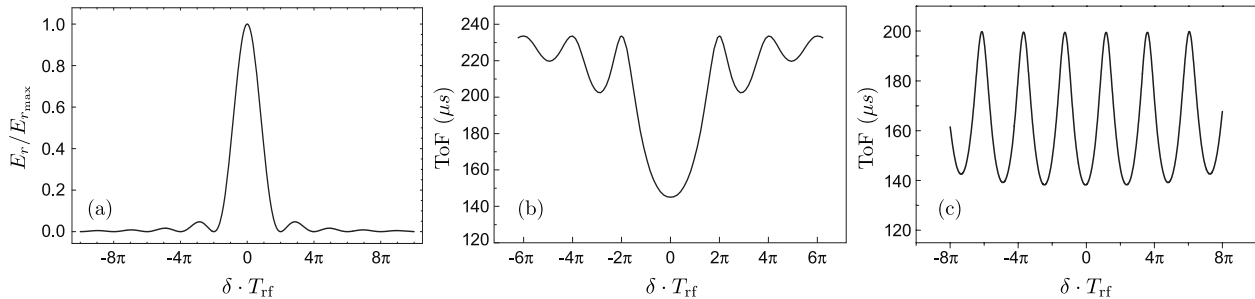

Figure 4.6: (a) Radial energy at the end of the quadrupolar excitation as a function of the detuning parameter δ. (b) Resulting time-of-flight spectrum $t(E_r)$. (c) Time-of-flight spectrum for the Ramsey type excitation scheme (for details see text). The times given here are arbitrary.

Apart from the quadrupolar excitation with a single pulse it is also possible to convert radial modes using two or more pulses doing a so-called Ramsey excitation scheme [98, 99]. The single excitation pulse with the duration $T_{\rm rf}$ and amplitude $A_{\rm rf}$ is replaced by two pulses with the duration $\tau_{\rm rf}$ and amplitude $a_{\rm rf}$ separated by a waiting time τ_0, while the the total power of applied excitation is kept constant, i.e. $T_{\rm rf}A_{\rm rf} = 2\tau_{\rm rf}a_{\rm rf}$. This elegant method reduces the line-width of the ToF resonance and makes the sidebands more pronounced and steeper (see Fig. 4.6(c)), improving the precision of the ν_c determination up to a factor three [100].

4.4.3 PI-ICR technique

Similar to the ToF-ICR technique, in the novel PI-ICR method the free cyclotron frequency ν_c is measured as the sideband coupling frequency, i.e. $\nu_c = \nu_+ + \nu_-$. The PI-ICR technique uses direct observation of the ion's radial motions on a high-resolution position-sensitive detector: a MCP with the delay line anode (shortly DLD $-$ Delay Line Detector). Precisely speaking, ν_c is determined by measuring the phases of ν_- and ν_+ ion motion, accumulated after a given phase-accumulation time. Additionally, the possibility of independent observation of both ν_- and ν_+ radial motions provides a beneficial tool for the tuning and characterization of the Penning trap.

The PI-ICR method offers a simultaneous increase in resolving power by a factor 40 and in precision by a factor 5 as compared to the ToF-ICR technique with the Ramsey excitation scheme [95]. Furthermore, the PI-ICR technique is faster, thus, in principle, allowing for mass measurements on nuclides with shorter half-lives than those which are accessible for the ToF-ICR detection. Actually, every Penning-trap mass spectrometer which utilizes the ToF-ICR technique can be readily upgraded up to PI-ICR technique by replacing the conventional MCP detector with an ion detector with position sensitivity.

For the radial frequencies determination the ion motion is projected onto the DLD by ejecting the ions from the trap and letting them hit the detector. The projection of the

ion motion on the detector is magnified by a factor G relative to the actual scale of the ion motions in the trap. The magnification factor G in the absence of an electric field can be estimated by using the Gauss's flux law:

$$G \approx \sqrt{B_z^{\mathrm{trap}}/B_z^{\mathrm{det}}}, \tag{4.33}$$

where B_z^{trap} and B_z^{det} are the axial components of the magnetic field in the trap and at the detector, respectively. Due to different kinds of misalignments and displacements the projection of the trap motion onto the detector is not only magnified, but also shifted and distorted. These effects and their impacts on the frequency determination have to be considered in the real experiment (see Sec. 5.4). In this section, for the sake of simplicity, only the basic idea of the PI-ICR method is described for the ideal case of the non-distorted projection.

Individual determination of the radial frequencies

Let us assume that the ions in the measurement trap are already well cooled, and hence are prepared at the center of the trap with the FWHM of their spatial distribution $2\Delta r$ defined by the cooling performance in the preparation trap (see Sec. 4.4.1). By applying a dipolar rf-pulse ν_{rf} at the corresponding frequency ν_- or ν_+ the ions are radially excited[1] to an average radius ρ and the initial phase is set. After a time t of the free evolution the radial ion motion is in its final phase and the total accumulated phase is $\varphi + 2\pi n = 2\pi\nu t$, where φ is the polar angle between initial and final phases, as shown in Fig. 4.7, n is the number of full revolutions, and ν is the radial frequency (either ν_- or ν_+). Thus, if time t is relatively short, then the number of performed full revolutions n can be reliably calculated, and by taking into account the measured phase φ, the trap frequency can be determined. Gradually increasing the phase-accumulation time t and controlling the number of revolutions n, the precision of the radial frequency determination can reach its ultimate value, where fluctuations of the magnetic and/or electric fields become dominant limiting factor.

Excitation-pulse schemes for the measurement of the magnetron ν_- and the modified cyclotron ν_+ frequencies are presented in Fig. 4.8 (left) and (right), respectively. Magnetron frequency measurement is the easiest case. First, a well cooled ion of interest is injected into the measurement trap. Due to some misalignment of the traps axis, after the transportation the ions may get non-negligible initial magnetron radius. However, for magnetron frequency measurement it is irrelevant, because this motion is anyway subsequently excited by the dipolar rf-pulse. After the excitation the ion is ejected and its reference phase is detected. For the final phase determination, the injection and excitation steps are the same, but now ejection and detection of the ion is done after some free phase-accumulation time t. Thus, the difference between reference and final phases is φ_-, while the total accumulated phase is $\varphi_- + 2\pi n = 2\pi\nu_- t$.

---

[1]By increasing radius of the magnetron motion the ions, actually, loose their energy since it is the metastable motion around an electric potential hill, while increasing radius of the cyclotron motion is indeed increases the ion energy and they get excited. However, by agreement in the Penning-trap community, if the amplitude of any trap motion is increased then it is simply said that the ions are got excited.
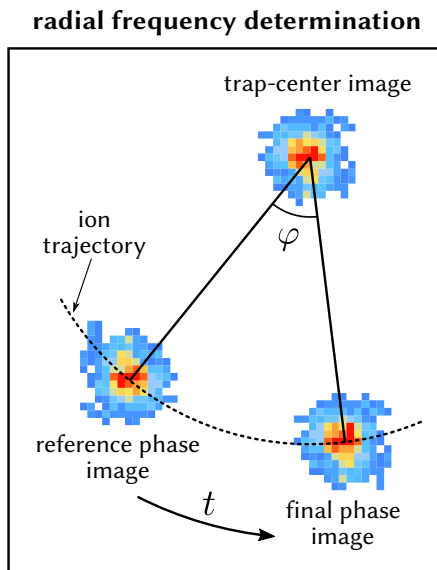
radial frequency determination

Figure 4.7: Projection of the radial ion motions in a Penning trap onto the position sensitive detector. The trap-center image is for the well-cooled radial motions of both coherent and incoherent components. The reference phase is the image of the radially excited coherent ion motion, whereas and the final phase is the phase-image of the same motion, but after a phase accumulation time t. For more details see text.

Measurement of the modified cyclotron frequency requires more steps. First, after the injection into the measurement trap the initial magnetron motion has to be damped (see Sec. 5.2.2), otherwise its presence will systematically shift the measured ν_+ frequency. In the next step the modified cyclotron motion is excitation by rf-pulse at ν_+. Then, before the extraction the fast cyclotron motion is converted into the slow magnetron motion via a quadrupolar rf-pulse at the cyclotron frequency[1]. A direct projection of the cyclotron motion is possible but results in a substantial angular spread on the detector due to the time-of-flight distribution of the ions[2]. Finally, just after the ν_+ motion is fully converted into ν_-, the ions are ejected and the reference phase is detected. For the final phase detection the ions undergo the same manipulations as for the reference phase, but now the conversion pulse is delayed, setting up the phase-accumulation time t. Hence, the total accumulated phase is $\varphi_+ + 2\pi n = 2\pi \nu_+ t$ from where the ν_+ frequency can be calculated.

For the trap-center image (1) the initial magnetron motion of the injected ions have to be damped and (2) the delay of ejection pulse have to scanned over the period of the magnetron motion in order to average out its remnants. Practically, the position of the trap-center image is stable enough and can be measured only once per day. The reference phase should also be stable and can be measured occasionally. The position of the final phase is the only quantity which has to be constantly measured. The sequentially measured both

---

[1]Note that the conversion of the modified cyclotron into magnetron motion preserves the modulus of the angle φ between the reference and the final phase of the corresponding motions although flips the sign of the angle.

[2]The smearing of the ToF peak is caused by the energy distribution of the ion's axial motion in the trap. The typical FWHM of the ToF peak is a few hundred ns, which is comparable to the period of modified cyclotron motion of heavy singly charged ions
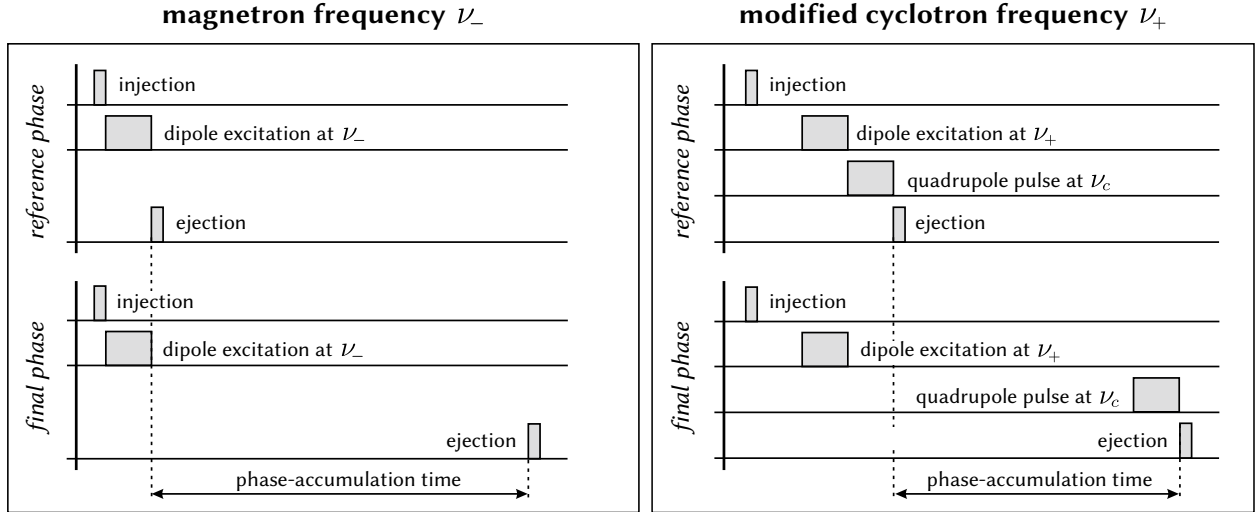
magnetron frequency ν_-   **modified cyclotron frequency ν_+**

Figure 4.8: Excitation-pulse scheme for the independent measurement of the magnetron (left) and modified cyclotron (right) frequencies. For details see text.

radial frequencies ν_- and ν_+ can result in the free cyclotron frequency as $\nu_c = \nu_- + \nu_+$. This approach, however, is less accurate compare to the one described in the following section Sec. 4.4.3. Instead, the direct radial frequencies measurements can be used, for example, for the harmonization of the trap potential (see Sec. 5.2.3), or for the temporal stability test of the voltage supplies for the trap electrodes.

Direct measurement of ν_c

Instead of summing the independently measured values of ν_- and ν_+, the alternative scheme presented in Fig. 4.10 allows the direct determination of the free cyclotron frequency ν_c. The excitation-pulse scheme consists of two patterns: the first one measures the so-called "magnetron phase" (ν_--image), the second one – the "cyclotron phase" (ν_+-image). These phases are depicted in Fig.4.9. The names are given after the dominant motion in each pattern. Indeed, in «pattern 1» after the conversion pulse the ions perform magnetron motion until the ejection, while in «pattern 2» they perform mostly the modified cyclotron motion because the conversion pulse is applied just before the ejection.

By applying the excitation-pulse scheme shown in Fig. 4.10, the relative phases $\alpha_\pm$ of the corresponding radial motions are

$$\alpha_\pm = \pm(2\pi n_\pm - 2\pi\nu_\pm t_\pm) + \alpha_0, \tag{4.34}$$

where $t_\pm$ is the phase accumulation time of either ν_+ or ν_- motion, α_0 is some initial phase, and the phases $\alpha_\pm$ are depicted in Fig. 4.9. Note, that the phases α_+ and α_- in Eq. (4.34) have opposite signs since the conversion of the modified cyclotron into magnetron motion flips the sign of the angle. Next, summing up phases α_- and α_+ with the assumption $t_- = t_+ \equiv t$ and taking into account Eq. (4.7) we finally derive the equation for the free
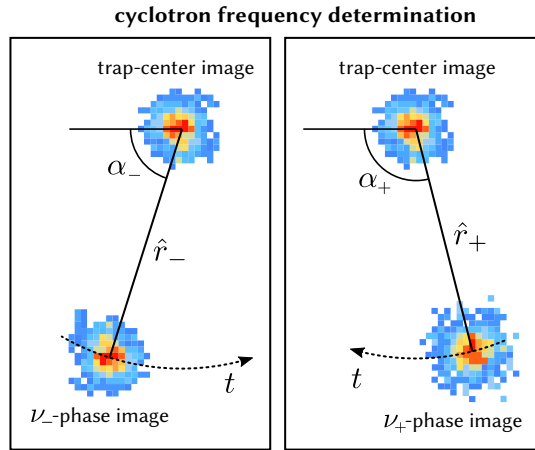
Figure 4.9: Projection of the radial ion motions in a Penning trap onto the position sensitive detector. The trap-center image is for the well-cooled radial motions of both coherent and incoherent components. The ν_-- and ν_+-phase images can be obtained if *pattern 1* and *pattern 2* in Fig. 4.10 are respectively applied. For more details see text.

cyclotron frequency determination

$$\nu_c = \frac{\alpha_c + 2\pi(n_- + n_+)}{2\pi t}, \tag{4.35}$$

where

$$\alpha_c = \alpha_- - \alpha_+. \tag{4.36}$$

Thus, ν_c frequency can be calculated by using Eq. (4.35) if the angle α_c is experimentally measured, while the number of full revolutions $n_\pm$ and the phase-accumulation time t are manually set.
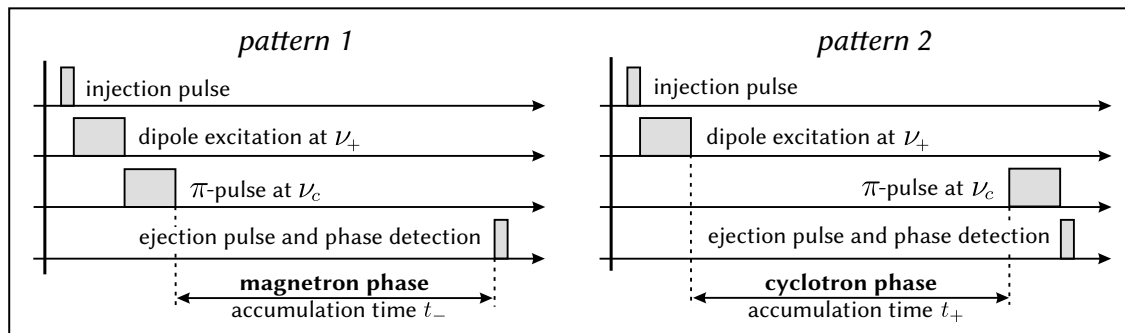
Figure 4.10: Excitation-pulse scheme for the direct measurement of ν_c. For details see text.
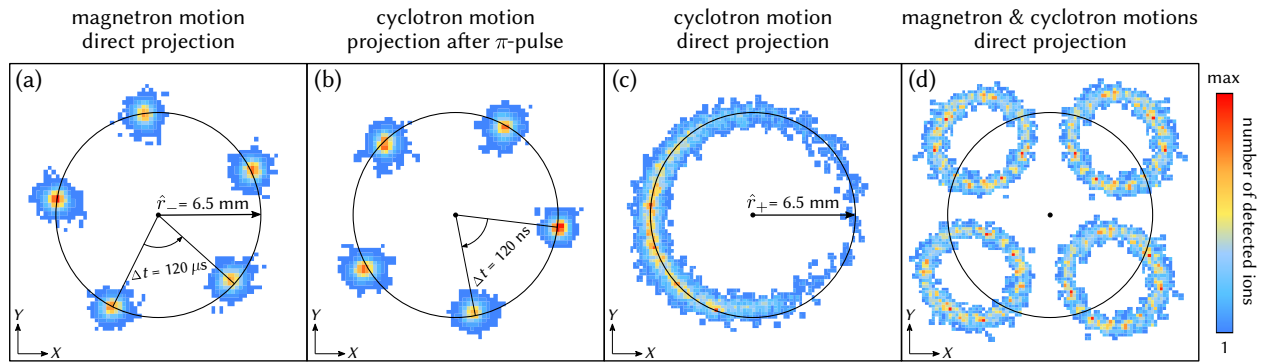
Figure 4.11: Projections of the position of ^{133}Cs$^+$ ions for several phases **(a)** of the magnetron motion and **(b)** of the cyclotron motion after its conversion with π-pulse. **(c)** Direct projection of the cyclotron motion with a certain phase onto the detector (FWHM of the ion's ToF distribution is 500 ns). **(d)** Direct projection of the radial-ion motion with non-zero magnetron and cyclotron radii for four phases of the magnetron motion.

5. The Penning-trap mass spectrometer SHIPTRAP

The SHIPTRAP mass spectrometer is the first Penning-trap installation for high-precision experiments of fusion-evaporation residuals. Though SHIPTRAP can investigate all neutron-deficient nuclides throughout the nuclear chart, this installation is targeted mainly to transuranium nuclides including superheavy elements. SHIPTRAP was named after the Separator for Heavy Ion reaction Products (SHIP) facility, which is world-wide well known for the discovery of super-heavy elements [101, 102]. A detailed description of the whole project and its achievements can be found in [87, 103]. Here, only a part of the facility which is relevant to the current measurements, namely «off-line SHIPTRAP», is presented. The off-line part of the facility consists of a station with the ion sources for production of singly charged ions from neutral species in various chemical forms, and of the heart of the system − the Penning-trap mass spectrometer.

5.1 Ion source

Singly charged ions are produced in a laser-ablation ion source [104] by irradiating the sample on a rotatable holder using a pulsed laser beam (see Fig. 5.1). The nuclides under investigation have to be virtually stable and must be provided in a sufficient amount. The mass differences of the considered isobaric pairs are so small that the parent and daughter ions can not be fully resolved even in the measurement trap. Therefore, in order to avoid systematic shifts of the cyclotron frequency due to the simultaneous presence of ions of different sorts in the measurement trap, the samples fixed on the sample holder are diametrically separated by about 2 cm. The used frequency-doubled Nd:YAG laser (532 nm) has an intrinsic pulse duration of 3-5 ns, while the pulse energy, which is typically in the range of 4-12 mJ, can be controlled remotely. The laser beam is focused by a telescopic lens system to a diameter of a millimeter at the sample, where the material is ionized after the laser induced desorption and fragmentation. The produced ions are mostly singly charged, higher charge states have never been observed at SHIPTRAP in the off-line mode.

A commercial surface ionization ion source is used to produce $^{133}Cs^+$ ions for test measurements. The advantage of this ion source is the reliability and stability. Unlike the laser ion source, where for the ion production a few parameters have to be properly optimized, the surface ion source has only a single parameter - the heating current. Moreover,

the count-rate of the surface ion source is more stable, what substantially helps for the optimization of the Penning-trap system.

The series of electrostatic electrodes and Einzel lenses transport the ions from the ion sources towards the Penning-trap mass spectrometer, as shown in Fig. 5.1. For the optimization of these transport sections a conventional micro-channel plate (MCP) detector, which can be placed in front of the entrance to the first trap, is used. When optimization of the transport section is done the MCP is replaced by the Einzel lens and the ions can fly further towards the traps. The acceptance of the first preparation trap (PT) is limited by its geometry, thus for the optimization of the injection section all the trap potentials are set to the "open" mode (indicated by the red line in Fig. 5.2) such that the ions can freely fly through the traps and be detected on the last MCP detector. The existence of the diaphragm between the two traps ensures that if the count-rate on the detector is maximized, then the whole ion transport section is well optimized.
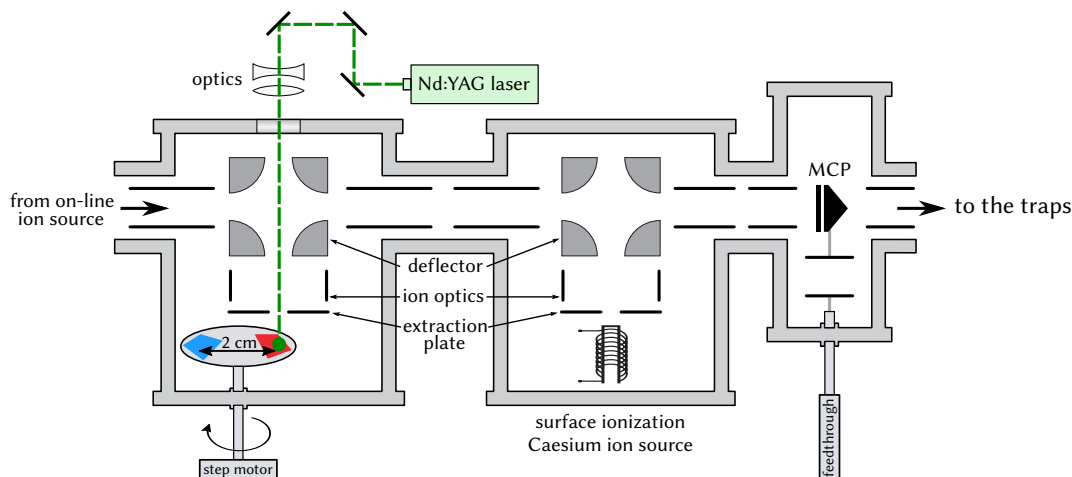
Figure 5.1: Schematics of the ion production section (not to scale). It consists of the laser ablation and the caesium-133 surface ionization ion sources together with the downstream first diagnostics unit.

5.2 Penning-trap system

The Penning-trap mass spectrometer has two cylindrical Penning traps: the preparation trap (PT) and the measurement trap (MT). They are placed in a magnetic field of 7 T created by a superconducting magnet (see Fig. 5.2). The traps are separated by a diaphragm with an inner diameter of 3 mm and a length of 52 mm. The geometry of the preparation trap was chosen in such a way as to maximize the capture efficiency. Thus, the ring electrode of the PT has a width of 18.5 mm in comparison with a 4.7 mm width of the MT ring electrode. The inner diameter of both traps is 32 mm.
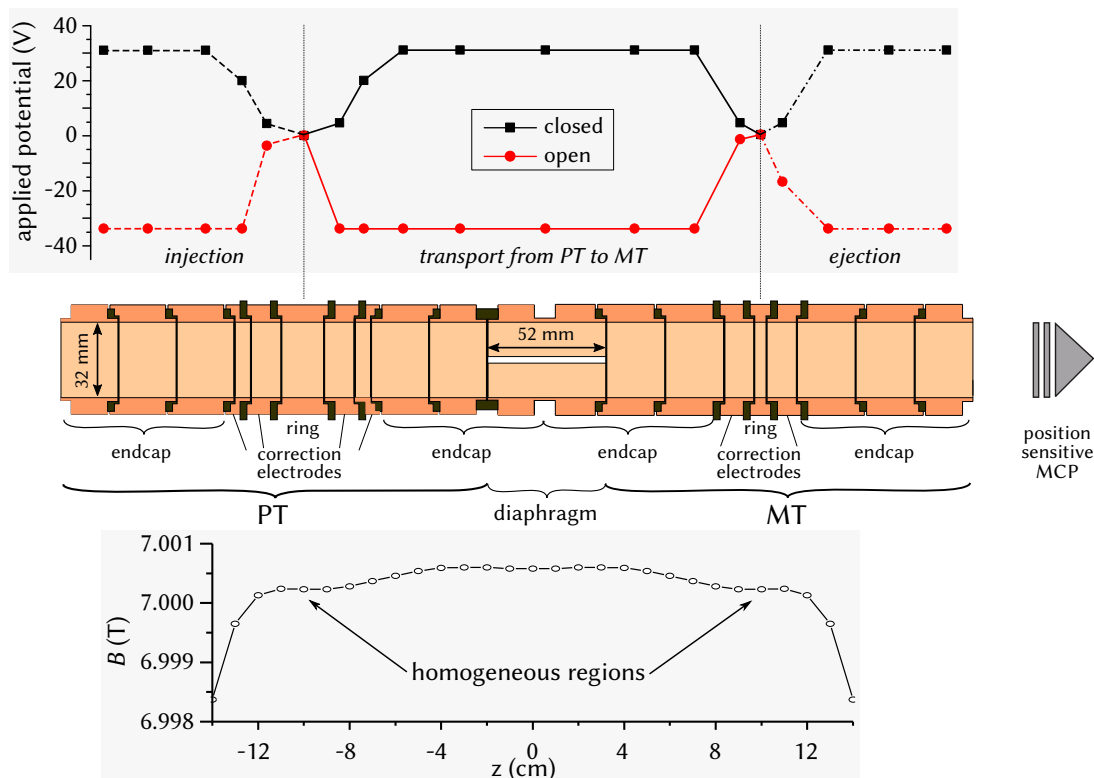
Figure 5.2: Middle: schematic picture of the Penning-trap tandem at SHIPTRAP. A 7-pole preparation trap (PT) with a wide central ring in order to maximize the capture efficiency, and a 5-pole measurement trap (MT) with the narrow ring and an orthogonal geometry. Traps are separated by a thin diaphragm and set according to the position of two homogeneous regions of a 7 T magnetic field (bottom). Voltages applied to the electrodes are shown on top. They are switched between closed and open configuration for a few tens of μs for: injection into the PT (dashed lines), transport from the PT to MT (solid lines), ejection from the MT towards the detector (dash-dotted lines).

5.2.1 Buffer-gas cooling in the preparation trap

The working principle of buffer-gas cooling technique is described in Sec. 4.4.1. The detailed characterization and optimization of the cooling procedure in the preparation trap during its commissioning phase is described in [105] using, however, a conventional MCP as the ion detector. The conventional MCP doesn't allow the direct test of the ion's radial spatial distribution. Therefore, in this case the mass-selective cooling is mostly dedicated to the isobaric separation with the resolving power of about 10^5 [106]. The general realisation of the buffer-gas cooling technique in a Penning trap can be found, for example, in [107, 108]. The recently invented PI-ICR method is based on the observation of the radial ion motion and, thus, the cooling performance is the key characteristics, which directly affects on the resolution and precision of the ν_c measurements. Therefore, the main steps in optimization of the buffer-gas cooling technique using a position sensitive micro-channel plate detector with the delay line anode (shortly the delay line detector − DLD) are highlighted in the following.

By applying a sequence of rf-pulses to the ring electrode, only ions of a certain mass are cooled and well centered and, when extracted, are able to pass through the diaphragm

(see Fig. 5.2). On one hand, the diaphragm makes the mass-selective cooling possible. On the other hand, it significantly reduces the buffer-gas flow from the PT into MT, where as low as possible pressure, typically below 10^{-7} mbar, is required. The cross section of the ring electrode with the corresponding lines for the rf-signals is schematically shown in Fig. 5.3(a). This is the minimal configuration to perform the buffer-gas cooling: an rf-signal at ν_- frequency is applied to one segment of the ring electrode making a dipolar excitation (Fig. 5.3(b)), while a quadrupolar signal is formed by applying an rf-signal at ν_c frequency to the other two opposite segments. The latter rf-pulse converts the magnetron to the modified cyclotron motion. The radial ion motion during the cooling process is schematically shown in Fig. 5.3(c). To avoid charge exchange processes and ion loses a 99.9998% purified helium at a typical pressure of a few 10^{-4} mbar is used as a buffer-gas. For even better purification the gas feeding line goes through a vessel filled with liquid nitrogen, where some contaminants are frozen out. To control the helium flow injected into the PT a fine-dosing valve (Pfeiffer EVR 116) is used.
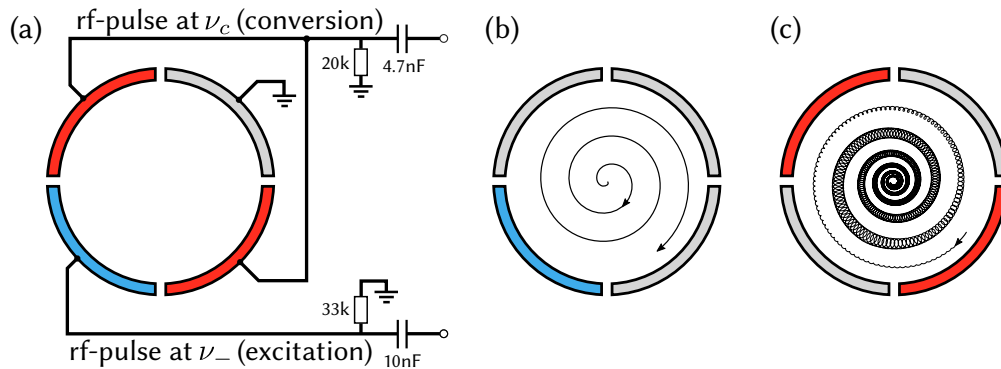
Figure 5.3: Transverse cut of a four-fold segmented ring electrode. (a) The minimal RF pulses configuration to perform the buffer-gas cooling technique in a Penning trap. (b) Magnetron excitation of initially centered ions to a certain radius. (c) Mass selective conversion of the slow ν_- motion to the fast ν_+ motion with consequent damping of the latter one in the buffer-gas.

During the optimization of the cooling procedure the ions are ejected from the PT and directly projected onto the DLD, while the MT is always kept open. Only cycles with ≤ 5 ions per shot are taken into account, otherwise the repulsion Coulomb force between the ions starts affecting their spatial distribution. Repeating the cycle and acquiring the statistics, the full width at a half maximum (FWHM) of the projection, which we call the "center spot", can be derived. Fig. 5.4 shows a typical radial spatial distribution of ^{133}Cs$^+$ ions after the well-optimized cooling procedure. The spot has roughly 2×2 mm^2 size and is positioned approximately in the center of the detector, which is 40 mm in diameter. The actual size of the center spot depends on the cooling performance and the magnification factor G. At SHIPTRAP the estimated magnification factor according to Eq. (4.33) is $G \approx 21$, whereas the minimal width of the cooled ^{133}Cs$^+$ ions according to Eq. (4.28) is $W \approx 90$ μm. Thus, the intrinsic FWHM of the center spot on the detector at SHIPTRAP is indeed 21×0.09 mm ≈ 2 mm.

For the ultimate cooling of the ion motions a few parameters have to be optimized, starting with the cooling time. At SHIPTRAP the ion cooling in the PT and the ν_c frequency measurement in the MT are performed sequentially. In principle, the ion cooling in the
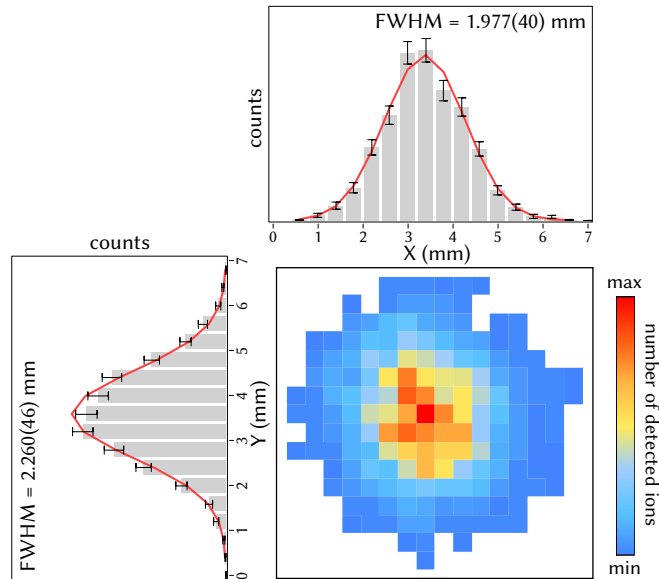
Figure 5.4: A typical projection of the cooled ^{133}Cs$^+$ ions (center spot) onto the position sensitive MCP detector. For visualization of the radial distribution the spot has a bin structure, and the color-code represents the number of ions per bin. The X- and Y-projections are shown as the histograms. The Gaussian fit is applied to each projection (red curve) and the FWHM is derived.

PT and the ν_c frequency measurement in the MT could be done in parallel, gaining in the total effective measurement time. However, due to technical limitations it could not be realized and the procedures were performed sequentially. Thus, one one hand, being only a preparatory part of the whole measurement cycle, the total cooling time should be as short as possible. On the other hand, there is a minimum required cooling time[1]. On the other hand, the PT and MT are separated only by the diaphragm, therefore the residual pressure in the MT is strongly correlated with the buffer-gas pressure in the PT. It was found out that the residual pressure in the MT sets the main limitation to the precision of the mass measurements at SHIPTRAP. Thus, the total cooling time and the buffer-gas pressure are the parameters which have to be well balanced for high-precision mass measurements. The empirically determined values are the $150 - 200$ ms of the total cooling time and $\approx 5 \cdot 10^{-5}$ mbar pressure of the helium buffer-gas.

The pulse pattern scheme for the cooling procedure is depicted in Fig. 5.5. The rf-pulses at ν_- and ν_c frequencies are applied simultaneously. It allows a smooth increasing of the magnetron radius of all the ions except the ions of interest, which are continuously cooled owing to the mass-selective π-pulse at ν_c. Note that in contrast to the conventional cooling scheme, where these two rf-pulses are applied sequentially, the new approach is more delicate and, therefore, improves the overall cooling performance.

At a fixed buffer-gas pressure and the total cooling time the parameters to be optimized are the duration and amplitude of the ν_- and ν_c rf-pulses. The idea of the optimization

---

[1]This time is defined by the fact that for the efficient cooling the collision between an ion and a buffer-gas atom occurs only once per few cyclotron revolutions. Indeed, if the kinematics of two adjacent collisions is not correlated, then the scattering angle is averaged out and the ion is gradually cooling by losing its energy.
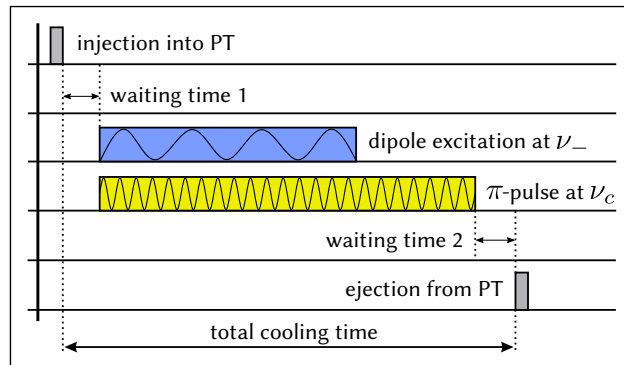
Figure 5.5: Excitation-pulse scheme for the buffer-gas cooling technique. For details see text.

is shown in Fig. 5.6. The additional degree of freedom for the fine-tuning can be added as the waiting times before and after the rf-pulses. The «waiting time 1» of $5 - 10$ ms helps to pre-cool axial motion and to confine the ions in a smaller, more homogeneous and harmonic volume. The «waiting time 2» of another $5 - 10$ ms finishes the self-cooling of a residual cyclotron motion. The cooling optimization is considered completed when the intrinsic FWHM of the spot is reached.
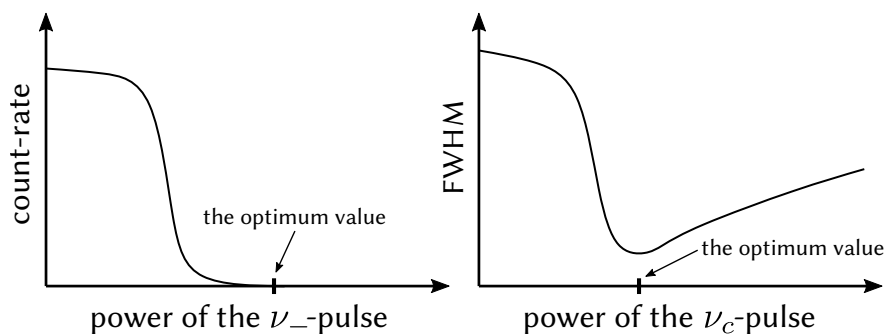
Figure 5.6: rf-pulses power optimization for the best cooling performance at a given buffer-gas pressure. Power of an rf-pulse is the product of its amplitude and duration. Left: the count-rate on the detector in dependence on the power of the ν_--pulse, while ν_c-pulse is off. Duration of the ν_--pulse is $\sim 50\%$ of the total cooling time. The optimum value is the minimal power when no ion is seen. Right: the FWHM of the spot on the detector in dependence on the power of the ν_c-pulse, whereas the optimum ν_--pulse is applied. Duration of the ν_c-pulse should be about 90% of the total cooling time.

5.2.2 Ion preparation in the measurement trap

When the ultimate cooling performance is achieved, the ions can be transported from the PT to the MT. The transfer between the traps doesn't disturb spatial ion distribution. However, due to a non-ideal capture timing and non-perfect alignment of the trap axes relative to each other and to the magnetic field lines, after capturing the ion bunch acquires a non negligible amplitude of the coherent components of the magnetron and axial motions. By fine-tuning the transportation timing and the transportation voltages between PT and MT (see Fig. 5.2) the initial axial motion can be sufficiently minimized. The amplitude of the

axial motion can be observed by measuring the time of flight from the MT to the detector within the period of the axial motion. Alternatively, the initial axial motion can be damped by the rf-pulse at ν_z frequency with a certain amplitude, duration and phase. At SHIPTRAP both approaches work well. In order to minimize initial magnetron motion, the only option is to apply the damping rf-pulse. The cabling scheme for application of the damping rf-pulses is shown in Fig. 5.7, while the idea of the ν_- and ν_z damping rf-pulses optimization is depicted in Fig. 5.8. Duration of the ν_- damping rf-pulse didn't exceed 5 ms. Ultimately, amplitudes of the coherent ν_- and ν_z components in the trap are minimized down to 0.01 mm and 0.4 mm, respectively. These preparatory steps are required for the reduction to a level well below 10^{-10} a possible shift in the cyclotron-frequency ratios due to the inharmonicity of the trap potential and the inhomogeneity of the magnetic field.
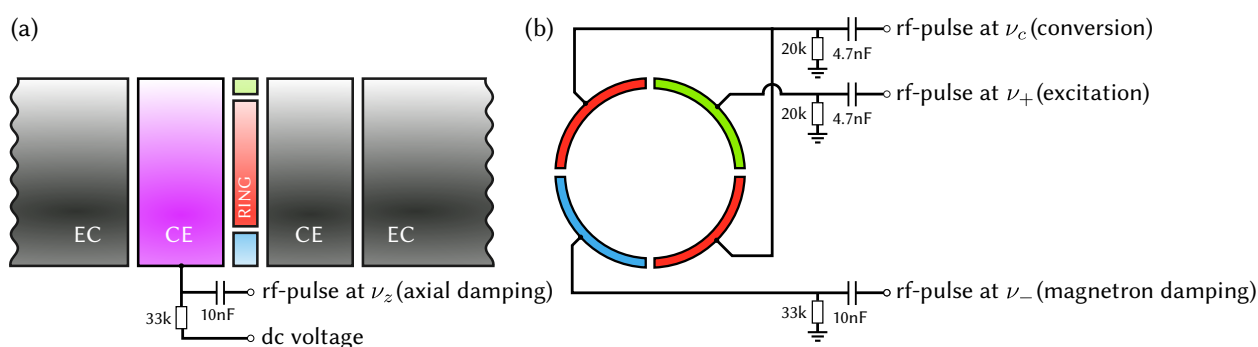
Figure 5.7: (a) Side view of the measurement trap with the axial damping line attached to the correction electrode. (b) Transverse cut of a four-fold segmented ring electrode with the minimal wiring configuration to apply the PI-ICR technique.
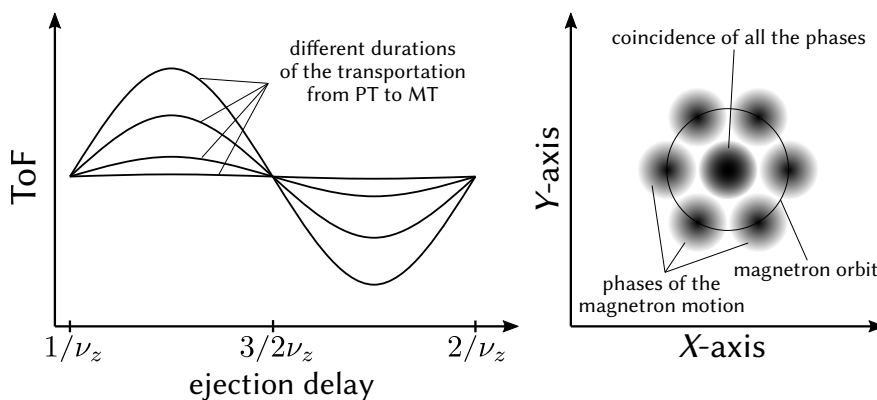

Figure 5.8: Minimization of the initial axial and magnetron motions in the MT. Left: time of flight in dependence on the transportation pulse duration. The optimum duration is when the amplitude of the oscillation is minimal. Right: phases of the magnetron motion on the PS-MCP. The damping ν_--pulse has the optimum settings when the magnetron orbit is minimized and all the phases coincide.

5.2.3 Harmonization of the trap potential

A visualization of the radial ion motions on the position-sensitive detector offers a simple method to tune the harmonicity of the trapping potential. In general, the trap frequencies are functions of the amplitudes of the motions due to a certain inhomogeneity of the magnetic field in the trap and a deviation of the trapping potential from the quadratic form. At SHIPTRAP the magnetron-frequency shift due to the magnetic field inhomogeneity for a magnetron radius of up to 2 mm is negligible, while the cyclotron-frequency shift does not exceed 2 mHz [95]. The latter one is not visible on the detector for phase-accumulation times below 10 s and thus the effect of the magnetic field inhomogeneity on the angular position of the image spot on the detector can be neglected. Thus, the radial dependence of ν_- and ν_+ frequencies is entirely due to the deviation of the electric trapping potential from the quadratic form. The most significant non-quadratic terms in the series expansion of the potential are the octupolar C_4 and the dodecapolar C_6 terms from Eq. (4.25). These non-quadratic components of the trapping potential result in a distortion of the image spots for large radial motion amplitudes, what in turn limits the precision of the PI-ICR method.

For harmonization of the trapping potential it is reasonable to use the magnetron motion, since the cyclotron motion suffers from a substantial smearing due to an ion scattering on residual-gas molecules for long phase-accumulation times. The C_4 and C_6 terms of the trapping-potential result in a relative shift of the magnetron frequency given by [91]

$$\frac{\Delta\nu_-}{\nu_-} \propto -\left(\frac{3C_4}{C_2 d^2} + \frac{45C_6}{4C_2 d^4} \cdot \hat{z}^2\right) \cdot \hat{r}_-^2 + \left(\frac{15C_6}{8C_2 d^4}\right) \cdot \hat{r}_-^4, \tag{5.1}$$

where $\hat{z}$, $\hat{r}_-$ and $\hat{r}_+$ are the amplitudes of the corresponding eigenmotions. Equation (5.1) is valid when the corresponding amplitudes of the coherent radial motions $\hat{r}_+ < 50\,\mu\text{m}$ and $\hat{r}_- < 2\,\text{mm}$. Practically, harmonization of the trapping potential, i.e. minimization of the C_4 and C_6 terms, by adjusting the applied voltages on the correction electrodes of the trap. The harmonicity can be tested by detecting images of different magnetron radii at a fixed magnetron phase. The presence of C_4 and C_6 terms manifests itself as a deviation from the straight line and the distortion of the projection at large radii. The excitation-pulse scheme can be taken from Fig. 4.8 for the final phase of the ν_- motion. The longer the phase-accumulation time, the higher the sensitivity to the trapping potential imperfections. An exemplary harmonization was done in [95] for 1 s phase-accumulation time. After the harmonization the relative frequency shift $\Delta\nu_-/\nu_-$ was measured as a function of excitation amplitude $\hat{r}_-$. The dependence was fitted by the function

$$\Delta\nu_-/\nu_- = a_0 + a_2 \cdot \hat{r}_-^2 + a_4 \cdot \hat{r}_-^4, \tag{5.2}$$

where a_0, a_4 and a_6 are the fit coefficients. The fit yielded $a_2 = 1.5(20) \cdot 10^{-6}$ mm^{-2} and $a_4 = -8.3(14) \cdot 10^{-6}$ mm^{-4}. By comparing Eq. (5.1) with Eq. (5.2) one can deduce $C_4/C_2 = -0.0019(6)$ and $C_6/C_2 = -0.20(3)$ taking into account the characteristic trap dimension $d = 14.5$ mm and the amplitude of the coherent axial motion $\hat{z} = 0.5$ mm. The numerical estimation of the systematic error due to the presence of these residual C_4 and C_6 non-quadratic terms can be found in Sec. 5.4.2.

5.2.4   Cyclotron frequency measurement using PI-ICR

Before the PI-ICR technique for ν_c determination can be applied a few other things have to be optimized. First, the radius of the modified cyclotron motion in the trap is increased to 0.5 mm (it corresponds to 11 mm radius on the detector) in order to set an initial phase. This dipolar excitation ν_+-pulse can be as short as possible provided that the necessary radius is set. Afterwards, a π-pulse on the sideband $\nu_c = \nu_+ + \nu_-$ frequency is applied for the cyclotron-to-magnetron motion conversion. The product of the amplitude and duration (or, shortly, the power) of this π-pulse has to be optimized to ensure a full conversion. The conversion is assumed to be full when the image of the resulted phase of the magnetron motion reaches its intrinsic width, as it was just after the completed cooling in the PT. In the next step the optimum phase accumulation time should be found. The FWHM of the cyclotron phase is dictated by the residual gas pressure in the MT. The ion scattering on the residual gas broadens the ion spatial distribution imposing a strong constraint onto the achievable precision of the mass measurement at SHIPTRAP [95]. Therefore, at the cyclotron radius of $\hat{r}_+ \approx 0.5$ mm an optimum phase accumulation time is about $500 - 700$ ms, such that the FWHM of the cyclotron spot is larger than the magnetron spot by at most a factor 2.

As it was already pointed out, prior to the projection onto the detector, the cyclotron motion must be converted into magnetron motion by applying a π-pulse at the cyclotron frequency ν_c. Clearly, this shifts the angular position of the image spot by a certain phase. However, since the difference of the reference and the final phases is measured, this constant offset cancels out. This is correct only in the ideal case, when the frequency of the π-pulse equals the cyclotron frequency ν_c of the ions at the moment of the conversion and the amplitude of the π-pulse remains constant. In reality, 1) the reference and final phases are measured at different times, 2) the cyclotron frequency ν_c is changing in time due to the temporal instability of the magnetic field, 3) radial frequencies fluctuate due to the temporal instability of the trapping voltage. These effects lead to different phase offsets of the reference and final phases after the conversion, and thus to an error of the cyclotron-frequency determination. In order to eliminate this error the phase-accumulation time must be a multiple of half the period of the free cyclotron motion, as it was proved in [95].

In practice, the phase accumulation time is defined as $t_{\text{long}} - t_{\text{short}} = (n_{\text{long}} - n_{\text{short}})/\nu_f$, where times $t_{\text{short}} = n_{\text{short}}/\nu_f$ and $t_{\text{long}} = n_{\text{long}}/\nu_f$ are set as the delays prior to the corresponding π-pulses as shown in Fig. 5.9. The two double-channel function generators (Agilent 33522A) are used to generate ν_+- and ν_c rf-pulses. The cabling scheme is shown in Fig. 5.7. These function generators (FG) are alternately triggered by the TTL pulse generator (NI FP-GA-PCI7811R), which is also used to generate all the other necessary trigger pulses, including injection and ejection pulses. The reason of using Agilent FGs for setting the phase accumulation time is that these devices are an order of magnitude more precise and stable in timing than the used TTL generator. Number of revolutions n_{long} and n_{short} together with the ν_f frequency are manually set to the FGs. Thus, when the measurement scheme depicted in Fig. 5.9 is applied and if $\nu_f = \nu_c$ then the magnetron and cyclotron phases on the detector should perfectly overlap. In reality $\nu_f \approx \nu_c$ and (if we don't miss any revolutions) the angle

α_c (see Fig. 4.9) between these phases is used as a correction factor:

$$\nu_c = \frac{\alpha_c + 2\pi(n_{\text{short}} + n_{\text{long}})}{2\pi(t_{\text{short}} + t_{\text{long}})}. \tag{5.3}$$

The sampling rate of the used FG (Agilent 33522A) is $S = 250$ MHz, therefore all the delays can be set in steps of 4 ns. Thus, in order to set the phase-accumulation time in multiple of half the period of the free cyclotron motion the set frequency ν_f is rounded such that

$$\frac{n}{2} \cdot \frac{S}{\nu_f} = p, \tag{5.4}$$

where n is the number of full periods and p is an integer number.

The angle α_c between magnetron and cyclotron spots should be as small as possible. There are a few reasons for this condition, which are considered in Sec. 5.4.3. Practically, the allowed drift of α_c is plus-minus a few degrees, and if α_c exceeds the acceptable range then the set ν_f frequency at the FG has to be readjusted.
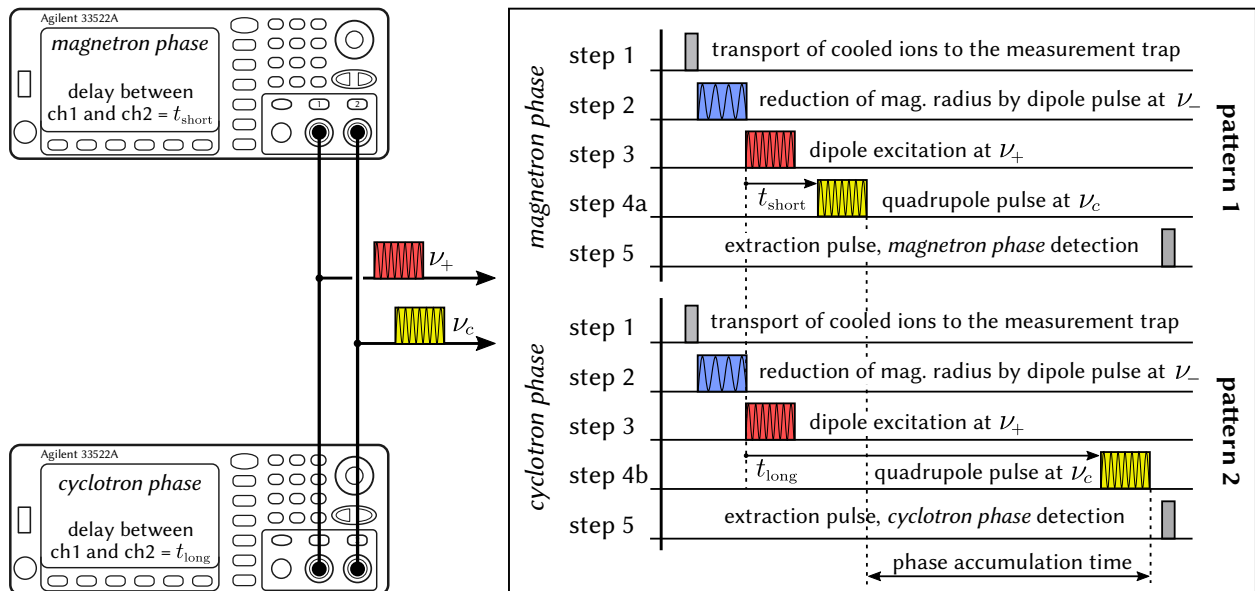
Figure 5.9: Excitation-pulse scheme for the direct measurement of ν_c. For details see text.

Despite that the initial magnetron motion was damped, to some extend it is still present in the final magnetron and cyclotron phases, and thus has to be averaged out. For that the delay of the excitation ν_+-pulse (step 3 in Fig. 5.9) is swept within the period of the magnetron motion. Furthermore, the delay of the ejection pulse is also swept within the period of the modified cyclotron motion in order to average out the residual ν_+-motion after the conversion π-pulse (step 4 in Fig. 5.9). The application of this 2D scan is highly important for the elimination of the systematic uncertainties related to the presence of the corresponding residual radial motions.

5.3 Off-line measurement campaign at SHIPTRAP

As a proof of principle of the newly implemented PI-ICR technique the nonisobaric pair of ^{132}Xe/^{131}Xe has been probed and the result was compared with the literature value which is entirely based on the FSU-trap measurements [109]. The resulting mass difference $M(^{132}\mathrm{Xe}) - M(^{131}\mathrm{Xe}) = 930\,628\,611(29)$ eV [37, 110] was in excellent agreement with the FSU's value $930\,628\,604(13)$ eV [109]. The great success in mass difference measurements of one atomic mass unit imposed strong constraints onto the performance of the PI-ICR technique, and therefore mass doublet measurements should be even more reliable.

For the β-decay energy measurements, ions of the corresponding isobaric pairs ^{123}Te/^{123}Sb, ^{163}Ho/^{163}Dy and ^{187}Re/^{187}Os were produced with the laser-ablation ion source. In general, the mass measurement procedure for each of these three cases was identical. The major difference was in the preparation of the sample for the laser-ablation ion source. Hence, the setup optimization routine was unified in the previous section and only the unique features and results of each mass doublet are given in the following dedicated sub-paragraphs.

5.3.1 Mass difference of ^{187}Re $- ^{187}$Os

The first physics case which was investigated at SHIPTRAP after the successful commissioning of the newly implemented PI-ICR technique and part of this thesis work was the β-decay of ^{187}Re. It has the lowest decay energy in the β^--decay sector, and therefore is one of the best candidates for the neutrino mass determination (see Sec. 2.2.1). Thus, a direct and precise β-decay energy determination as the mass difference between the parent ^{187}Re and daughter ^{187}Os nuclides is of high importance.

Singly charged ions of ^{187}Re and ^{187}Os were produced with the laser-ablation ion source by irradiating the corresponding metallic samples of natural rhenium (^{187}Re $-$ natural abundance 63%) and osmium (^{187}Os $-$ natural abundance 2%).

The cyclotron motion was excited to an amplitude of about 0.5 mm ($\sim$ 11 mm on the detector) and the phase-accumulation time was set to about 700 ms. The cyclotron frequencies ν_c of the ^{187}Re$^+$ and ^{187}Os$^+$ ions were measured alternately for several days. The two examples of a few hour frequency measurements are shown in Fig. 5.10. For the frequency ratio determination the linear interpolation method described in Sec. 4.3.1 was used. An exemplary plot of the frequency ratios of the 4-hour measurement period is shown in Fig. 5.11, where the reference ion was chosen either ^{187}Re or ^{187}Os. For each of the 33 4-hour periods the weighted mean ratio R_{4h} of the ratios was calculated along with the inner and outer errors (see Sec. 4.3.1) . Despite the fact that the cyclotron frequencies may slowly drift due to the drift of the magnetic field as it is shown in Fig. 5.10(b), the frequency ratio stays constant. The final cyclotron-frequency ratio R_{mean} is the weighted mean of the R_{4h} ratios (see Fig. 5.12(b)), where the maximum of the inner and outer errors of the R_{4h} ratios were taken as the weights to calculate R_{mean}. The difference between the inner and outer errors does not exceed 10%.

Figure 5.12 shows the frequency ratios of ^{187}Re$^+$ and ^{187}Os$^+$ ions. The final mean frequency ratio R_{mean}, with its statistical and systematic uncertainty is

R_{mean} = $1.00000001431(17)_{\mathrm{stat}}(9)_{\mathrm{syst}}$. Using Eq. (4.14) and Eq. (4.15) the mass difference between ^{187}Re and ^{187}Os atoms is $\mathbf{Q = 2.492(30)_{stat}(15)_{syst}\ keV}$ [37].
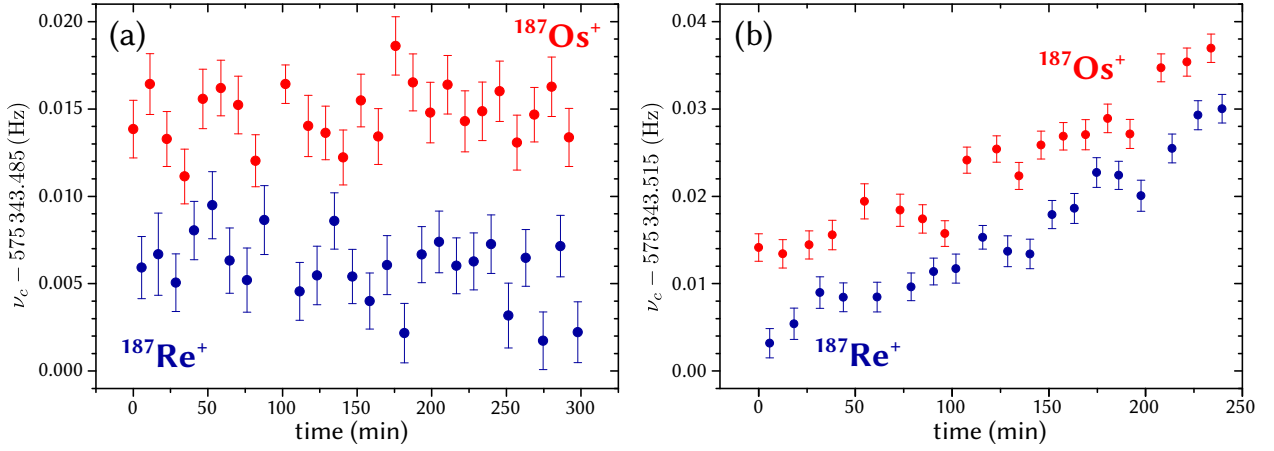

Figure 5.10: The two examples of a few hour measurements of ν_c frequency of the ^{187}Re$^+$ and ^{187}Os$^+$ ions. Plot (a) shows stable behavior of the mean frequencies, whereas plot (b) shows the clear drift of the frequencies.
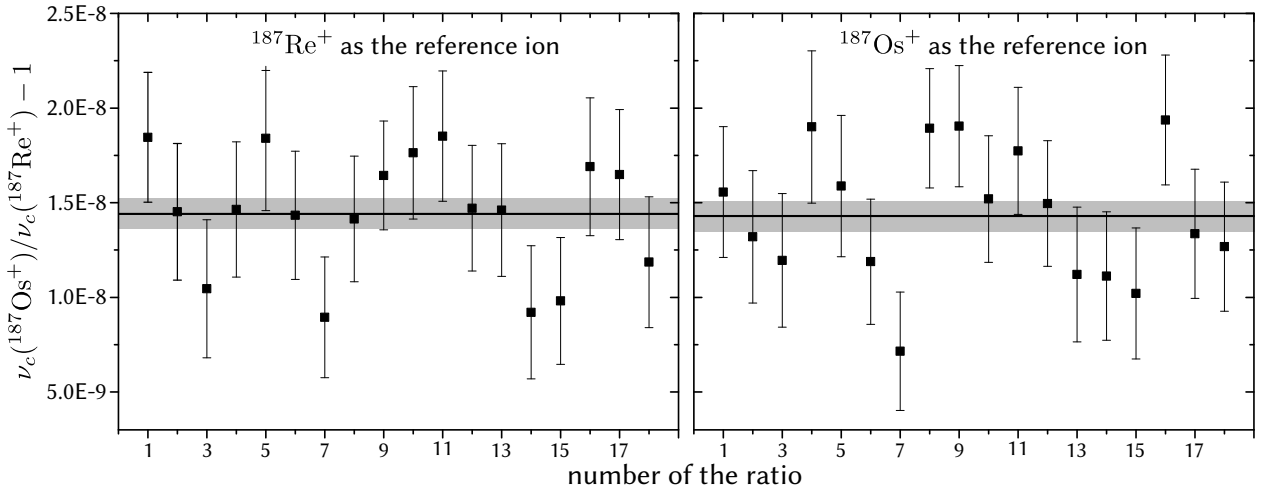

Figure 5.11: Single ratios $\nu_c(^{187}\mathrm{Os}^+)/\nu_c(^{187}\mathrm{Re}^+)$ of the data taken from Fig. 5.10(b). Either $\nu_c(^{187}\mathrm{Os}^+)$ is linearly interpolated to the measurement time of $\nu_c(^{187}\mathrm{Re}^+)$ (left plot), or the other way around (right plot) (see Sec. 4.3.1). Although Fig. 5.10(b) shows the clear drift of the cyclotron frequencies, this figure verifies that their ratio stays constant. Solid black line indicates the averaged ratio value, while the shaded area represents its 1σ standard deviation.

5.3.2 Mass difference of ^{163}Ho $-$ ^{163}Dy

The second physics case which was investigated at SHIPTRAP was ^{163}Ho. It has the lowest decay energy in electron capture domain being another good candidate for the neutrino mass determination (see Sec. 2.2.2). Therefore, the direct and precise total decay energy
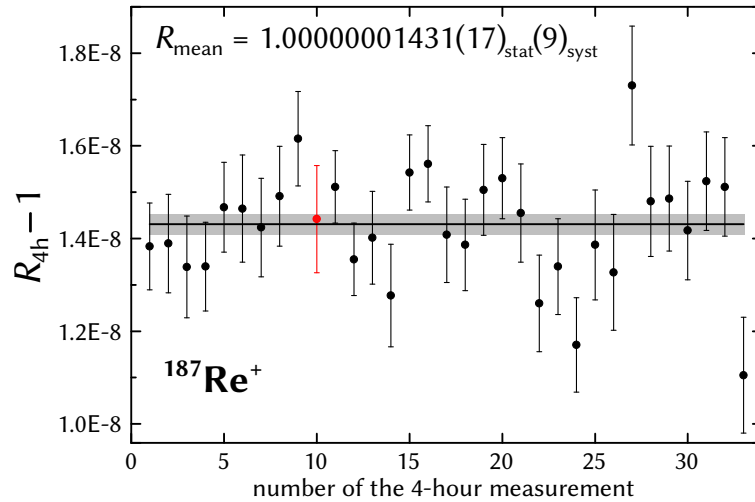
Figure 5.12: The cyclotron frequency ratios $R_{4h} = \nu_c(^{187}\mathrm{Os}^+)/\nu_c(^{187}\mathrm{Re}^+)$ determined over the 4-hour measurement intervals. The ratio marked in red is obtained from the data set in Fig. 5.10(b), showing that even though cyclotron frequencies may drift, the frequency ratio stays constant. The solid black line and the gray band is the mean value and its 1σ statistical uncertainty, respectively.

determination as the mass difference between parent $^{163}\mathrm{Ho}$ and daughter $^{163}\mathrm{Dy}$ atoms is of high importance.

Singly charged ions of $^{163}\mathrm{Ho}$ and $^{163}\mathrm{Dy}$ were produced with the laser-ablation ion source by irradiating the corresponding metallic samples. For the production of the Dy sample, a few milligrams of natural Dy in powder form were spread over a $5 \times 5\mathrm{mm}^2$ titanium substrate. The nuclide $^{163}\mathrm{Dy}$ is stable and 25% naturally abundant, however $^{163}\mathrm{Ho}$ is radioactive with a half-life of 4570(25) years and thus first had to be produced in a sufficient amount and in a high-purity form. The production of $^{163}\mathrm{Ho}$ involved neutron irradiation of an enriched $^{162}\mathrm{Er}$ sample in the high-flux reactor at the Institut Laue-Langevin and the subsequent electron capture decay of the resulting $^{163}\mathrm{Er}$ ($T_{1/2} = 75$ min) into $^{163}\mathrm{Ho}$. This was followed by a chemical separation based on ion chromatography optimized to separate neighboring lanthanides [111]. The resulting $^{163}\mathrm{Ho}$ contained less than 0.4% $^{163}\mathrm{Dy}$ — the only nuclide that cannot be resolved from $^{163}\mathrm{Ho}$ in the Penning trap and hence can lead to a systematic uncertainty in the mass difference determination between $^{163}\mathrm{Ho}$ and $^{163}\mathrm{Dy}$. Finally, the Ho sample for the laser ion source was prepared by putting a drop of $^{163}\mathrm{Ho}$ nitrate on a titanium plate and letting it dry. The final Ho sample contained about 10^{16} atoms of $^{163}\mathrm{Ho}$.

The cyclotron motion was excited to an amplitude of about 0.7 mm (~ 15 mm on the detector) and the phase-accumulation time was set to about 600 ms. The cyclotron frequencies ν_c of the $^{163}\mathrm{Dy}^+$ and $^{163}\mathrm{Ho}^+$ ions were measured alternately for many days. An exemplary 5-hour measurement period of cyclotron frequencies is shown in Fig. 5.13. The whole cyclotron frequency data set aquired during the measurement campaign was divided into 34 approximately 5-hour intervals. For each of them the ratio R_{5h} of the cyclotron frequencies ν_c of the $^{163}\mathrm{Dy}^+$ and $^{163}\mathrm{Ho}^+$ ions was obtained along with the inner and outer errors [112] by a simultaneous fit of a fifth-order polynomial to the frequency data set, as described in Sec. 4.3.1.
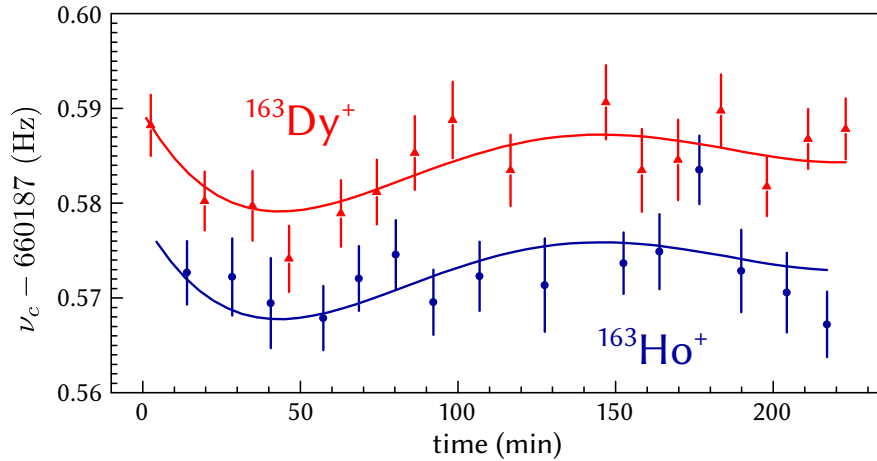
Figure 5.13: An exemplary 5-hour measurement period of the cyclotron frequencies ν_c of the ^{163}Dy$^+$ and ^{163}Ho$^+$ ions. The ratio R_{5h} of the cyclotron frequencies ν_c of the ^{163}Dy$^+$ and ^{163}Ho$^+$ ions was obtained along with the inner and outer errors by fitting to the ^{163}Ho$^+$ frequency points a fifth order polynomial $P_1(t)$ and to the ^{163}Dy$^+$ frequency points a polynomial $P_2(t) = R_{5h}P_1(t)$.
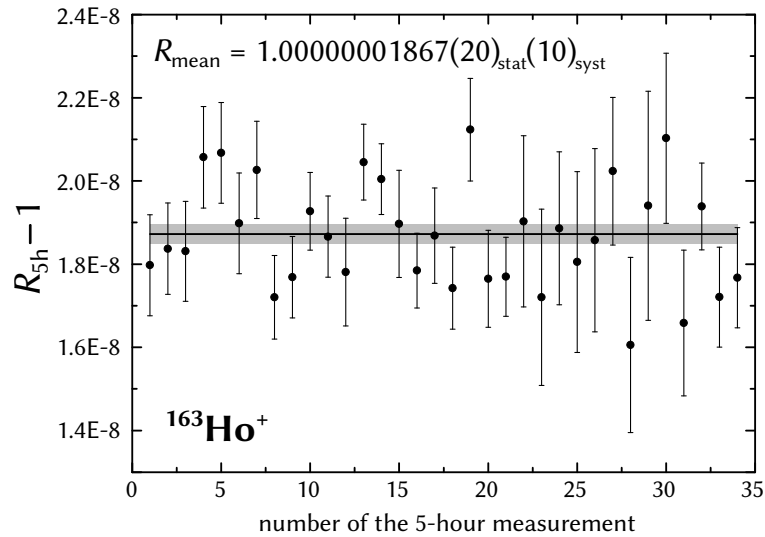

Figure 5.14: The cyclotron frequency ratios $R_{5h} = \nu_c(^{163}\text{Dy}^+)/\nu_c(^{163}\text{Ho}^+)$ determined over the 5-hour measurement intervals. The solid black line and the gray band is the mean value and its 1σ statistical uncertainty, respectively.

Figure 5.14 shows the frequency ratios of ^{163}Ho$^+$ and ^{163}Dy$^+$ ions. The final mean frequency ratio R_{mean}, with its statistical and systematic uncertainty is $R_{\text{mean}} = 1.00000001867(20)_{\text{stat}}(10)_{\text{syst}}$. Note that this value already accounts for the systematic shift due to the possible contamination of the ^{163}Ho sample by ^{163}Dy atoms. As mentioned above the contamination was estimated to be $< 0.4\%$. In case of unresolved admixture of ^{163}Dy ions during the cyclotron-frequency measurement of ^{163}Ho the experimentally measured frequency ratio R_{exp} is

$$R_{\text{exp}} = \frac{\nu_c(^{163}\text{Dy})}{(1-x)\cdot\nu_c(^{163}\text{Ho}) + x\cdot\nu_c(^{163}\text{Dy})} = \frac{R_{\text{true}}}{(1-x) + xR_{\text{true}}}, \tag{5.5}$$

where x is the fraction of ^{163}Dy atoms in the ^{163}Ho sample, and $R_{\text{true}} = \frac{\nu_c(^{163}\text{Dy})}{\nu_c(^{163}\text{Ho})}$ is the "true" cyclotron-frequency ratio in the absence of any impurities. Thereof, R_{true} can be calculated as

$$R_{\text{true}} = \frac{1 - x}{R_{\text{exp}}^{-1} - x}. \tag{5.6}$$

Thus, in case of $x = 0.4\%$ fraction of ^{163}Dy atoms in the ^{163}Ho sample, the cyclotron-frequency ratio should be shifted only by $R_{\text{true}} - R_{\text{exp}} = 7.5 \cdot 10^{-11}$, which is actually well within the total statistical error of $2 \cdot 10^{-10}$. Ultimately, using Eq. (4.14) and Eq. (4.15) the mass difference between ^{163}Ho and ^{163}Dy atoms is $\mathbf{Q = 2.833(30)_{stat}(15)_{syst}}$ **keV** [38].

5.3.3   Mass difference of ^{123}Te $- ^{123}$Sb

The third pair which was measured within the off-line campaign at SHIPTRAP and as part of this thesis is ^{123}Te $- ^{123}$Sb. Nuclide ^{123}Te has a low decay energy of about 50 keV and is involved in the astrophysical s-process. Due to the effects described in Sec. 3.2 its stellar half-life can drastically differ from the terrestrial one, what in turn may have an affect on the s-process local path. The decay energy of ^{123}Te has never been measured directly, however its accurate (rather then precise) value is necessary for the stellar half-life estimation.

For the production of the Sb-sample, a piece of natural Sb in metallic crystal form was used. Since the natural abundance of ^{123}Te is only 0.9% a few milligrams of enriched metallic powder with over 70% enrichment of ^{123}Te was compressed into a pellet with a diameter of 2 mm to assure sufficiently high ion production.
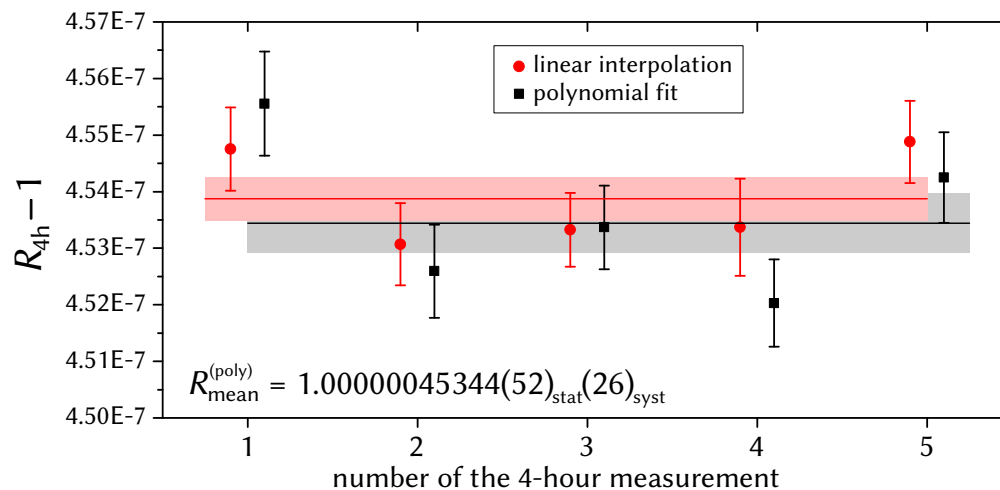

Figure 5.15: The cyclotron frequency ratios $R_{4h} = \nu_c(^{123}\text{Sb}^+)/\nu_c(^{123}\text{Te}^+)$. The solid lines and the shaded bands are the average ratios and its 1σ statistical uncertainties for either the linear interpolation method (red) or the polynomial fitting method (gray), respectively. Both methods give a consistent results.

The cyclotron motion was excited to an amplitude of about 0.7 mm ($\sim$ 15 mm on the detector) and the phase-accumulation time was set to about 450 ms. In Fig. 5.15 the cyclotron-frequency ratios R_{4h} are shown for the entire measurement period. During the measurement campaign five 4-hour measurements were performed and statistically averaged.

Each R_{4h} value was calculated by using either the polynomial fitting method (grey squares) or the linear interpolation method (red circles). It can be seen that the obtained averaged ratios well agree with each other. Moreover, the individual ratios R_{4h} all agree within error bars (1 sigma of standard deviation). The polynomial method was the method of choice for the final result since it is more robust to the drift (long-term fluctuations) of the magnetic field. Thus, the mean frequency ratio R_{mean} with its statistical and systematic uncertainty is $R_{mean} = 1.00000045344(52)_{stat}(26)_{syst}$. Using Eq. (4.14) and Eq. (4.15) the mass difference between ^{123}Te and ^{127}Sb atoms is $\mathbf{Q = 51.912(60)_{stat}(30)_{syst} \ keV}$ [113].

5.4 Data evaluation

5.4.1 Data filtering

In order to suppress the noise signals or the number of undesired events it is important to carefully filter the data the PI-ICR method produces. The dominant source of the noise signals are the dark noise of the MCP and, if the mass-selective buffer-gas cooling doesn't perform well, the contaminant ions. Moreover, the signal produced by the ions of interest sometimes may have atypical signatures, i.e. the significant deviation of the ion signal from the mean values in a time or coordinate domain. All these irrelevant signals should be filtered out.

The signals from the DLD detector are read out by the time-to-digital converter (TDC) Cronologic HPTDC8-PC. The TDC produces a string with the channel number and the time of the signal arrival. In total there are 5 signal cables coming from the DLD to the TDC: 4 delay-line signals and 1 MCP signal. An event is considered as an ion when all 4 delay-line signals come within (-25 ns, 75 ns) interval relative to the MCP signal. Another signal which is read out by the TDC is the trigger signal which is used for the ion ejection. Thus, after the data sorting every ion (event) is assigned with an array $A = (x_1, x_2, y_1, y_2, t_0)$ of the time-stamps, where t_0 is the time of flight of the ion from the trap to the MCP detector, whereas x_1, x_2, y_1 and y_2 are the signal arrival times at both ends of each parallel-pair delay-line, for each of two perpendicular independent layers, which are located just behind the MCP. The differences $(x_1 - x_2)$ and $(y_1 - y_2)$ between the signal arrival times at the adjacent ends of each delay-line are proportional to the position on the MCP in the respective dimensions. The sums $(x_1 + x_2)$ and $(y_1 + y_2)$ of these arrival times have a certain intrinsic distribution. Thus, after evaluation of these arrays one can deduce the calibration, the ToF and the X-Y ion spectra. Then, the coordinates of the image spots in X-Y spectra can be extracted after applying certain window functions to the data. The used window functions are:

1. Calibration window. It sets gates for $(x_1 + x_2)$ and $(y_1 + y_2)$ sums.
2. ToF window. The detected ions have the time-of-flight distribution. Each magnetron or cyclotron spot is assigned with its ToF spectrum.
3. X-Y window. The window is the circle around the spot center.

These window functions are listed according to their seniority, such that the calibration window affects both ToF and X-Y spectra, while the ToF window affects only the X-Y spectra. The maximum likelihood method is used to determine the mean value and dispersion ($\sigma -$

the standard deviation) of the calibration, ToF and X-Y spectra. The general data analysis of the whole measurement campaign is done using the 2σ bands around the mean values.

5.4.2 Statistical uncertainties

The whole measurement campaign consists of 5-minute measurement intervals, alternating between the two different ions species. The delay between each 5-minute measurement should be as short as possible. Typically it took us 30 seconds to load the settings for another ion species and start the next 5-minute measurement. During these 5-minute measurements only magnetron and cyclotron spots are measured, and each spot contains at least 200 ions (single events). The position of the center spot is relatively stable and can be measured only once per day, but with higher statistics (typically more than 1000 events). After the data evaluation the coordinates of the magnetron and cyclotron spots are extracted and, combining with the coordinates of the center spot, the angle α_c between these two phases is calculated, and ultimately the free cyclotron frequency ν_c is deduced. This ν_c, however, is deduced for the fixed set of window functions applied to the raw data, as described in the section above. A typical bandwidth of the window functions is 2σ, so that about 95% of the statistically distributed values are taken into account. Then, these ν_c frequencies deduced from the alternating 5-minute measurements are combined into 4- or 5-hours data sets provided that the delay between the 5-minute measurements in each data set doesn't exceed several minutes. From each frequency data set the frequency ratio $\overline{R}_i$ together with its "inner" $\delta R_i^{\text{inner}}$ and "outer" $\delta R_i^{\text{outer}}$ error is calculated using the linear interpolation and/or polynomial method. By the "inner" error we mean the standard error of the weighted mean (with variance weights)

$$\delta R_{\text{inner}} = \sqrt{\frac{1}{\sum_{k=1}^{N} w_k}}, \tag{5.7}$$

while by the "outer" error we mean the biased weighted mean variance

$$\delta R_{\text{outer}} = \sqrt{\frac{\sum_{k=1}^{N} w_k \left(\overline{R} - R_k\right)^2}{N \sum_{k=1}^{N} w_k}}, \tag{5.8}$$

with weights

$$w_k = \delta R_k^{-2}. \tag{5.9}$$

The largest error (inner or outer) is taken as the final error for each $\overline{R}_i$. Then, all the $\overline{R}_i$ are combined and averaged again, giving the final frequency ratio R_{final} together with its inner and outer error. The largest error is assigned as the final statistical uncertainty of the whole measurement campaign.

Choice of the polynomial order

If the frequency ratio of a few hour measurement is deduced using the polynomial method, then the crucial aspect is the choice of the polynomial order. In the polynomial method the

magnetic field is approximated by a polynomial function, as described in Sec. 4.3.1. However, time scales and amplitudes of magnetic-field fluctuations are not constant and, therefore, complicate the appropriate choice of the polynomial order. Owing to the temperature and pressure stabilization systems [114] the magnetic field drift shows a smooth behavior during the day. The detailed analysis of the choice of the polynomial order is done in [90], though utilizing the ToF-ICR technique for the ν_c determination. In [110] the analysis, though superficial, is done utilizing the PI-ICR technique for the ν_c determination. All in all, we can conclude that in our cases the statistical uncertainty related to the choice of the polynomial order (tested for $n = 2$ to 7) is $\Delta R/R \approx 2 \cdot 10^{-11}$.

Fluctuation of the center-image projection

Usually the coordinates of the center-image are constant such that it is sufficient to measure them with high precision only every now and then, typically once per day. Nevertheless, possible fluctuations of the center spot were tested during several days and indicated a good stability, so that the position of the center-image varied only within two standard deviations, what is statistically reasonable. To test the influence of the center-image stability on the frequency ratio we considered an extreme case, when for every single ν_c measurement we manually shift the position of the center by 0.1 mm (5σ of a typical precision of the center-image position) randomly in both dimensions. The increment of the final statistical uncertainty was only 15%. At typical experimental settings and conditions (see Sec. 5.3) these fluctuations should be way smaller. Hence, for the measurements performed in the scope of this thesis we neglected the increment of the statistical error due to the possible fluctuations of the center-image.

5.4.3 Systematic uncertainties

Systematic errors are errors that are not determined by the normally distributed parameters but are introduced by an inaccuracy inherent to the system.

Choice of the window function bandwidth

In principle, an error due to the choice of the window function bandwidth is a part of the statistical uncertainty. However, by convention we consider this error as a systematic uncertainty. The maximum likelihood method was used to determine the mean value and the dispersion (standard deviation) of the statistically distributed parameters: calibration, ToF and X-Y spectra. For the determination of the error related to the choice of the window function the bands around the mean values are swept from 1σ to 3σ. It turns out that the choice of the X-Y window bandwidth has the dominant impact on the ν_c determination, and thus on the final result. The automated multi-dimensional fit routine is integrated in the data analysis program written in LabVIEW [115]. It is empirically found that the total error related to the choice of the gate bandwidths is always about 40% of the statistical error which is calculated at the fixed window bandwidth of 2σ.

C_4 and C_6 terms

The deviation of the electric trapping potential from the quadratic form (see Eq. (4.2)) influences the magnetron and the modified cyclotron frequencies. The coefficients C_4 and C_6 are the most important non-quadratic terms (see Eq. (4.25)). The radial frequency shift due to these two terms is [91]

$$\Delta \nu_\pm = \mp \frac{C_4}{C_2} \frac{3}{4d^2} \frac{\nu_+ \nu_-}{\nu_+ - \nu_-} \left(2\hat{z}^2 - \hat{r}_\pm^2 - \hat{r}_\mp^2 \right)$$
$$\mp \frac{C_6}{C_2} \frac{15}{8d^4} \frac{\nu_+ \nu_-}{\nu_+ - \nu_-} \left(3\hat{z}^4 + \hat{r}_\pm^4 + 3\hat{r}_\mp^4 - 6\hat{r}_\pm^2 \hat{z}^2 - 12\hat{r}_\mp^2 \hat{z}^2 + 6\hat{r}_+^2 \hat{r}_-^2 \right) . \tag{5.10}$$

The absolute shift of the free cyclotron frequency is $\Delta \nu_c = \Delta \nu_+ + \Delta \nu_-$. Thus, the relative shift of the free cyclotron frequency ratio ΔR is

$$\Delta R = \frac{\nu_{c_1} + \Delta \nu_{c_1}}{\nu_{c_2} + \Delta \nu_{c_2}} - \frac{\nu_{c_1}}{\nu_{c_2}}, \tag{5.11}$$

where ν_{c_1} and ν_{c_2} are the free cyclotron frequencies of two different ion species. Note that the absolute shifts for the two ion species have the same sign.

For the numerical estimation of the radial frequency shifts for the above described mass doublet measurements the following parameters have been used: the magnetron phase has $0.5 < \hat{r}_- < 0.7$ mm and $\hat{r}_+ < 0.05$ mm, while the cyclotron phase has $0.5 < \hat{r}_+ < 0.7$ mm and $\hat{r}_- < 0.05$ mm; amplitude of the axial motion is estimated to be $\hat{z} < 0.5$ mm. The two main contributions for the inequality of $\Delta \nu_{c_1}$ and $\Delta \nu_{c_2}$ are the different ν_+ frequencies and different amplitudes of the radial motions. Using Eq. (5.10) and Eq. (5.11) the shift of the cyclotron frequency ratio for ^{123}Te, ^{163}Ho and ^{187}Re cases is $\Delta R < 10^{-14}$ and hence can be neglected at the present 0.2 ppb limit of precision at SHIPTRAP.

Distortion of the orbit-image projection

Different kinds of angular and/or linear displacement between the symmetry axes of the magnetic field, the trap electrodes, and the detector can result in a distortion of the ion-orbit projection and a shift of the center of the orbit image with respect to the symmetry axis of the detector. The orbit-image distortion causes discrepancy between the real and visible angle α_c and thus the shift of ν_c. In [95] it was shown that at SHIPTRAP the main impact on ν_c comes from the inclination of the detector symmetry axis with respect to the symmetry axis of the trap electrodes by a finite angle δ. The angle δ can be calculated from the ellipticity of the orbit image, namely from the ratio of the major to the minor radius as $r_{max}^{det}/r_{min}^{det} = 1/\cos \delta$. Measurement of the ellipticity yielded $\delta < 1°$. The shift of the radial-motion frequency caused by the distortion of the orbit image is given by [95]

$$\Delta \nu_c \approx \frac{\alpha_c - \arctan(\tan(\beta + \alpha_c)/\cos \delta) + \arctan(\tan \beta/\cos \delta)}{2\pi t}, \tag{5.12}$$

where β is the polar angle between the minor axis of the ellipse and the magnetron spot. For $\delta = 1°$, $\alpha_c = 10°$ and an arbitrary β the shift of the cyclotron frequency is $\Delta \nu_c < 5 \cdot 10^{-6}/t$,

where t is the phase-accumulation time in seconds. Thus, according to Eq. (5.11) the shift of the frequency ratio ΔR due to the distortion of the orbit-image projection is well below 10^{-11} and, hence can be neglected in all practical cases.

Interconversion of radial motions

Besides the possible distortion of the orbit-image projection the angle α_c between magnetron and cyclotron spots should be also kept as small as possible due to an error related to the interconversion of the radial motions. As mentioned in Sec. 4.4.3, prior to the projection onto the detector, the cyclotron motion has to be converted into the magnetron motion by applying a π-pulse at ν_c frequency. This leads to a shift of the angular position of the image spot by a certain phase. However, since we measure only the difference of the reference and the final phases, this constant offset α_0 cancels out (see Fig. 4.9 and Eq. (4.34)$-$(4.36)). However, this is correct only for the ideal trap and when the frequency of the π-pulse equals exactly the cyclotron frequency ν_c of the ions. In practice, the reference and final phases are measured non-simultaneously. Moreover, the temporal instability of the magnetic field and of the trapping voltage results in the fluctuation of the radial-motion frequencies. All these effects lead to different phase offsets of the reference and final phases after the conversion and thus to an error of the cyclotron-frequency determination. The detailed analysis of these effects is done in [95]. There it is concluded that the total relative cyclotron-frequency systematic shift for ^{133}Cs$^+$ ions at typical SHIPTRAP conditions is on the order of a few 10^{-10}. The impact of this cyclotron-frequency shift on the frequency ratio is well below 10^{-11} and, thus can be neglected at the present limit of precision.

Uncertainty related to the number of ions in the trap

The PI-ICR is a destructive detection technique, which requires injection of ions into the trap and, after some manipulations, ejection from it for the detection. The number of ions simultaneously present in the trap is an important parameter which has to be kept under control. Theoretically, presence of multiple ions of the same species in the ideal trap doesn't shift eigenfrequencies since the driving field acts on the center of mass of the ion cloud which coincides with the center of charge. Presence of multiple ions of different species does shift the eigenfrequencies even in the ideal trap, but the presence of contaminant ions in the measurement trap is highly unlikely owing to the mass-selective buffer-gas cooling procedure in the preparation trap[1] (see Sec. 5.2.1).

On one hand, having multiple ions per shot we would aquire the statistics in the spots faster. On the other hand, presence of multiple ions even of the same species does shift the eigenfrequencies in the real trap. Indeed, the mean trapping potential is modified due to the space-charge effect. It shifts the axial frequency and consequently radial frequencies as well. Moreover, the Coulomb force repels the ions and therefore increases the spatial ion

---

[1]Note that this is true only if the contaminant ions, e.g. other nuclides, are well resolved from the ions of interest, which is not the case for the mass doublets considered in this thesis work. In order to avoid the simultaneous presence of parent and daughter nuclides in the ion bunch special care was taken as described in Sec. 5.1

distribution. Ions in the cloud being at different radii probe the different trap imperfections and thus their individual eigenfrequencies are shifted. At SHIPTRAP it was experimentally found that if we select events with only up to 5 ion per shot it doesn't cause a shift of the frequency ratio at least on the level of $2 \cdot 10^{-10}$ [37]. It is worth noting that the total efficiency of the DLD detector is only about 25% [116] meaning that in average the total number of ions in the trap is 4 times higher than what we observe on the detector.

Summary of the systematic uncertainties

In this section several sources which could result in a systematic shift and/or systematic uncertainty in the determination of the cyclotron-frequency ratio were discussed. It is shown that even though the cyclotron frequencies of both ion species are shifted, the influence of the shift is canceled out to a large extend when calculating the frequency ratio. The effect of cancellation is even stronger when the cyclotron frequencies are nearly the same, i.e. $(R-1) < 5 \cdot 10^{-7}$ as in the cases of ^{123}Te, ^{163}Ho and ^{187}Re considered in this thesis. Thus, at typical experimental settings and conditions the impact on the cyclotron-frequency ratio due to the 1) inharmonicity of the trapping potential, 2) distortion of the orbit-image projection, 3) interconversion of the radial motions is below the total statistical uncertainty. The choice of the window functions when filtering the data has the dominant impact on the systematic uncertainty, accounting for about 40% of the statistical uncertainty.

6. The Penning-trap mass spectrometer ISOLTRAP

Since 1992, a new ISOLDE (Isotope On-Line Mass Separator) facility [117] is located at the Proton-Synchrotron Booster at CERN. The booster is aimed to the production of radioactive beams by means of impinging high-energetic protons on a thick target. The protons, produced and accelerated by the LINAC/Booster facility, are delivered as bunches every 1.2 seconds with an energy of 1.4 GeV and an intensity of up to 2μA per pulse.

The nuclides of interest are produced by bombardment of a thick, mainly uranium-carbide target via spallation, fission or fragmentation reactions. The reaction products are released from the target at a temperature of about 2000°C by thermal diffusion and effusion. Subsequently, the atoms are ionized by different techniques, including plasma, surface and laser ionization. After the ionization process, the ions are accelerated and mass separated by the general purpose magnetic separator. Then, the mass-selected ions are delivered as continuous beam at the energy up to 60 keV to the ISOLTRAP setup, composed of four ion traps. In the first trap the ions are accumulated in a linear radio-frequency quadrupole (RFQ) [118], where they are cooled by collisions with helium buffer gas, and bunched. The bunches are released from the RFQ and injected into the multi-reflection time-of-flight mass separator (MR-ToF MS) [119, 120], where the bunches of different isobars are mass separated, with a resolving power of up to $3 \cdot 10^5$ [121]. The separation is achieved using a thousend revolutions in the MR-ToF MS, corresponding to a trapping time of about 36 ms. The isobarically purified ion bunch is then transferred to the cylindrical preparation Penning trap [108] for cooling and cleaning by the mass-selective buffer-gas cooling technique [107]. The cleaned bunch of singly charged ions of interest is then injected into the hyperbolic precision Penning trap. Here, finally, a precise measurement of the cyclotron frequency of the ions is performed with either conventional or Ramsey ToF-ICR technique [96], or with the recently implemented PI-ICR technique [95]. The sketch of the ISOLTRAP experiment is shown in Fig. 6.1.

6.1 On-line campaign at ISOLTRAP

The ISOLTRAP and SHIPTRAP mass spectrometers have many similarities. Thus, only those aspects which are unique for the ISOLTRAP apparatus are considered in more details in the following, whereas the analogous things, like application of the buffer-gas cooling or the PI-ICR technique, only invoke corresponding sections of the SHIPTRAP's chapter.
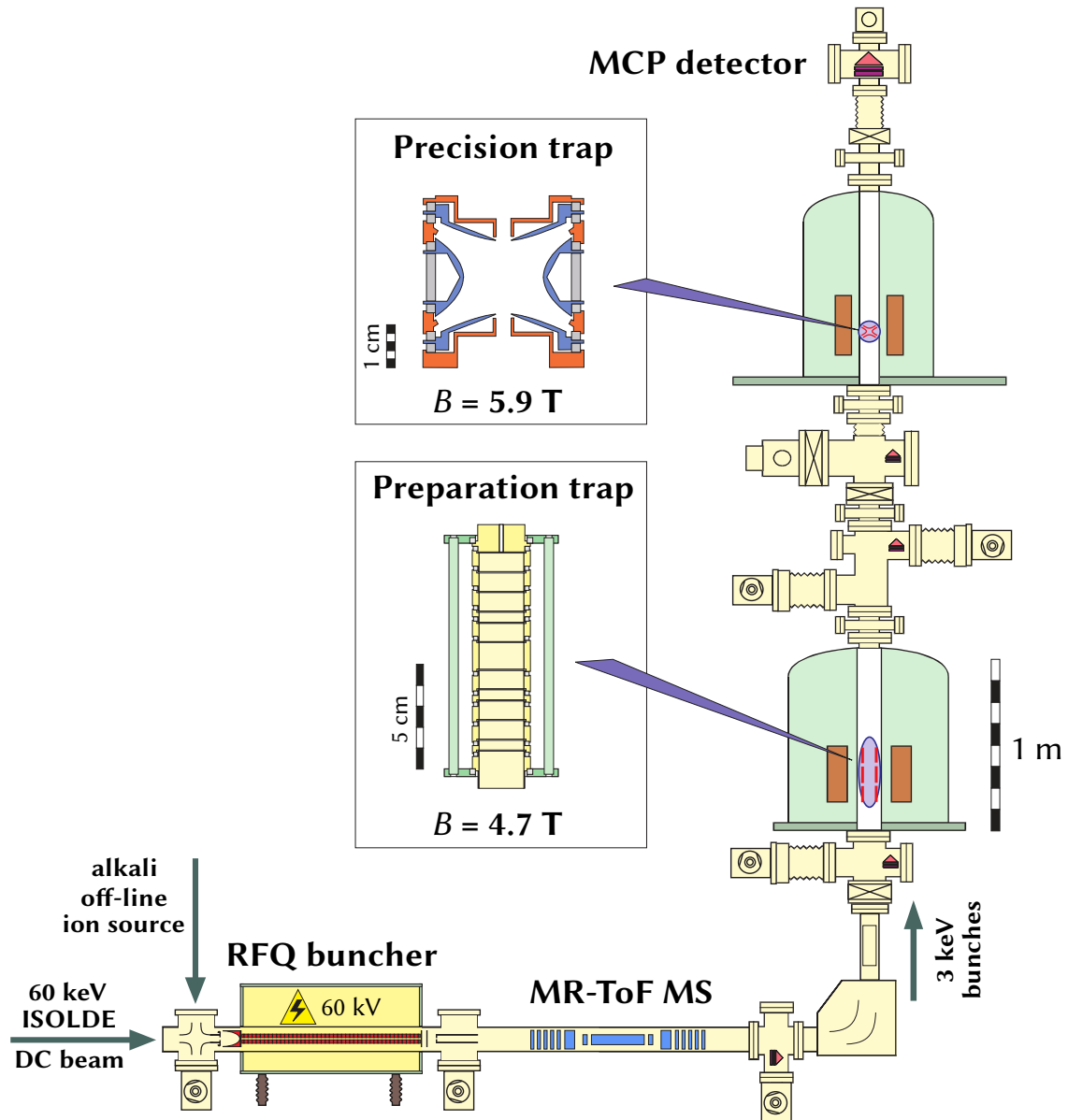
Figure 6.1: Sketch of the ISOLTRAP experiment, located at ISOLDE/CERN [116].

6.1.1 Absolute mass of ^{202}Tl

In the ground-to-ground EC domain the nuclide ^{163}Ho has the lowest so far emitted neutrino energy $Q - B_{M1} = 0.79(3)$ keV [38]. This circumstance makes ^{163}Ho the most promising nuclide for the neutrino mass determination using the kinematic approach (see Sec. 2.2.2). However, there was still one case, namely ^{202}Pb, whose emitted neutrino energy was too uncertain (see Fig. 2.3) to conclude whether ^{202}Pb can compete with ^{163}Ho. Thus, in order to eliminate the existing inaccuracy we attempted the Q-value measurement of ^{202}Pb by PT-MS at ISOLTRAP.

For the Q-value determination of ^{202}Pb, two independent campaigns on the absolute mass measurements of the mother ^{202}Pb and daughter nuclide ^{202}Tl have been performed at ISOLTRAP. Between these two independent measurement campaigns, a simultaneous

measurement of ^{202}Pb and ^{202}Tl was attempted, which would have allowed a direct Q-value determination with higher precision and accuracy. Both species were in this case produced from a UC$_x$ target, and ^{202}Pb was laser ionized. The measurement was, however, hampered by the very low surface-ionization yield of ^{202}Tl and by the contamination of the ^{202}Pb ground state by its long-lived 9^- isomeric state with $T_{1/2} = 3.54$ h. Thus, the direct Q-value determination of ^{202}Pb at ISOLTRAP was not feasible, and the Q-value could only be extracted from the absolute mass measurement of parent and daughter atoms. Absolute masses of both nuclides were determined by measuring the cyclotron-frequency ratio between the ion of interest and a corresponding singly charged reference ion. In the case of ^{202}Pb the reference mass was ^{133}Cs$^+$, whereas in the case of ^{202}Tl the additional reference ions ^{181}Ta^{16}O$^+$ and ^{203}Tl$^+$ were used. The latter helps to prevent a significant mass-dependent cyclotron frequency shift. The absolute mass of ^{202}Pb was succesfully measured in 2008 [45], while absolute mass measurement of ^{202}Tl is a subject of this thesis and is described in the following.

The ^{202}Tl ions were produced in 2015 by the ISOLDE's laser ion source RILIS [122] (for comparision the ^{202}Pb ions were produced by a hot plasma ion source [123]). The usage of the resonance ionization technique for producing of ^{202}Tl$^+$ ions substantially suppressed the beam contamination by ^{202}Pb$^+$ ions. After the ionization process, the ions are accelerated and mass separated by the general purpose magnetic separator. Next, the ions are accumulated, cooled and bunched in the buffer-gas filled RFQ with the subsequent injection into the MR-ToF MS for the isobaric purification. In this way the contaminants ^{202}Fr and ^{202}Bi were successfully separated, being 100 times less abundant than the ion of interest ^{202}Tl. The separation is achieved using 1000 revolutions in the MR-ToF, which corresponds to a trapping time of about 36 ms. The isobarically purified ion bunch is then transported to the first, cylindrical Penning trap for cooling, re-centering and additional isobaric cleaning by the mass-selective resonant buffer-gas cooling technique. The general idea of the cooling technique can be found in Sec. 4.4.1, while its application at SHIPTRAP is in Sec. 5.2.1. Note, however, that at SHIPTRAP the cooling procedure in the preparation trap is controlled by the DLD detector which allows a direct test of cooling performance of the radial motions. At the time of ^{202}Tl mass measurement at ISOLTRAP the DLD detector was not in use yet and the frequency measurements were performed by the ToF-ICR technique using a conventional MCP detector. In this case the main indicator of the cooling performance is the so-called cooling resonance, which actually doesn't assume the best cooling of the radial motions, but rather the highest purity of the ion bunch.

The cooled and purified bunch of ^{202}Tl$^+$ ions is ultimately injected into the hyperbolic precision Penning trap. Here a precise measurement of the cyclotron frequency is performed with the ToF-ICR detection technique [96] using single-pulse or two-pulse (Ramsey-type) excitation schemes (see Sec. 4.4.2) with various excitation times up to $T_{ex} = 3$ s. In total 10 ToF-ICR measurements of ^{202}Tl$^+$ were performed, the first six being sandwiched between ToF-ICR measurements of ^{203}Tl$^+$ ions, the last four between measurements of ^{181}Ta^{16}O$^+$. Both reference ions were delivered from the same on-line ion source as ^{202}Tl ions, whereas ions of ^{133}Cs were from an off-line alkali ion source. The use of two different reference ions helps to avoid a bias of the determined absolute mass value due to a potential error of the literature

value of the reference mass. Nevertheless, all 10 ToF-ICR measurements of ^{202}Tl$^+$ ions were also sandwiched between ToF-ICR spectra of ^{133}Cs$^+$ in order to monitor whether there were any significant changes in the measurement conditions; which would appear as sudden jumps in the frequency ratio with respect to ^{133}Cs$^+$. The measured cyclotron-frequency ratios of ^{202}Tl$^+$ with respect to ^{133}Cs$^+$ are plotted in Fig. 6.2.
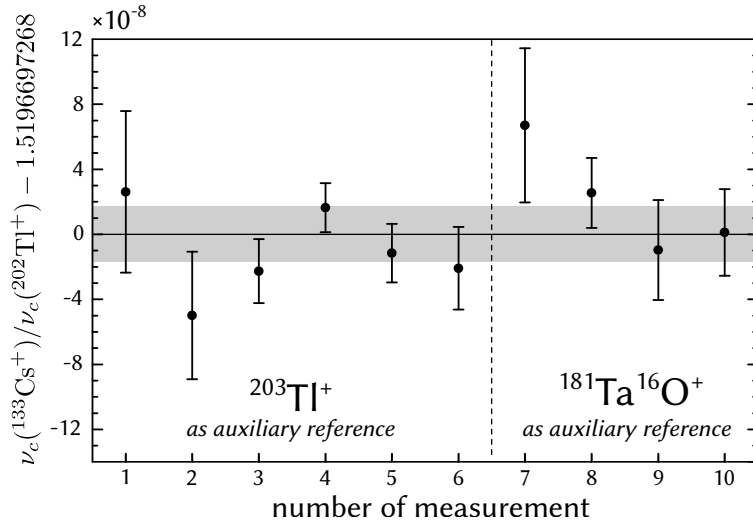

Figure 6.2: Measured cyclotron-frequency ratios of ^{202}Tl$^+$ with respect to ^{133}Cs$^+$. The error bars of the individual measurements are the pure statistical uncertainties. The dashed line in the figure separates the runs where ^{203}Tl$^+$ and ^{181}Ta^{16}O$^+$ ions were additionally sandwiched as the auxiliary reference masses. The grey shaded band represents the standard deviation of the average cyclotron-frequency ratio. For details see text.

Table 6.1 lists the final cyclotron-frequency ratios ν_{ref}/ν_c. The table separately shows both statistical and systematic uncertainties. In the case of the frequency ratios, the systematic uncertainty originates from two sources: the first is a mass-dependent error, which is due to the misalignment between the electric and magnetic symmetry axes of the Penning trap. The second error has no clear mass dependence and is due to the fact that ions of different masses probe different volumes of the Penning trap and hence their frequency ratios are affected by the trap inhomogeneities. Both relative errors were determined in [86] and were applied for the measurement of ^{202}Pb. The mass-dependent error at ISOLTRAP is $1.6 \cdot 10^{-10}$/u, while the mass-independent one is determined to be $8 \cdot 10^{-9}$. Before the ^{202}Tl measurement, however, the superconducting magnet of ISOLTRAP underwent a maintenance operation and the tras were re-aligned. The mass-dependent error was preliminary re-estimated by use of alkali ions to be $3.5 \cdot 10^{-10}$/u and this value is used for ^{202}Tl. As the general layout of the apparatus has not changed, the mass-independent error is not expected to be changed compared to the previouse one determined in [86]. The statistical uncertainty of the mass-excess values also includes the contribution of the uncertainty of the reference mass. The mass-excess of ^{202}Tl evaluated in this work was obtained using the AME algorithm, which accounts also for the consistency of the two corresponding reference masses ^{203}Tl and ^{181}Ta^{16}O, in the entire AME16 network [124]. We note that the mass-excess values of ^{202}Tl obtained by using either ^{203}Tl or ^{181}Ta^{16}O reference masses exhibits a discrepancy larger than one standard deviation.

The cause of this discrepancy could well be due to errors in the reference-mass values. This is supported by Fig. 6.2, where one can notice that the frequency ratios $\nu_c(^{202}\text{Tl})/\nu_c(^{133}\text{Cs})$ do not have any systematic shift between the two data sets, where the measurements were sandwiched with either $^{203}\text{Tl}^+$ or $^{181}\text{Ta}^{16}\text{O}^+$ ions. The final mass-excess value of ^{202}Tl deduced after applying the AME algorithm is $\text{ME}_{\text{exp}} = -25980.2(16)$ keV [51].

The Q-value of the EC in ^{202}Pb is given by the mass difference between ^{202}Pb and ^{202}Tl and amounts to $Q_{\text{EC}} = 38.8(43)$ keV [125].

Table 6.1: Cyclotron-frequency ratios of $^{202}\text{Pb}^+$ with respect to $^{133}\text{Cs}^+$, and of $^{202}\text{Tl}^+$ with respect to $^{181}\text{Ta}^{16}\text{O}^+$, $^{203}\text{Tl}^+$ and $^{133}\text{Cs}^+$. The $^{202}\text{Pb}^+$ result is taken from [45]. The mass excess deduced in this work is also shown (ME_{exp}), compared to the literature value (ME_{lit}) [126]. In the sixth column the differences between the experimental value and the AME value are listed. The statistical uncertainties are given between parentheses, while the systematic uncertainties are given between curly brackets.

Ion	Reference	Freq. ratio ν_{ref}/ν_c	ME_{exp} (keV)	ME_{lit} (keV)	Δ (keV)
$^{202}\text{Pb}^+$	$^{133}\text{Cs}^+$	1.519 670 057 7(184){164}	$-25\,941.4(35)\{20\}$	$-25\,940(4)$	1.1(57)
$^{202}\text{Tl}^+$	$^{181}\text{Ta}^{16}\text{O}^+$	1.025 536 375 2(99){84}	$-25\,984.5(26)\{15\}$	$-25\,986(14)$	1.5(14)
$^{202}\text{Tl}^+$	$^{203}\text{Tl}^+$	0.995 072 053 5(63){80}	$-25\,978.9(18)\{15\}$	$-25\,986(14)$	7.1(14)
$^{202}\text{Tl}^+$	$^{133}\text{Cs}^+$	1.519 669 741 3(72){271}	$-25\,980.6(9)\{34\}$	$-25\,986(14)$	5.4(14)

6.1.2 Absolute mass of ^{131}Cs

The nuclide ^{131}Cs presumably may have a very small emitted neutrino energy Q_ν when decaying to the $E^* = 364.5$ keV excited state of ^{131}Xe and, thus, can be a good candidate for the neutrino mass determination (see Sec. 2.2.3). The currently known literature Q-value of ^{131}Cs does not allow to clarify the situation. Thus, the precise and accurate Q-value determination of ^{131}Cs with an uncertainty less than 1 keV is demanded. The direct Q-value measurement is not feasible at ISOLTRAP due to inability of the simultaneous production of both ion species. However, the mass of the daughter ^{131}Xe nuclide is well known in the literature with the precision $\delta M = 9$ eV [1] to which, in particular, the high-precision measurement from SHIPTRAP using the PI-ICR technique made an impact [37]. Therefore, absolute mass measurements of the parent nuclide ^{131}Cs with uncertainty < 1 keV would be fairly sufficient to achieve the goal of the experiment.

The $^{131}\text{Cs}^+$ ions were produced in 2018 by the ISOLDE's hot plasma ion source [123]. The beam was then ionized via surface ionization, accelerated to 50 keV, pre-purified using a high-resolution separator and transported to the ISOLTRAP setup. As the reference mass the $^{133}\text{Cs}^+$ ions ($\delta M = 8$ eV [1]) from an off-line alkali ion source have been used. After production, the ions were accumulated in the RFQ trap and then went through the MR-ToF MS and the preparation trap in the same way as described previously in Sec. 6.1.1. Ultimately, only ions of interest arrive in the precision Penning trap for the cyclotron-frequency determination.

By 2018, ISOLTRAP has several detection techniques available, namely the conventional ToF-ICR (see Sec. 4.4.2), as well as the recently implemented PI-ICR technique (see Sec. 4.4.3). All of them were successfully used for the alternating ν_c measurement of ^{131}Cs$^+$ and ^{133}Cs$^+$ ions as shown in Fig. 6.3. The measurement campaign started with the PI-ICR method. After two hours of measurements with 100 ms phase accumulation time the rough data analysis showed the statistical uncertainty of $\delta M(^{131}\text{Cs}) \approx 260$ eV, which already meets the goals of the experiment. However, in order to cross-check the result, the conventional ToF-ICR technique with the single and two excitation-pulse scheme (Ramsey type) was applied. The cross-check did not show any shift and, thus, another 2 hours of measurements using the PI-ICR method were performed. The combined data sets of ^{131}Cs$^+$ and ^{133}Cs$^+$ cyclotron frequencies are shown in Fig. 6.3, where the simultaneous polynomial fit (see Sec. 4.3.1) is applied. As one can see, all the PT-MS detection methods are in a good agreement. Alternatively, the frequency ratio was extracted using the linear interpolation method (see Sec. 4.3.1), and the result well agrees with the polynomial method.

Besides the statistical uncertainty derived from the fit, an analysis of systematic uncertainties not being covered by the polynomial fit has to be undertaken. Investigations of the systematic uncertainty include background analysis, z-class analysis, mass-dependent frequency shift corrections, fit parameter correlations and frequency fluctuation distribution [86]. The preliminary frequency ratio without consideration of a systematic error yields $R(^{131}\text{Cs}^+/^{133}\text{Cs}^+) = 1.0152781392(13)$ with the relative statistical uncertainty of $\delta R/R = 1.3\cdot10^{-9}$. Using Eq. (4.16) the preliminary mass-excess value of ^{131}Cs is $\text{ME}_{\text{exp}}(^{131}\text{Cs}) = -88055.64(17)$ keV. The mass-excess of ^{131}Xe is $\text{ME}_{\text{lit}}(^{131}\text{Xe}) = -88413.558(9)$ keV [1] and, thus, the Q-value of ^{131}Cs given by the mass difference between ^{131}Cs and ^{131}Xe atoms amounts to $Q = 357.92(17)$ keV.
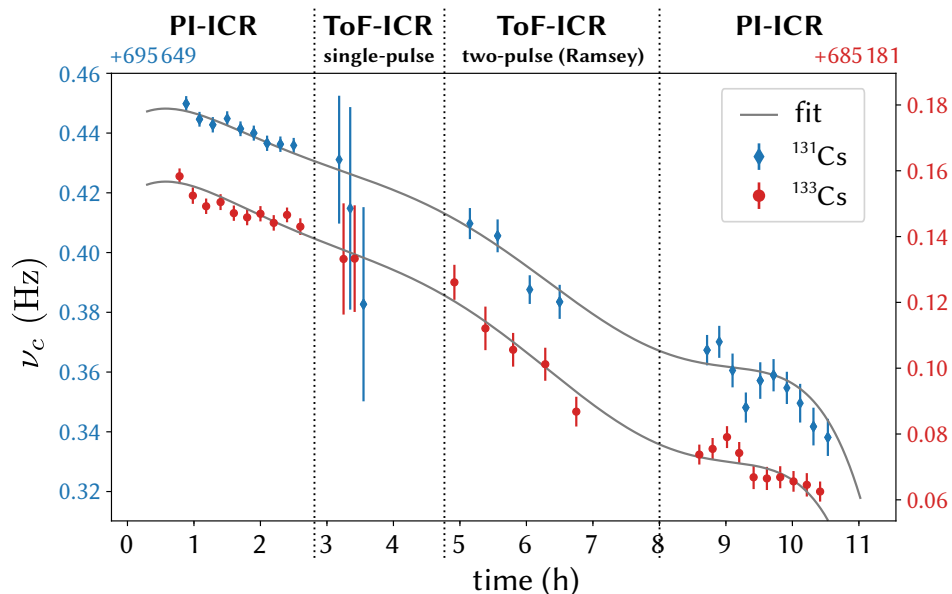

Figure 6.3: Measured cyclotron frequencies of ^{131}Cs$^+$ and ^{133}Cs$^+$ ions. Simultaneous polynomial fit to both data sets is applied to extract the frequency ratio R.

7. Results and discussions

7.1 Nuclides relevant to the neutrino mass determination

Nuclides with low-energy β-transitions are of high interest for neutrino physics as it is motivated in Chapter 2. Investigation of the β-decay kinematics is the most model independent method for the neutrino mass determination. A finite mass of the neutrino shows up as the distortion of the β-spectrum near its endpoint. According to Eq. (2.6), in any search for a kinetic neutrino mass m_{ν_e}, the emitted neutrino energy should be as small as possible, otherwise relativity hides the mass. This argument favors the search for m_{ν_e} using the low-energy β-transitions.

7.1.1 Nuclide ^{187}Re

The nuclide ^{187}Re has the lowest decay energy of $Q = 2.5$ keV in the ground state β^--decay sector. Until now, however, the Q-value of ^{187}Re had only been determined indirectly as a fit parameter from the analysis of the β^--decay spectra. Figure 7.1 shows the two distinctive data sets: one combines the values obtained with gas proportional counters [127, 128, 129] resulting in an average value of $Q = 2.647(39)$ keV, whereas the other comprises the values obtained with cryogenic microcalorimetry [130, 131, 132, 133]. If the microcalorimetric result of Cosulich-1992, which agrees with the proportional counter results, is ignored, then the average value of this group is $Q = 2.4666(16)$ keV. Evidently, there is a substantial discrepancy between the Q-values given by these two different methods. Thus, it was essential to perform an independent measurement of the Q-value of ^{187}Re with an uncertainty of at most a few tens of electron volts in order to resolve this discrepancy.

A significant deviation of the Q-value obtained by well-established PT-MS from that obtained with cryogenic microcalorimeters (CM) would hint at the existence of systematic effects inherent in microcalorimetry, which would have a severe impact on the uncertainty of a future experiment to determine the neutrino mass with this technique. Our result for the atomic mass difference of ^{187}Re and ^{187}Os of $Q = 2.492(33)$ keV [37] confirms consistency of the latest microcalorimetric measurements, as shown in Fig. 7.1. Thus, on the level of our present accuracy of 33 eV there are no unexpected systematic effects inherent in the CM technique.

As it is mentioned in Sec. 2.2.1, the authors of [35] carried out high statistics (about 10^7 decays) measurements of ^{187}Re β^--decay using $AgReO_4$ absorber and set the upper limit on
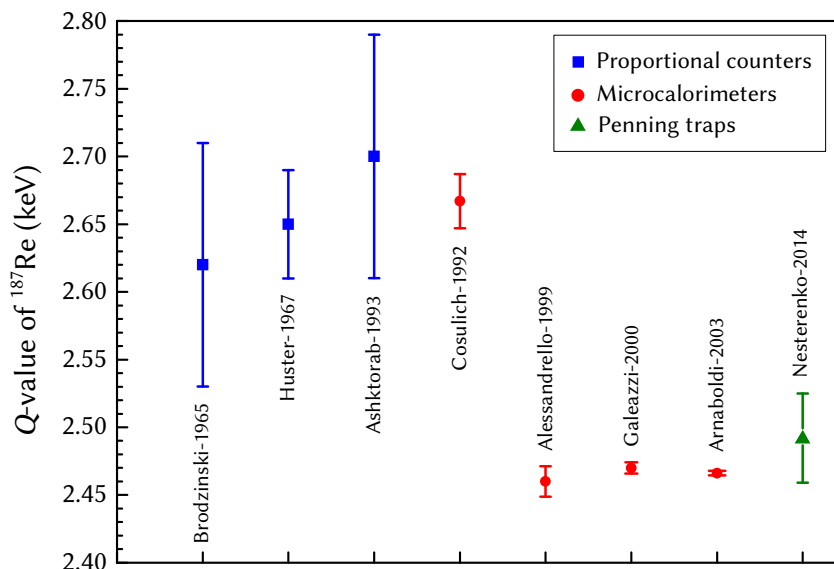
Figure 7.1: Q-values of the β^--decay of ^{187}Re, obtained in Brodzinski-1965 [127], Huster-1967 [128], Ashktorab-1993 [129], Cosulich-1992 [130], Alessandrello-1999 [131], Galeazzi-2000 [132], Arnaboldi-2003 [133] and Nesterenko-2014 [37].

the anti-neutrino mass of $m_{\nu_e} < 15$ eV (90% C.L.). The sensitivity of the experiment was limited by statistics and the detector performance, while systematic effects were expected to be small. The further investigation of ^{187}Re β^--spectra using the calorimetric approach exhibits two major difficulties: the low specific activity of about 1 Bq per mg of ^{187}Re and the relative slowness of the thermalization process in the detector. The low activity of ^{187}Re is defined by its very long half-life of $T_{1/2} \approx 43$ Gy, while the slowness of the detector thermalization is due to its high thermal (heat) capacity C_t. If a metallic rhenium crystal is used as a detector absorber for calorimetry then at the critical temperature $T_c = 1.7$ K rhenium undergoes a superconducting transition, which in turn leads to a significant rise of its thermal capacity. The high thermal capacity implies a long dead-time of the detector and a low energy resolution ΔE since $\Delta E \propto \sqrt{C_t}$. If a dielectric rhenium compound is used then it does not become superconducting, but nevertheless it doesn't completely circumvent the metallic rhenium problems since a dielectric compound has even lower specific activity and it faces an incomplete thermalization of the deposited energy. The project MARE has been coping with the demanding task of improving and scaling up those pioneer experiments of [35] and [34]. However, after several years of attempts rhenium turned out not to be fully compatible with the technical requirements of MARE and since 2015 the focus of the community was shifted from ^{187}Re to ^{163}Ho [134]. Curiously, however, that in 2010 the authors of the MARE collaboration made an overview on the expectations for a calorimetrically based experiment which utilizes ^{187}Re for the neutrino mass determination [135]. They investigated many aspects of the experiment, including pile-up effects, detector time and energy resolution, detector calibration, theoretical spectrum shape, beta environmental fine structure (BEFS) effect and others. They concluded that although systematics related to ^{187}Re β-decay theory and to the BEFS effects require further investigations, calorimetrically based experiments should not be plagued by large systematic uncertainties, and therefore

using plausible experimental configurations it is theoretically possible to achieve a sensitivity on the neutrino mass of about 0.1 eV. Nevertheless, the minimum technical requirements for a future microcalorimeter are a reasonable time resolution (less than a microsecond), an energy resolution of less than a few eV and a decent activity per detector on the order of a few Bq. Thus, only after meeting these minimum requirements the sub-eV sensitivity to the neutrino mass in high statistics β^--spectra of ^{187}Re becomes feasible. Moreover, in order to suppress systematic errors to a large extent an independent Q-value determination as the mass difference between ^{187}Re and ^{187}Os is required with the uncertainty not worse than the energy resolution ΔE of a calorimeter. The corresponding measurement with the uncertainty $\delta Q \approx 1$ eV is planned for 2019 at the Penning-trap mass spectrometer PENTATRAP [40, 136], which features are highlighted in Chapter 8.

7.1.2   Nuclide ^{202}Pb

It is clear that in the ground-to-ground β^--decay domain the nuclides ^{3}H and ^{187}Re emit antineutrinos with the lowest energies, and are therefore demanded for antineutrino mass determination experiments. In the ground-to-ground EC decay domain the nuclide ^{163}Ho has the lowest emitted neutrino energy $Q - B_{M1} = 0.79(3)$ keV [38], so far. However, by that time there was still one case, namely ^{202}Pb, whose emitted neutrino energy is presumably low (see Fig. 2.3). In order to conclude whether nuclide ^{202}Pb can compete with ^{163}Ho, we determined its Q-value by PT-MS using the ISOLTRAP facility (see Sec. 6.1.1). Unfortunately, the Q-value of ^{202}Pb was not measured directly e.g. by alternating cyclotron frequency measurements of parent and daughter nuclides, due to the very low surface-ionization yield of ^{202}Tl and the contamination of the ^{202}Pb ground state by its long-lived isomeric state. Instead, the absolute masses of ^{202}Pb [45] and ^{202}Tl [125] were determined in separated runs by measuring the cyclotron-frequency ratio between the ion of interest and a corresponding singly charged reference ion. Such an approach, however, limits the final precision and may introduce a systematic uncertainty. Nevertheless, using the conservative error we got $Q = 38.8(43)$ keV and, consequently $Q - B_{L1} = 23.5(43)$ keV. Thus, the EC in ^{202}Pb is expected to have much less sensitivity to the neutrino rest mass than the EC in ^{163}Ho, even though considering the additional enhancing effects like the shake-off of a second electron, elaborated on in [137, 138]. Moreover, the neutrino mass determination from the EC spectra of ^{202}Pb is hindered by the following issues. First, the Q-value of ^{202}Pb is relatively large for the current calorimetric experiments [139, 140, 141]. Thus, either another micro-calorimetric experiment must be built, which is suitable for this energy regime, or the current CM projects have to be adapted for this higher absorption energy value. Second, the daughter nuclide ^{202}Tl is not stable and decays with a half-life of $T_{1/2} = 12.3$ days, which would produce a significant background in the calorimetric spectrum. Hence, it is unlikely that ^{202}Pb will ever be used for the neutrino mass determination. By that, the ground-to-ground EC domain has been fully investigated in terms of the applicability of the nuclides for the neutrino mass determination. All in all, we can confidently conclude that in this domain the only nuclide which can be seriously considered is ^{163}Ho.

7.1.3 Nuclide ^{131}Cs

The last chance to find a β-transition with a small emitted neutrino energy Q_ν is to make a search in the ground-to-excited state β-decay domain. The idea is introduced in Sec. 2.2.3. So far there are 17 promising β-transitions, which are summarized in Table 2.2. In [49] we proposed to consider only 4 cases, namely ^{131}Cs, ^{134}Ce, ^{159}Dy and ^{175}Hf, and measure at ISOLTRAP their Q_{gg}-values − the atomic mass difference between ground states of the parent and daughter nuclides. In these cases a parent nuclide undergoes an allowed electron capture transition to a nuclear excited state of a daughter, and thus the partial half-life is expected to have a reasonable value. The other cases either have higher degrees of forbiddenness such that the partial half-life is expected to be significantly larger, or the nuclides can not be produced at ISOLDE, and thus it is planned to address them at a later stage.
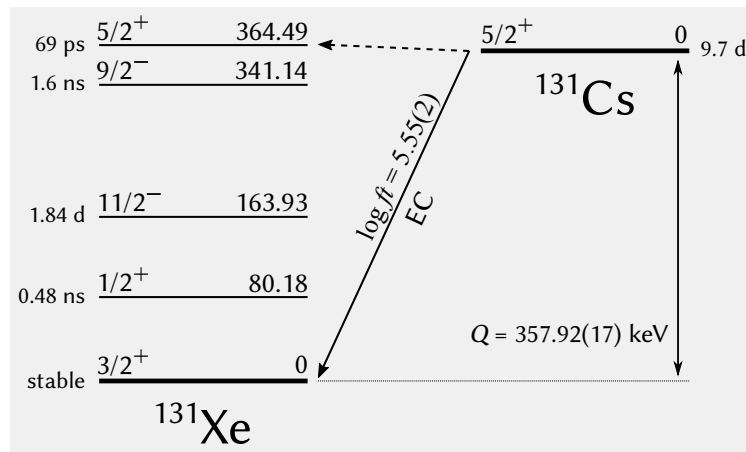
Figure 7.2: Decay scheme of ^{131}Cs. The only observed electron capture so far is indicated by the solid arrow. The capture branch we were interested in is indicated by the dashed arrow. Using our newly measured Q-value of ^{131}Cs we can confidently conclude that this transition is energetically forbidden, and thus can be excluded from the consideration in the sense of the neutrino mass determination.

The first nuclide which has been investigated within the scope of our proposal [49] is ^{131}Cs. In Fig. 7.2 the decay scheme of the ^{131}Cs ground state to the excited states of ^{131}Xe is shown. The so far known ground-to-ground decay energy $Q_{gg} = 355(5)$ keV [1] was too uncertain in order to conclude whether ^{133}Cs$(5/2^+, 0) \to {}^{133}$Xe$^*(5/2^+, 364.5$ keV$)$ transition is energetically allowed or not. The total emitted neutrino energy is $Q_{L1}^\nu = Q - B_{L1} = -16(5)$ keV and $Q_{M1}^\nu = -12(5)$ keV, surmising that the decay is energetically forbidden. In 2018 the absolute mass measurement of ^{131}Cs has been performed at ISOLTRAP using the recently implemented PI-ICR technique. Although initially in the proposal [49] it was stated that the required 1 keV precision can be achieved using the ToF-ICR Ramsey technique within six 8-hour shifts, the utilization of the PI-ICR method allowed to achieve 200 eV precision within only the two shifts (including 4 hours of the pure measurements). The measurement procedure is described in Sec. 6.1.2. The preliminary cyclotron frequency ratio is $\nu_c(^{131}\text{Cs}^+)/\nu_c(^{133}\text{Cs}^+) = 1.0152781392(13)$. It accounts only for the statistical uncertainty, however the final value will not differ much because the systematics is not expected to

have a valuable impact. The absolute atomic mass of ^{131}Cs in terms of the mass-excess is then $\mathrm{ME}_{\mathrm{exp}}(^{131}\mathrm{Cs}) = -88055.64(17)$ keV, while its ground-to-ground decay energy is $Q_{\mathrm{gg}} = 357.92(17)$ keV. Now we can affirm with certainty that the EC decay from the ground state of ^{131}Cs to the considered $E^* = 364.490(4)$ keV excited state in ^{131}Xe is energetically forbidden, i.e. $Q_{\mathrm{ge}} = -6.5(2)$ keV. Thus, the ^{131}Cs case can be excluded from the consideration as a candidate for the neutrino mass determination. Nevertheless, the succesfully implemented PI-ICR technique at ISOLTRAP appears very promising to tackle even more challenging cases such as ^{134}Ce, ^{159}Dy or ^{175}Hf [49] (see Table 2.2), where the decay energy must be determined in a sub-100-eV level.

7.1.4 Nuclides for keV-scale sterile neutrino search

Sterile neutrinos are not a part of the well-established Standard Model. As it was motivated in Sec. 2.3, the keV sterile neutrino is a good candidate as a Warm Dark Matter (WDM) particle. For the direct observation of sterile neutrinos one can produce them in a laboratory experiment and detect its presence via kinematic considerations. The β-decay process can provide necessary conditions for the search. An admixture of sterile neutrinos with the mass eigenstate m_4 should produce a kink in the β^--spectrum at the energy $Q - m_4$. Currently, there are no β^--spectroscopic indications for the existence of sterile neutrinos [24]. The electron capture process provides an alternative method for sterile neutrino search in the keV to tens of keV mass region. This idea was suggested for the first time by us in [65] and is rehashed in Sec. 2.3.1.

When considering a single ratio between two integrated rates in a given nucleus, e.g. K/L-, L/M- or M/N-ratio, the sterile neutrino with the mixing matrix element $|U_{e4}|^2$ and mass m_4 is manifested if the theoretically predicted ratio, which excludes the existence of sterile neutrinos, deviates from the experimentally measured one by more than their total combined uncertainty. Fig. 7.3 shows the achievable sensitivity to the mixing matrix element $|U_{e4}|^2$ at 90% C.L. as a function of the sterile neutrino mass m_4 for the bunch of nuclides in case of the single ratios between two integrated rates. Each curve in the figure is simulated with the assumption that the uncertainly of the calculated atomic wave functions is negligible $\delta\psi_{l,k} = 0$, the uncertainties of the measured values are $\delta Q = 1$ eV and $\delta B_l = 0.01$ eV, and the statistical uncertainty of the experimentally measured ratios $R_{\mathrm{exp}} = N_i/N_j$ is half of the uncertainty of the theoretical ratios $R_{\mathrm{th}} = \Lambda_i/\Lambda_j$, which account for δQ and δB_l. The number of events in the full EC spectrum when this criteria is satisfied, i.e. $2\delta R_{\mathrm{exp}} = \delta R_{\mathrm{th}}$, is $6 \cdot 10^9$ for ^{123}Te, 10^9 for ^{157}Tb, $6 \cdot 10^6$ for ^{163}Ho, $2 \cdot 10^{10}$ for ^{179}Ta, $3 \cdot 10^{11}$ for ^{193}Pt, $2 \cdot 10^{10}$ for ^{202}Pb, 10^{11} for ^{205}Pb and $2 \cdot 10^9$ for ^{235}Np. The highest sensitivity to $|U_{e4}|^2$ is observed when the neutrino mass is close to the corresponding $(Q - B_i)$-value, where B_i corresponds to the highest energy peak in the EC spectrum. Overall sensitivity reaches $\sim 10^{-4}$ at m_4 of a few tens of keV. However, the sensitivity drops drastically if we assume the realistic uncertainty for the calculated wave functions $\delta\psi_{l,k}/\psi_{l,k}$ of about 1%.

In order to cancel out the uncertainty of the wave function $\psi_{l,k}$ to a large extent, one can consider the "ratios between ratios" for different isotopes a and b of the same chemical element,
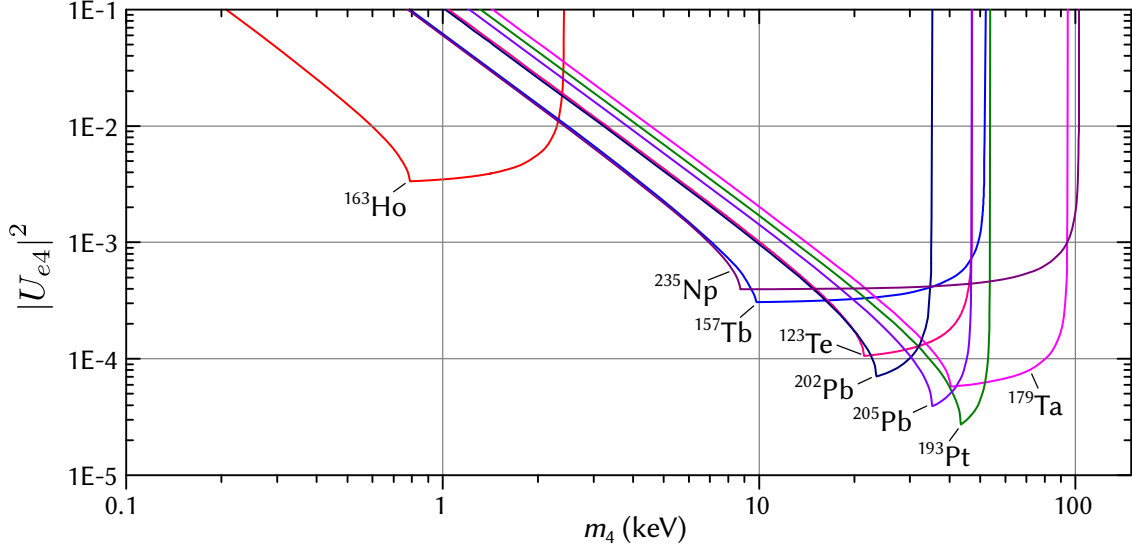
Figure 7.3: The area above the curves shows the estimated sensitivity to the mixing matrix element $|U_{e4}|^2$ at 90% C.L. as a function of the sterile neutrino mass m_4 for several EC transitions. The curves are estimated under the assumption that $\delta Q = 1$ eV, $\delta B_l = 0.01$ eV.

as described in Sec. 2.3.1. The impact of the sterile neutrino can be observed if the difference between the calculated $\Re_{ijab}$-value which doesn't account for the sterile neutrino and the experimentally measured R_{exp}-value exceeds their combined uncertainty. The sensitivity of this approach at 90% C.L. can be simulated by solving the equation [65]:

$$|\Re_{ijab} - R'| > 1.645 \cdot (\delta\Re_{ijab} + \delta R_{\text{exp}}), \tag{7.1}$$

where

$$R_{\text{exp}} = \frac{N_{ia}}{N_{ja}} \cdot \frac{N_{jb}}{N_{ja}} \tag{7.2}$$

and

$$\delta\Re_{ijab} = \sqrt{\sum_p \left(\frac{\partial\Re_{ijab}}{\partial x_p}\delta x_p\right)^2}, \quad \delta R_{\text{exp}} = \sqrt{\sum_{l,k} \left(\frac{\partial R_{\text{exp}}}{\partial N_{lk}}\delta N_{lk}\right)^2}, \quad l = \{i,j\}, \quad k = \{a,b\}. \tag{7.3}$$

Here $x_p = \{Q_a, Q_b, B_i, B_j\}$; index k means different isotopes, while index l indicates different atomic electron orbits. Using Eq. (7.1) we simulated curves for the sterile neutrino contribution and the results are given in Fig. 7.4 and Fig. 7.5. The set of input parameters used for the simulation is listed in the captions of the figures. The chosen Q_k-value and the electron binding energies B_l are not exactly the literature values, but rather rounded ones because the exact absolute values are not necessary for the current pilot studies. Having 10^{11} counts in the full spectrum the position of a peak, i.e. the centroid B_l, can be determined with an uncertainty $\delta B_l = 0.01$ eV or less.

As can be seen from Fig. 7.4, the sensitivity to a possible contribution of sterile neutrinos in the capture process reaches 0.03% for m_4 of about 10 keV − the most interesting value for WDM. The ^{202}Pb/^{205}Pb case, depicted in Fig. 7.5, has slightly higher sensitivity of

about 0.01% to $|U_{e4}|^2$, but for m_4 in the range between 20 and 45 keV, having however a feature around 34 keV due to the interference between $(Q_k - B_l)$ terms as a consequence of the similar Q_k-values.
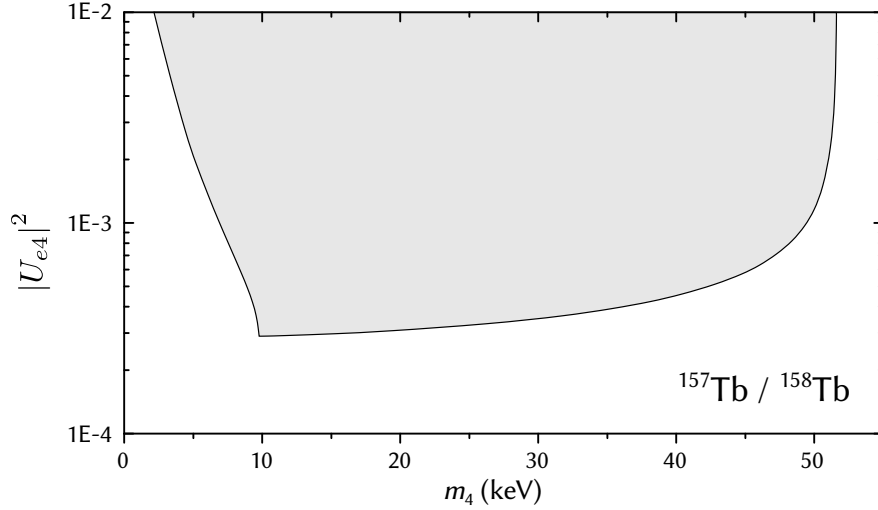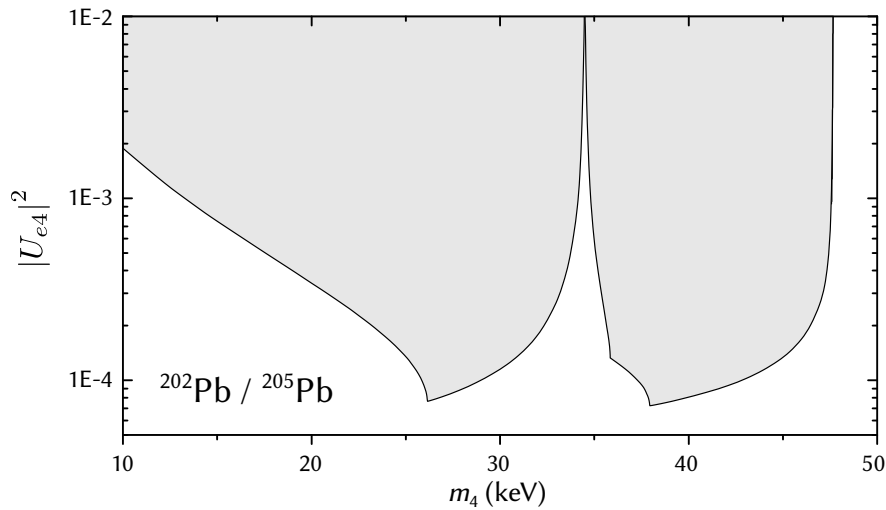

Figure 7.4: Shaded area shows the achievable sensitivity to the mixing matrix element $|U_{e4}|^2$ at 90% C.L. as a function of the sterile neutrino mass m_4 in case of the integrated K/L-ratios in ^{157}Tb and ^{158}Tb. The input parameters are: $Q_{157\text{Tb}} = 60$ keV, $Q_{158\text{Tb}} = 1219$ keV, $\delta Q_r = 1$ eV for both isotopes, $B_K = 50.24$ keV, $B_{L1} = 8.38$ keV, $\delta B_l = 0.01$ eV for both peaks, statistics in the full spectrum is 10^{11} counts. In this case the 1 eV uncertainty of the Q_r-values have the dominant impact on the total error budget.

Figure 7.5: Shaded area shows the achievable sensitivity to the mixing matrix element $|U_{e4}|^2$ at 90% C.L. as a function of the sterile neutrino mass m_4 in case of the integrated L/M-ratios in ^{202}Pb and ^{205}Pb. The input parameters are: $Q_{202\text{Pb}} = 38.8$ keV, $Q_{205\text{Pb}} = 50.6$ keV, $\delta Q_r = 1$ eV for both isotopes, $B_{L3} = 12.66$ keV, $B_{M3} = 2.96$ keV, $\delta B_l = 0.01$ eV for both peaks, statistics in the full spectrum is 10^{11} counts. In this case the 1 eV uncertainty of the Q_r-values have the dominant impact on the total error budget.

It is important to emphasize that the theoretically calculated ratios $\Re_{ijab}$, which are used for the simulation of the curves in Fig. 7.4 and 7.5, contain several approximations:

they correspond to Dirac-delta peaks, ignoring the actual shapes and widths, and thus they just refer to one single capture peak, neglecting the possible effect of the tails of nearby one-hole peaks. Moreover, the influence of two-hole peaks close to the main ones has also been neglected. Other effects, that have not been taken into account but whose influence is expected to be very small, are the multi-hole peaks, virtual intermediate states (influence of transitions through atomic shells not energetically accessible), or interference between atomic transitions resulting from the addition of amplitudes instead of intensities. The accurate experimental determination of the ratio R_{exp} entails its own difficulties. Among them are the pile-up effects in the calorimetric spectrum, the possible existence of metastable atomic states whose delayed de-excitations fail to contribute to the collected spectrum, and the variety of chemical environments resulting in a complex mixture of Q_k-values.

The sensitivity for the determination of the sterile neutrino contribution to the shape of the EC atomic de-excitation spectrum considerably depends on the uncertainty of the Q_k-values. At present, only high-precision PT-MS is capable of providing such uncertainties for a broad variety of nuclides. The uncertainty of 1 eV for the Q_k-values means relative accuracy of the absolute mass measurements of $\delta M/M \lesssim 10^{-11}$. This becomes feasible with the realization of the Penning-trap mass spectrometer PENTATRAP [40, 136].

7.2 Nuclides relevant to nuclear astrophysics

The β-decay rates λ_β and the neutron capture cross sections (n,γ) are the primary ingredients for the astrophysical s-process path determination. The s-process runs close to the valley of stability where β-decay rates are typically well known. However, for some nuclides the β-decay rates measured in terrestrial experiment may significantly deviate from the stellar ones. The main effects responsible for the dependence of λ_β on the temperature and density of the interstellar medium are described in Chapter 3. In particular, a high temperature stellar environment ionizes atoms and subsequently modifies the total β-decay energy due to the difference in the electron binding energies in the q-times ionized parent nuclide having Z protons and the q-times ionized daughter nuclide having $Z \pm 1$ protons (see Sec. 3.1). The impact of this effect is shown in Fig. 3.1 and can be as high as a few tens of keV for H-like heavy atoms. Evidently the impact of this effect is significant for low-energy β-decaying nuclei, i.e. for nuclides with $Q \lesssim 100$ keV.

If the temperature and density of the stellar matter are known, the stellar decay rates can be estimated based on the $\log ft$-values of all the energetically possible β-transitions. The $\log ft$-values of the ground-to-ground or ground-to-excited level transitions are mostly known in literature. However the $\log ft$-values of the excited-to-ground level transitions are almost inaccessible experimentally (because γ-decay by far dominates over β-transitions), but nevertheless can be estimated by comparison with known analogous transitions originated from the ground states in the isobaric chain. The correct accounting of all the energetically allowed β-transitions at stellar conditions depends on the knowledge of the overall energy balance between parent and daughter nuclei. The energy balance for all possible degree of ionization can be reconstructed based on the ground-to-ground β-decay energy Q_{neut}, energy

of excited states E^* and the electron binding energies B_i (see Eq. (3.2)). The electron binding energies B_i are theoretically calculable and the typical uncertainty doesn't exceed a few eV, except for K-shell electrons, where inconsistency of results using different models may reach a few 100 eV. The energies of the relevant low-energy excited nuclear states with $E^* < 500$ keV are usually experimentally well known with an uncertainty of $\Delta E^* \lesssim 50$ eV. The least known ingredient are the Q_{neut}-values of the neutral atoms. This circumstance motivates for direct high-precision and accurate Q_{neut}-values determination of the relevant nuclides via PT-MS.

7.2.1 Nuclide ^{123}Te

The electron capture decay of ^{123}Te has never been seen so far due to its very long half-life $T_{1/2} > 9.2 \cdot 10^{16}$ y [142]. Nevertheless, based on the data from (n, γ) reactions it is known that ^{123}Te is heavier than ^{123}Sb by $Q = 52.7(16)$ keV [124], and thus the EC decay of ^{123}Te is energetically allowed. For the first time we performed the direct Q-value measurement by means of PT-MS as described in Sec. 5.3.3. The value we've got is $Q = 51.912(67)$ keV [113], being 24 times more precise than the so far known literature value, as can be seen from Fig. 7.6, and the literature value turns out to be in a good agreement with our result.
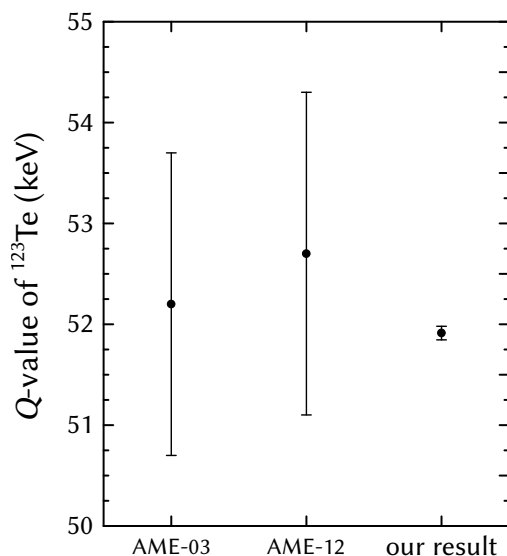
Figure 7.6: Q-value of ^{123}Te. Comparision of our result [113] with the literature values taken from AME-03 [41] and AME-12 [143].

Known information of the relevant β-transitions for a part of the isobaric chain with mass number $A = 123$ is depicted in Fig. 7.7. As can be seen, the $E^* = 159$ keV level in ^{123}Te is populated with 1% at $kT = 30$ keV, and thus, being in thermal equilibrium, can decay via electron capture to both the ground and the 160.3 keV excited state in ^{123}Sb. It predominantly decays to the latter one because of the allowed character of the transition $(3/2^+ \to 5/2^+)$. The transition to the ground state as well as the β-transition from the 160.3 keV excited state of ^{123}Sb to the ground state of ^{123}Te are of 2nd-order forbidden type and hence are much weaker. The transition probability or the comparative half-life − the $\log ft$-value − for the

allowed transition $(3/2^+, 159\,\text{keV}) \to (5/2^+, 160.3\,\text{keV})$ can not be experimentally measured[1], but can be estimated based on the similar $(3/2^+ \leftrightarrow 5/2^+)$ transitions in the $A = 123$ mass isobars (see Fig. 7.7). When accounting for the inverse transitions $(3/2^+ \to 5/2^+)$ in ^{123}I one should consider that $\log ft_{(f\to i)} = \log ft_{(i\to f)} + \log\left[(2J_f + 1)/(2J_i + 1)\right]$, where indexes i and f mean the initial and final states, respectively. Thus, the expected $\log ft$ value for the $^{123}\text{Te}^*(3/2^+, 159\,\text{keV}) \to {}^{123}\text{Sb}^*(5/2^+, 160.3\,\text{keV})$ transition is the mean value of the two known similar transitions in $A = 123$ isobaric chain, being $\log ft = (5.23 + \log {}^2\!/\!_3 + 5.24)/2 \approx 5.05$.
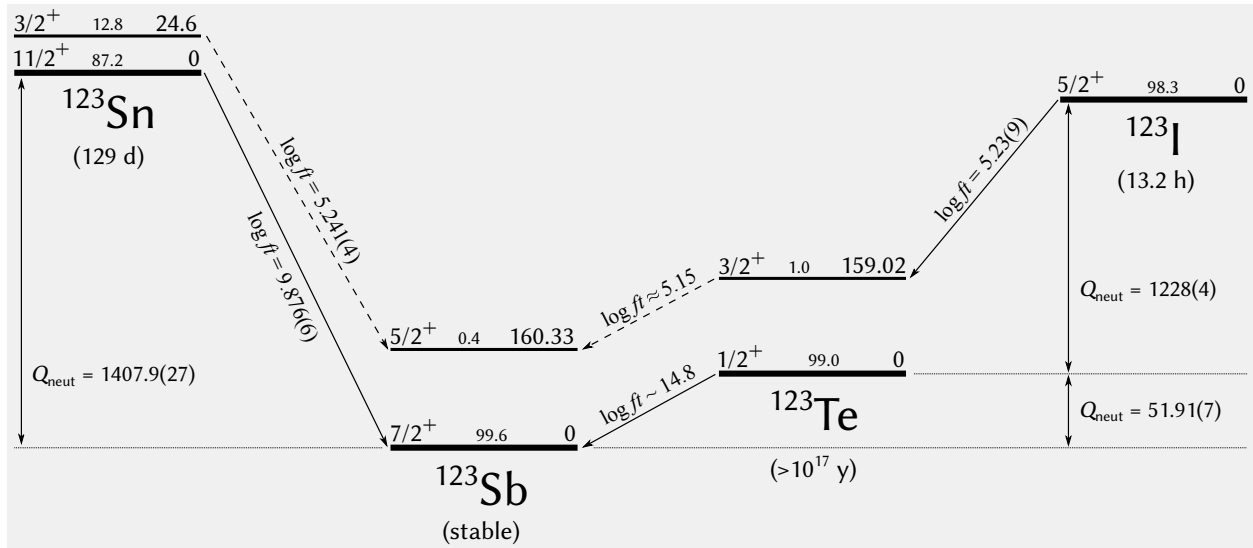
Figure 7.7: Skeleton scheme for $A = 123$ near ^{123}Te (not to scale). The Q_{neut}-values are given in keV and are for the neutral atoms. Energies of the excited nuclear states, depicted in the right side of every level, are also in keV. The value in the middle of a nuclear level is the percentage of the population at the temperature $T = 3.5 \cdot 10^9$ K ($kT = 30$ keV) of the stellar environment according to Eq. (3.5). The solid arrows are the terrestrial β-transitions, while the dashed arrows indicate the allowed β-transitions which occur only if the corresponding excited states are constantly being populated, i.e. at high environmental temperatures.

The Q_{neut}-value of ^{123}Te we have measured corresponds to the ground state of a neutral atom. Relying on our accurate result, we now can reliably calculate the energy $Q^{(q)}$ of the $^{123}\text{Te}^*(3/2^+, 159\,\text{keV}) \to {}^{123}\text{Sb}^*(5/2^+, 160.3\,\text{keV})$ transition in dependence on the ionic charge state q (see Sec. 3.1 and Eq. (3.2)). The result is shown in Fig. 7.8, where the dramatic change is seen only for H- and He-like ions as expected. The precision of the first exited states in ^{123}Te and ^{123}Sb is 20 eV and 50 eV, respectively. The most well-known values are the electron binding energies, whose precision is better than a few eV. Thus, the uncertainty of $Q^{(q)}$-values is entirely defined by the least precise Q_{neut}-value term which we have measured with the uncertainty of 67 eV. Thus, we can reliably conclude that for H- and He-like tellurium ions the K-electron capture is energetically forbidden.

In high-temperature stellar conditions different ionic states are produced having Boltzmann distributed charge states. If the matter density exceeds 10^4 g/cm^3 the capture of free

---

[1]Under terrestrial conditions this β-transition practically can not be observed since even if it is populated in a nuclear reaction it undergoes a strongly predominant γ-transition with $T_{1/2} = 196$ ps to the ground state.
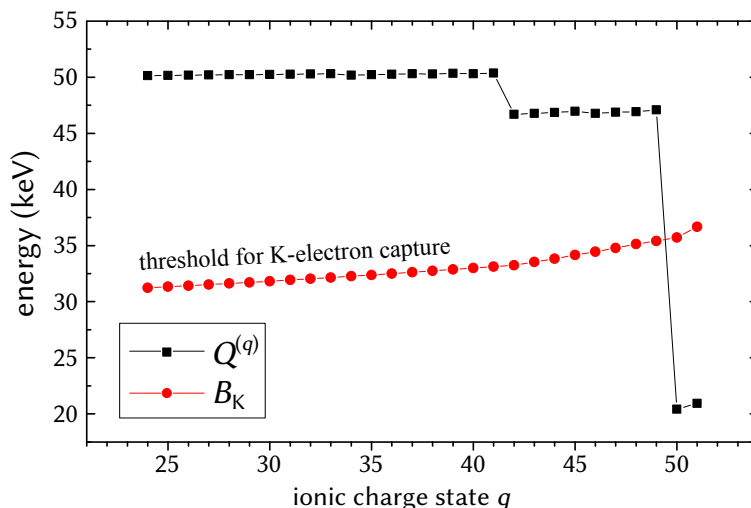
Figure 7.8: Black squares correspond to the mass difference $Q^{(q)}$ of ions $^{123}\text{Te}^*(E^* = 159$ keV$)$ and $^{123}\text{Sb}^*(E^* = 160.3$ keV$)$ according to Eq. (3.2). Red circles represent binding energy of the K-electron in dependence of the ionic charge state q. The uncertainty of all the values are well within the markers. It is seen that for the H- and He-like ^{123}Te ions the K-electron capture is energetically forbidden, i.e. $Q^{(q)} < B_K$.

environmental electrons becomes non-negligible. The formalism for calculating the decay rates of nuclides in high-temperature and high-density conditions is described in [76]. The population of various ionic states in local thermal equilibrium can be calculated using the Saha equation [144]. With these assumptions and with the nuclear input data discussed above we have re-estimated the probabilities of the orbital as well as free electron capture by the ^{123}Te nuclide being in the $E^* = 159$ keV nuclear excited state. Figure 7.9 depicts the dependence of the total effective half-life of ^{123}Te in dependence on the temperature and matter density. The exponential dependence of $T_{1/2}$ on temperature is actually due to the exponential population of the $E^* = 159$ keV nuclear excited state according to Eq. (3.5). Thus, although the population of the state is about 1% at $T = 3 \cdot 10^8$ K the total effective half-life of ^{123}Te can be as low as 10^3 years, which is more than fourteen orders of magnitude less than the expected terrestrial value.

The dramatic enhancement of the decay probability of ^{123}Te in the stellar environment could reveal the importance of this nuclide in understanding of the *s*-process scenarios. In particular, the temperature-dependent decay rates may set some meaningful constraints for the site(s) where this nuclide can be produced during the *s*-process. In massive stars the duration of the *s*-process is quite long and the strong electron capture can significantly influence the tellurium production mechanism. An attempt to quantify these expectations has been made in [145]. The authors analyzed the relative solar abundances of $^{122,123,124}\text{Te}$ in massive stars. They pointed out that the nuclide ^{123}Te can be strongly and selectively depleted in advanced evolutionary phases of massive stars as the result of the EC process on this isotope. And hence, if the contribution to the solar abundances of the *s*-only tellurium isotopes from the *s*-process in massive stars is significant, then it certainly leads to an inherent contradiction to the observational data. Additionally, a "freeze-out" of the *s*-process at high temperatures could also cause a relative deficit of ^{123}Te if its total neutron-capture
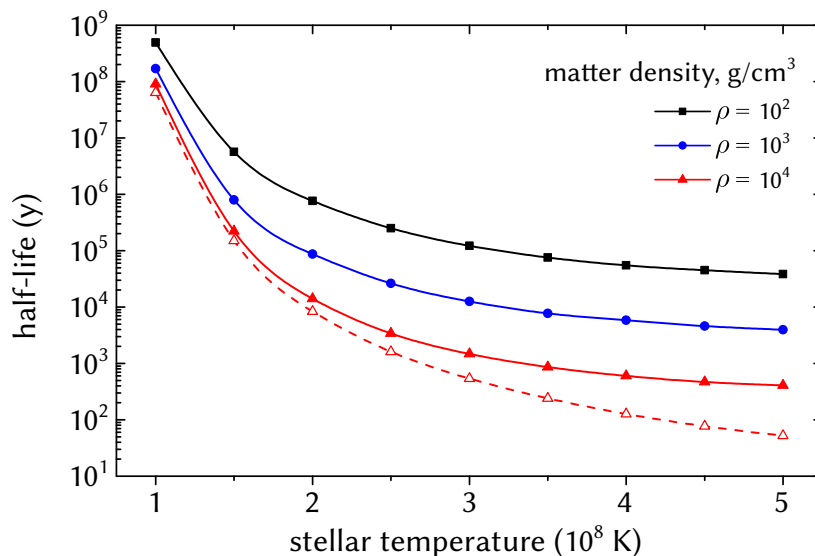
Figure 7.9: Estimated half-life of ^{123}Te in dependence on temperature and matter density using the formalism in [76]. The dashed curve represents the half-life including the capture of free electrons for $\rho = 10^4$ g/cm^3.

cross-section is considerably enhanced because of the thermally populated excited states. Nevertheless, despite the fact that the Q-value of ^{123}Te now is well known owing to our measurement, it is clear that much remains to be worked out before these claims can be verified. For example the uncertainty of the relevant $\log ft$-values should be reduced by a direct calculation of the nuclear matrix elements using new advanced theoretical models. On the astrophysical site, more detailed stellar evolution models of the variety of stars are to be tested.

7.2.2 Nuclides ^{163}Ho and ^{187}Re

In terrestrial conditions the neutral atoms of ^{187}Re are very long lived with $T_{1/2} = 43.3(7) \cdot 10^9$ y [146], which is comparable with the age of the Universe of $13.799(21) \cdot 10^9$ y [147]. Moreover, ^{187}Re is a pure r-process nuclide, whereas its daughter ^{187}Os is (almost) a pure s-process nuclide. All this makes the ^{187}Re/^{187}Os couple a good nucleo-cosmochronometer, which can among the others contribute, for example, to better understanding of astrophysical sites of the s- and r-processes, and to the dating of astrophysical objects [148, 149]. However, when considering this couple as a cosmochronometer many difficulties may arise. One of them concerns the real s-process contribution to ^{187}Os, whose evaluation requires neutron capture cross sections of ^{186,187}Os in s-process conditions. Furthermore, the uncertainties may arise from the existence of s-process branchings in the W-Os region (see Fig. 7.10). Another problem concerns the β-transition rates of ^{187}Re and ^{187}Os in stars. Due to the reasons discussed in Chapter 3 the β-decay rate of ^{187}Re may be substantially greater in certain astrophysical environments than in the laboratory, while the stable nuclide ^{187}Os may become radioactive (see Fig. 7.11). The latter effects bring an additional difficulty into the ^{187}Re-^{187}Os chronology.

The precisely and accurately known Q-value of ^{187}Re conduces to the correct assignment of the energetically allowed β-transitions (including bound-state β^--decay [150]) between
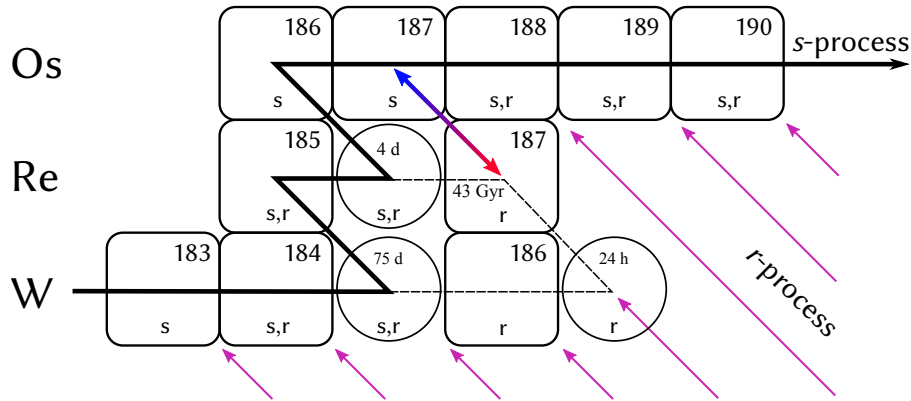
Figure 7.10: Sequence of the main *s*-process path (thick solid black line) along stable or long-lived nuclei (squares) with the branching points at radioactive nuclides (circles). The thick red-blue arrow symbolizes either the possible β^--decay of ^{187}Re, or the inverse process, namely the EC decay of ^{187}Os into ^{187}Re. The small "s" and "r" stand for the (nearly) *s*- and *r*-only nuclei, whereas "s,r" means the mixture of both the processes. The dashed black line shows the minor branching of the main *s*-process path.

^{187}Re and ^{187}Os being in different ionic charge states. Then, when combining this information with $\log ft$-values of the relevant transitions and calculating the total decay rates of ^{187}Re and ^{187}Os at stellar conditions, it results in more reliable chronological information or imposes more severe constraints on the models for the chemical evolution of the Galaxy.

Another case which undergoes dramatic changes in the high-temperature stellar medium is the ^{163}Ho-^{163}Dy couple. Schematics of the decay is shown in Fig. 7.12 where a neutral ^{163}Ho decays via EC with $T_{1/2} = 4570(50)$ y [39] to a stable ^{163}Dy atom. However, when highly ionized, ^{163}Ho becomes β-stable, whereas fully stripped ^{163}Dy gets unstable and decays mostly via the bound-state β^--decay to ^{163}Ho with $T_{1/2} = 47(5)$ y [150]. Similar to the ^{187}Re-^{187}Os case, the ^{163}Ho-^{163}Dy couple forms the branching point on the way of the *s*-process, and hence in the sense of the nuclear astrophysics the precise and accurate Q-value determination of ^{163}Ho is being demanded.
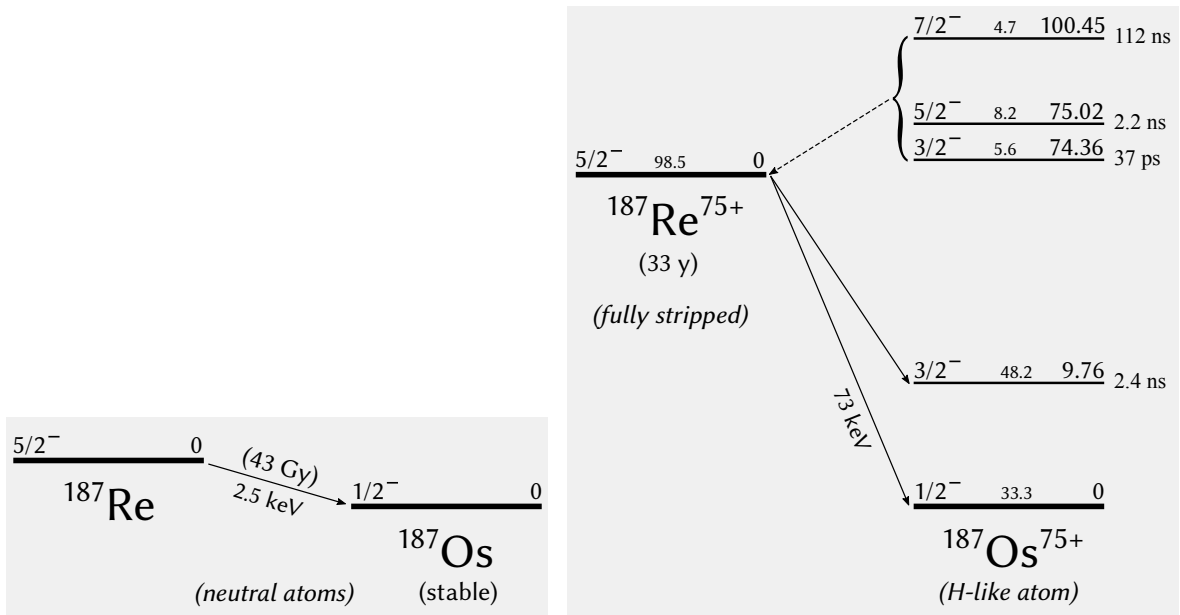
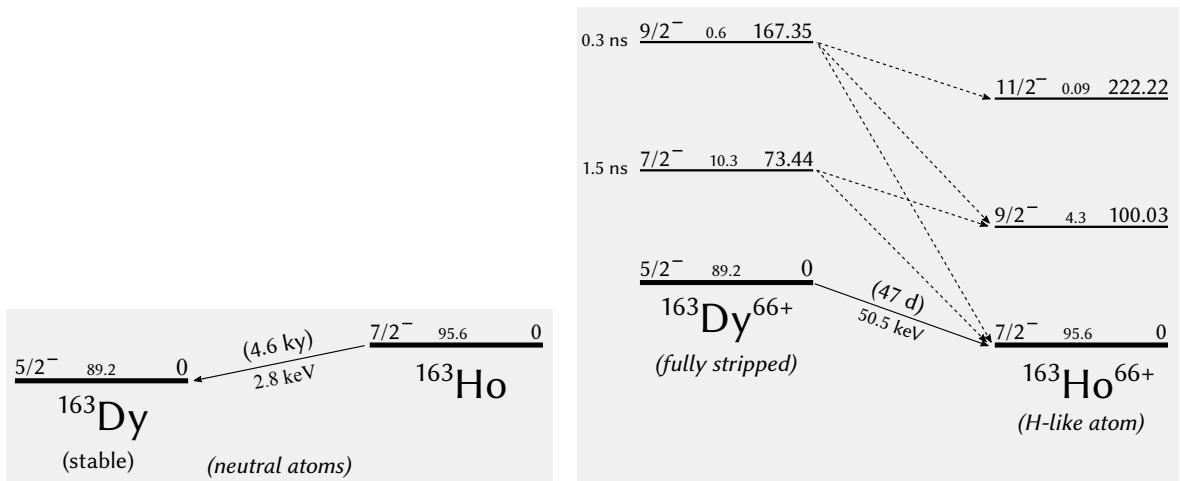**Figure 7.11:** On the left side is the decay scheme of neutral ^{187}Re, whereas on the right side is a part of the decay scheme for the bare nucleus, i.e for ^{187}Re^{75+}. It is seen that the bare ^{187}Re has a significantly higher decay energy and the half-life of only $T_{1/2} = 33(2)$ y via bound-state β^--decay [78]. At the stellar temperature $kT = 30$ keV the low-lying nuclear excited levels of ^{187}Os are populated with the probability (in percent) shown in the middle of the levels. The possible inverse β-transitions (electron capture) from the relevant levels at stellar conditions are indicated by the dashed arrow.

Figure 7.12: On the left side is the decay scheme of neutral ^{163}Ho, whereas on the right side is a part of the decay scheme for the H-like ^{163}Ho, i.e for ^{163}Ho^{66+}. H-like ^{163}Ho is stable, but the fully stripped ^{163}Dy decays with $T_{1/2} = 47(5)$ y via bound-state β^--decay [150]. At the stellar temperature $kT = 30$ keV, the low-lying nuclear excited levels of ^{163}Dy are populated with the probability (in percent) shown in the middle of the levels, and thus the total effective half-life of ^{163}Dy at stellar conditions should be even shorter. The most probable β-transitions in a stellar environment are indicated by the dashed arrows.

8. Conclusion and Outlook

This thesis is devoted to an atomic mass-difference determination of the cases relevant to neutrino physics and nuclear astrophysics. The atomic mass-difference determination is based on cyclotron-frequency ratio measurements performed by means of Penning-trap mass spectrometry (PT-MS). In the following, a brief summary on the research work is done and further steps and improvements are outlooked.

Nuclear physics opens a unique validation tool for astrophysical models by linking observables to the conditions in the deep stellar interiors. This is done by exploiting the strong dependence of nuclear processes on temperature, density, and the composition of stellar media, but requires accurate nuclear spectroscopic data. One of the important spectroscopic parameters is the total decay energy of a nuclide. This parameter is especially crucial for low-energy β-decaying nuclides which participate in the s-process of stellar nucleosynthesis. If the total decay energy is accurately known for a neutral atom, then the energy balance and hence the complete decay scheme can be reliably reconstructed for highly charged ions in hot stellar conditions, which can not be reproduced in the laboratory. With the SHIPTRAP mass spectrometer at GSI we directly determined the decay energy of the pure s-process nuclide ^{123}Te, reaching the value of $Q = 51.912(67)$ keV [113]. Using our accurate and precise value the authors of [145] analyzed the relative solar abundances of ^{122,123,124}Te in massive stars and pointed out that the nuclide ^{123}Te can be strongly and selectively depleted in advanced evolutionary phases of massive stars as the result of the electron capture process on this isotope.

Another topic which was considered in the framework of this thesis is neutrino physics. The absolute value of the neutrino rest mass is one of the most intriguing questions in modern particle physics. The most model independent approach for its determination is based on kinematics without further assumptions. Thus, investigation of the kinematics of the processes where neutrino takes a part, namely weak decays, is the most straightforward method for the neutrino mass determination. More specifically it implies investigation of the endpoint region of a β^- or electron capture spectrum, where an impact of the effective electron neutrino mass m_{ν_e} can be observed. In any search for a kinetic neutrino mass, the neutrino energy should be as small as possible, otherwise the mass is hidden by relativistic effects. This argument favours the measurement of the electron neutrino mass m_{ν_e} in low-energy nuclear β-transformations.

Within the present thesis work, a series of measurements dedicated to a search for a low-energy β-transitions was performed with the ISOLTRAP mass spectrometers at CERN. The absolute mass of the daughter ^{202}Ta nuclide was measured and the decay energy (Q-value) of parent the ^{202}Pb nuclide is deduced. It turned out that the so far considered enhancement effect at the energy $Q \approx B_i$, which could increase sensitivity to the neutrino rest mass, is

too far away from the resonance case, namely $Q - B_{L1} = 23.5(43)$ keV [125]. Thus, the electron capture in ^{202}Pb is expected to have much less sensitivity to m_{ν_e} than, for example, the ^{163}Ho case with only $Q - B_{M1} = 0.79(3)$ keV [38].

During another on-line measurement campaign at ISOLTRAP we measured the absolute mass of the parent ^{131}Cs nuclide and the achieved precision allowed to conclude that the possibly very low-energy β-transition ^{131}Cs$(5/2^+, 0) \rightarrow$ ^{131}Xe$^*(5/2^+, 364.5$ keV$)$ is not energetically allowed: $Q_{\text{ge}} = -6.5(2)$ keV. Although the final data analysis is still ongoing and the shown Q_{ge}-value is preliminary, a significant deviation from that value is not expected. Thus the ^{131}Cs case can be confidently excluded from the consideration as a candidate for the neutrino mass determination.

While β-spectra acquisition with high statistics and high energy resolution for the neutrino mass determination is the matter of Cryogenic Microcalorimetry (CM), the PT-MS can independently provide the most crucial input parameter for the fit of the spectra − the endpoint energy (Q-value), and thereby sub-eV sensitivity to m_{ν_e} can be achieved. The endpoint energy can be deduced from the β-spectrum itself by making the Fermi–Kurie plot, provided that the lineshape is accurately known. Several groups independently acquired the β^--spectra of ^{187}Re and extracted the Q-value. The achieved results, however, are by far not consistent. In order to solve the puzzle, we performed a direct Q-value measurements of ^{187}Re as the mass difference between parent and daughter nuclides at the mass spectrometers SHIPTRAP. Our result $Q = 2.492(33)$ keV [37] confirms consistency of the latest CM measurements, securing that on the level of our present accuracy of 33 eV there are no unexpected systematic effects inherent in the CM technique. However, in order to really reach the sub-eV sensitivity to m_{ν_e} the CM technique has to be further improved requiring a β-spectrum of ^{187}Re with even higher statistics and energy resolution, whereas its Q-value should be measured with eV (or even sub-eV) precision. The latter is the matter of the novel Penning-trap mass spectrometer PENTATRAP [40, 90, 136].

The unique feature of the mass spectrometer PENTATRAP is the trap-tower consisting of 5 Penning traps (each is only 24 mm in length). It allows to perform simultaneous cyclotron-frequency measurements in two adjacent traps, what in turn should cancel out temporal fluctuations of the magnetic field to a large extend. Furthermore, PENTATRAP utilizes a non-destructive image-current detection technique (FT-ICR) in 4.2K cryogenic environment. The low cryogenic temperature ensures good vacuum conditions in the trapping region and enables to cool ion eigenmotions down to a few μm level, where spatial inhomogeneity of the magnetic field $\delta B/B$ is only a few ppb. The good vacuum conditions and the ultra sensitive FT-ICR detection method allow the cyclotron-frequency detection of a single highly-charged ion. The custom-made ultra stable voltage source StaRep [151], which provides the potentials for the trap electrodes, has a temporal stability of about $\delta V/V = 2 \cdot 10^{-8}$ per 10 minutes to ensure the ultimate stability of the axial frequency of an ion.

Recently PENTATRAP has been successfully commissioned [40]. The different combinations of mass-ratios of stable xenon isotopes were measured with the statistical uncertainty of $\delta R/R \approx 10^{-11}$. Currently this statistical uncertainty can be reached after a couple of days of the pure measurement time utilizing in total four traps, two of which were used only

for storage, and two for the detection. The data analysis is still ongoing, however the systematic uncertainty is expected to be below the 10^{-11} level since the measured couples are a good charge-to-mass ratio doublets due to their equally high charge states of $17+$, e.g. $^{132}\text{Xe}^{17+}/\,^{131}\text{Xe}^{17+}$. The measured xenon mass-ratios are in a perfect agreement with the mass-ratios measured with the FSU-trap in 2013 [109], which were so far the most precisely measured mass-ratios of heavy nuclei, being however a few times less precise than our new results. The next physics cases for PENTATRAP are planned to be the electron capture in ^{163}Ho and β^--decay of ^{187}Re, for which $\delta Q \lesssim 2$ eV is aimed for.

In general the successful commissioning of PENTATRAP with xenon isotopes opens great frontiers for exploring fundamental properties of nature. In the 10^{-11} relative uncertainty regime of PENTATRAP the near future mass measurement of dedicated nuclides will allow, among others, to contribute to the tests of special relativity [152], bound-state QED [153], determination of fundamental constants [17] and neutrino-physics research [139, 154]. In a far future PENTATRAP may contribute to the keV sterile neutrino search in electron capture, as it was introduced by us in [65] and replicated in the framework of this thesis.

Bibliography

[1] M. Wang et al. "The AME2016 atomic mass evaluation (II). Tables, graphs and references". In: Chinese Physics C 41 (2017), 030003.

[2] C. L. Cowan et al. "Detection of the Free Neutrino: a Confirmation". In: Science 124 (1956), 103.

[3] Q.R. Ahmad et al. "Direct evidence for neutrino flavor transformation from neutral-current interactions in the Sudbury neutrino observatory". In: Phys. Rev. Lett. 89 (2002), 011301.

[4] Y. Fukuda et al. "Evidence for oscillation of atmospheric neutrinos". In: Phys. Rev. Lett. 81 (1998), 1562.

[5] G. Dattoli and K.V. Zhukovsky. "Neutrino mixing and the exponential form of the Pontecorvo–Maki–Nakagawa–Sakata matrix". In: The European Physical Journal C 55 (2008), 547.

[6] R.N. Mohapatra. "Origin of neutrino masses and mixings". In: Nuclear Physics B - Proceedings Supplements 91 (2001), 313.

[7] S.T. Petcov. "The Nature of Massive Neutrinos". In: Advances in High Energy Physics 2013 (2013).

[8] G. Wallerstein et al. "Synthesis of the elements in stars: forty years of progress". In: Rev. Mod. Phys. 69 (1997), 995.

[9] W. R. Hix and F.-K. Thielemann. "Silicon Burning. I. Neutronization and the Physics of Quasi-Equilibrium". In: Astrophysical Journal 460 (1996), 869.

[10] E. M. Burbidge et al. "Synthesis of the Elements in Stars". In: Rev. Mod. Phys. 29 (1957), 547.

[11] M. Busso, R. Gallino, and G. J. Wasserburg. "Nucleosynthesis in Asymptotic Giant Branch Stars: Relevance for Galactic Enrichment and Solar System Formation". In: Annual Review of Astronomy and Astrophysics 37 (1999), 239.

[12] J. J. Cowan and F. Thielemann. "r-process nucleosynthesis in supernovae". In: Physics Today (2004).

[13] F. Kappeler, H. Beer, and K. Wisshak. "s-process nucleosynthesis-nuclear physics and the classical model". In: Reports on Progress in Physics 52 (1989), 945.

[14] A. G. W. Cameron. "Photobeta Reactions in Stellar Interiors". In: Astrophysical Journal 130 (1959), 452.

[15] J.N. Bahcall. "Theory of Bound-State Beta Decay". In: Phys. Rev. 124 (2 1961), 495.

[16] J.N. Bahcall. "Electron Capture in Stellar Interiors". In: Astrophysical Journal 139 (1964), 318.

[17] K. Blaum, Yu. N. Novikov, and G. Werth. "Penning traps as a versatile tool for precise experiments in fundamental physics". In: Contemp. Phys. 51 (2010), 149.

[18] J. Lesgourgues and S. Pastor. "Neutrino Mass from Cosmology". In: Advances in High Energy Physics 34 (2012), 608515.

[19] N. Palanque Delabrouille et al. "Neutrino masses and cosmology with Lyman-alpha forest power spectrum". In: Journal of Cosmology and Astroparticle Physics 2015 (2015), 011.

[20] A. Aghamousa et al. "The DESI Experiment Part I: Science,Targeting, and Survey Design". In: (2016). arXiv: 1611.00036 [`astro-ph.IM`].

[21] A.S. Barabash. "Brief review of double beta decay experiments". In: (2017). arXiv: 1702.06340 [`nucl-ex`].

[22] G. Pagliaroli, F. Rossi-Torres, and F. Vissani. "Neutrino mass bound in the standard scenario for supernova electronic antineutrino emission". In: Astroparticle Physics 33 (2010), 287.

[23] S. Pascoli and S.T. Petcov. "The SNO solar neutrino data, neutrinoless double beta-decay and neutrino mass spectrum". In: Physics Letters B 544 (2002), 239.

[24] K.A. Olive et al. "Review of Particle Physics". In: Chinese Physics C 38 (2014), 090001.

[25] F.L. Wilson. "Fermi's Theory of Beta Decay". In: American Journal of Physics 36 (1968), 1150.

[26] G. Drexlin et al. "Current Direct Neutrino Mass Experiments". In: Advances in High Energy Physics 2013 (2013), 39.

[27] E.W. Otten and C. Weinheimer. "Neutrino mass limit from tritium β-decay". In: Reports on Progress in Physics 71 (2008), 086201.

[28] A. De Rújula and M. Lusignoli. "Calorimetric measurements of 163Holmium decay as tools to determine the electron neutrino mass". In: Physics Letters B 118 (1982), 429.

[29] C. Hassel et al. "Recent Results for the ECHo Experiment". In: Journal of Low Temperature Physics 184 (2016), 910.

[30] L. M. Langer and R. J. D. Moffat. "The Beta-Spectrum of Tritium and the Mass of the Neutrino". In: Phys. Rev. 88 (1952), 689.

[31] A. Osipowicz et al. "KATRIN: A Next generation tritium beta decay experiment with sub-eV sensitivity for the electron neutrino mass". In: (2001). arXiv: hep-ex/0109033 [hep-ex].

[32] KATRIN Collaboration. "KATRIN design report 2004". Tech. rep. 51.54.01; LK 01; Auch: NPI ASCR Rez EXP-01/2005; MS-KP-0501. 2005. 245 pp.

[33] S. Bauer et al. "Next generation KATRIN high precision voltage divider for voltages up to 65kV". In: Journal of Instrumentation 8 (2013), P10026.

[34] F. Gatti. "Microcalorimeter measurements". In: Nucl. Phys. B Proc. Suppl. 91 (2001), 293.

[35] M. Sisti, C. Arnaboldi, C. Brofferio, et al. "New limits from the Milano neutrino mass experiment with thermal microcalorimeters". In: Nucl. Instrum. Methods A 520 (2004), 125.

[36] S. Hamzeloui et al. "Precision mass ratio of ^{3}He$^+$ to HD$^+$". In: Phys. Rev. A 96 (2017), 060501.

[37] D. A. Nesterenko et al. "Direct determination of the atomic mass difference of ^{187}Re and ^{187}Os for neutrino physics and cosmochronology". In: Phys. Rev. C 90 (2014), 042501.

[38] S. Eliseev et al. "Direct Measurement of the Mass Difference of ^{163}Ho and ^{163}Dy Solves the Q-Value Puzzle for the Neutrino Mass Determination". In: Phys. Rev. Lett. 115 (2015), 062501.

[39] P.A. Baisden et al. "Measurement of the half-life of ^{163}Ho". In: Phys. Rev. C 28 (1983), 337.

[40] A. Rischka. "The First Direct Q_{EC} Measurement in ^{163}Ho and the Development of the High-Precision Mass Spectrometer PENTATRAP for Neutrino Physics". PhD thesis. University of Heidelberg, Germany, 2018.

[41] G. Audi, A. H. Wapstra, and C. Thibault. "The Ame2003 atomic mass evaluation: (II). Tables, graphs and references". In: Nuclear Physics A 729 (2003), 337.

[42] Yu. Novikov et al. "Search for new candidates for the neutrino-oriented mass determination by electron-capture". CERN-INTC-2008-012/INTC-P-242. 2008.

[43] S. Eliseev et al. "Direct mass measurements of ^{194}Hg and ^{194}Au: A new route to the neutrino mass determination?" In: Physics Letters B 693 (2010), 426.

[44] A. Kankainen et al. "Mass measurements of neutron-deficient nuclides close to $A = 80$ with a Penning trap". In: The European Physical Journal A - Hadrons and Nuclei 29 (2006), 271.

[45] Ch. Böhm et al. "Evolution of nuclear ground-state properties of neutron-deficient isotopes around $Z = 82$ from precision mass measurements". In: Phys. Rev. C 90 (2014), 044307.

[46]   B. J. Mount, M. Redshaw, and E. G. Myers. "Q value of ^{115}In $\rightarrow$ ^{115}Sn($3/2^+$): the lowes known energy β decay". In: Phys. Rev. Lett. 103 (2009), 122502.

[47]   A. Sonzogni. "Nuclear Data Sheets for $A = 134$". In: Nuclear Data Sheets 103 (2004), 1.

[48]   C. Reich. "Nuclear Data Sheets for $A = 159$". In: Nuclear Data Sheets 113 (2012), 157.

[49]   S. Eliseev et al. "Search for β-transitions with the lowest decay energy for a determination of the neutrino mass". CERN-INTC-2014-038/INTC-P-410. 2014.

[50]   "Center for Nuclear Studies". URL: http://www.nndc.bnl.gov.

[51]   G. Audi et al. "The NUBASE2016 evaluation of nuclear properties". In: Chinese Physics C 41 (2017), 030001.

[52]   D.E. Groom et al. "Review of Particle Physics". In: The European Physical Journal C15 (2000), 1.

[53]   T. Asaka and M. Shaposhnikov. "The νMSM, dark matter and baryon asymmetry of the universe". In: Physics Letters B 620 (2005), 17.

[54]   A. Merle. "keV neutrino model building". In: International Journal of Modern Physics D 22 (2013), 1330020.

[55]   S. Dodelson and L. M. Widrow. "Sterile neutrinos as dark matter". In: Phys. Rev. Lett. 72 (1994), 17.

[56]   S. Tremaine and J. E. Gunn. "Dynamical Role of Light Neutral Leptons in Cosmology". In: Phys. Rev. Lett. 42 (1979), 407.

[57]   A. Boyarsky, D. Iakubovskyi, and O. Ruchayskiy. "Next decade of sterile neutrino studies". In: Physics of the Dark Universe 1 (2012). Next Decade in Dark Matter and Dark Energy, 136.

[58]   E. Aprile et al. "Dark Matter Results from 225 Live Days of XENON100 Data". In: Phys. Rev. Lett. 109 (2012), 181301.

[59]   D. S. Akerib et al. "First Results from the LUX Dark Matter Experiment at the Sanford Underground Research Facility". In: Phys. Rev. Lett. 112 (2014), 091303.

[60]   R.E. Shrock. "New tests for and bounds on neutrino masses and lepton mixing". In: Physics Letters B 96 (1980), 159.

[61]   J.J. Simpson. "Evidence of Heavy-Neutrino Emission in Beta Decay". In: Phys. Rev. Lett. 54 (17 1985), 1891.

[62]   E. Holzschuh et al. "Search for heavy neutrinos in the β-spectrum of ^{63}Ni". In: Physics Letters B 451 (1999), 247.

[63]   D. R. Morrison. "The rise and fall of the 17-keV neutrino". In: Nature 366 (1993), 29.

[64]   O. Dragoun and D. Venos. "Constraints on the active and sterile neutrino masses from beta-ray spectra: past, present and future". In: Open Physics Journal 3 (2016), 73.

[65] P. E. Filianin et al. "On the keV sterile neutrino search in electron capture". In: Journal of Physics G: Nuclear and Particle Physics 41 (2014), 095004.

[66] O. Moreno, E. Moya de Guerra, and M. R. Medrano. "Warm dark matter sterile neutrinos in electron capture and beta decay spectra". In: Adv. High Energy Phys. 2016 (2016), 6318102.

[67] G.C. Rodrigues et al. "Systematic calculation of total atomic energies of ground state configurations". In: Atomic Data and Nuclear Data Tables 86 (2004), 117.

[68] W.R. Johnson and G. Soff. "The lamb shift in hydrogen-like atoms, $1 \leqslant Z \leqslant 110$". In: Atomic Data and Nuclear Data Tables 33 (1985), 405.

[69] A. N. Artemyev et al. "QED calculation of the $n = 1$ and $n = 2$ energy levels in He-like ions". In: Phys. Rev. A 71 (2005), 062104.

[70] W.A. Fowler, G.R. Caughlan, and B.A. Zimmerman. "Thermonuclear Reaction Rates". In: Annual Review of Astronomy and Astrophysics 5 (1967), 525.

[71] J. Engel and J. Menéndez. "Status and future of nuclear matrix elements for neutrinoless double-beta decay: a review". In: Reports on Progress in Physics 80 (2017), 046301.

[72] B. Singh et al. "Review Of $\log ft$-values in β-decay". In: Nuclear Data Sheets 84 (1998), 487.

[73] S. Raman and N. B. Gove. "Rules for Spin and Parity Assignments Based on $\log ft$ Values". In: Phys. Rev. C 7 (5 1973), 1995.

[74] R. Daudel, M. Jean, and M. Lecoin. "On the possible existence of a particular type of radioactivity phenomenon of creation electrons". In: J. Phys. Radium 8 (1947), 238.

[75] K. Takahashi and K. Yokoi. "Nuclear β-decays of highly ionized heavy atoms in stellar interiors". In: Nuclear Physics A 404 (1983), 578.

[76] K. Takahashi and K. Yokoi. "Beta-decay rates of highly ionized heavy atoms in stellar interiors". In: Atomic Data and Nuclear Data Tables 36 (1987), 375.

[77] K. Takahashi et al. "Bound-state beta decay of highly ionized atoms". In: Phys. Rev. C 36 (1987), 1522.

[78] Y. A. Litvinov and F. Bosch. "Beta decay of highly charged ions". In: Reports on Progress in Physics 74 (2011), 016301.

[79] J.N. Bahcall. "Electron Capture in Stellar Interiors". In: The Astrophysical Journal 139 (1964), 318.

[80] J.N. Bahcall. "Electron Capture and Nuclear Matrix Elements of ^{7}Be". In: Phys. Rev. 128 (1962), 1297.

[81] G. M. Fuller, W. A. Fowler, and M. J. Newman. "Stellar weak interaction rates for intermediate mass nuclei. III - Rate tables for the free nucleons and nuclei with $A = 21$ to $A = 60$". In: The Astrophysical Journal Supplement Series 48 (1982), 279.

[82] H. G. Dehmelt. "Experiments with an isolated subatomic particle at rest". In: Rev. Mod. Phys. 62 (1990), 525.

[83] S. Earnshaw. "On the nature of the molecular forces which regulate the constitution of the luminiferous ether". In: Trans. Camb. Phil. Soc. 7 (1842), 97.

[84] L. S. Brown and G. Gabrielse. "Geonium theory: Physics of a single electron or ion in a Penning trap". In: Rev. Mod. Phys. 58 (1986), 233.

[85] K. Blaum et al. "Carbon clusters for absolute mass measurements at ISOLTRAP". In: The European Physical Journal A - Hadrons and Nuclei 15 (2002), 245.

[86] A. Kellerbauer et al. "From direct to absolute mass measurements: A study of the accuracy of ISOLTRAP". In: The European Physical Journal D - Atomic, Molecular, Optical and Plasma Physics 22 (2003), 53.

[87] M. Block et al. "Towards direct mass measurements of nobelium at SHIPTRAP". In: The European Physical Journal D 45 (2007), 39.

[88] K. Blaum et al. "Recent developments at ISOLTRAP: towards a relative mass accuracy of exotic nuclei below 10^{-8}". In: Journal of Physics B: Atomic, Molecular and Optical Physics 36 (2003), 921.

[89] P. W. Anderson. "Theory of Flux Creep in Hard Superconductors". In: Phys. Rev. Lett. 9 (1962), 309.

[90] Ch.E. Roux. "High-resolution mass spectrometry: the trap design and detection system of pentatrap and new Q-values for neutrino studies". PhD thesis. University of Heidelberg, Germany, 2012.

[91] J. Ketter et al. "First-order perturbative calculation of the frequency-shifts caused by static cylindrically-symmetric electric and magnetic imperfections of a Penning trap". In: International Journal of Mass Spectrometry 358 (2014), 1.

[92] G. Gabrielse, L. Haarsma, and S.L. Rolston. "Open-endcap Penning traps for high precision experiments". In: International Journal of Mass Spectrometry and Ion Processes 88 (1989), 319.

[93] M. Kretzschmar. "Calculating damping effects for the ion motion in a Penning trap". In: The European Physical Journal D 48 (2008), 313.

[94] S. George et al. "Damping effects in Penning trap mass spectrometry". In: International Journal of Mass Spectrometry 299 (2011), 102.

[95] S. Eliseev et al. "A phase-imaging technique for cyclotron-frequency measurements". In: Applied Physics B: Lasers and Optics 114 (2014), 107.

[96] G. Gräff, H. Kalinowsky, and J. Traut. "A direct determination of the proton electron mass ratio". In: Zeitschrift für Physik A Atoms and Nuclei 297 (1980), 35.

[97] M. König et al. "Quadrupole excitation of stored ion motion at the true cyclotron frequency". In: International Journal of Mass Spectrometry and Ion Processes 142 (1995), 95.

[98] M. Kretzschmar. "The Ramsey method in high-precision mass spectrometry with Penning traps: Theoretical foundations". In: International Journal of Mass Spectrometry 264 (2007), 122.

[99] S. George et al. "Ramsey Method of Separated Oscillatory Fields for High-Precision Penning Trap Mass Spectrometry". In: Phys. Rev. Lett. 98 (2007), 162501.

[100] S. George et al. "The Ramsey method in high-precision mass spectrometry with Penning traps: Experimental results". In: International Journal of Mass Spectrometry 264 (2007), 110.

[101] S. Hofmann et al. "New results on elements 111 and 112". In: The European Physical Journal A - Hadrons and Nuclei 14 (2002), 147.

[102] E. Minaya Ramirez et al. "Direct Mapping of Nuclear Shell Effects in the Heaviest Elements". In: Science 337 (2012), 1207.

[103] M. Dworschak et al. "Penning trap mass measurements on nobelium isotopes". In: Phys. Rev. C 81 (2010), 064312.

[104] A. Chaudhuri et al. "Carbon-cluster mass calibration at SHIPTRAP". In: The European Physical Journal D 45 (2007), 47.

[105] S.M. Rahaman. "First on-line mass measurements at SHIPTRAP and mass determinations of neutron-rich Fr and Ra isotopes at ISOLTRAP". PhD thesis. University of Heidelberg, Germany, 2005.

[106] M. Block et al. "Penning trap mass measurements of transfermium elements with SHIPTRAP". In: Hyperfine Interactions 196 (2010), 225.

[107] G. Savard. "A new cooling technique for heavy ions in a Penning trap". In: Physics Letters A 158 (1991), 247.

[108] H. Raimbault-Hartmann et al. "A cylindrical Penning trap for capture, mass selective cooling, and bunching of radioactive ion beams". In: Nuclear Instruments and Methods in Physics Research Section B: Beam Interactions with Materials and Atoms 126 (1997), 378.

[109] M. Höcker, R. Rana, and E.G. Myers. "Atomic masses of ^{82,83}Kr and ^{131,134}Xe". In: Phys. Rev. A 88 (2013), 052502.

[110] E. Minaya Ramirez. "An Investigation of the Accuracy of the PI-ICR Technique at SHIPTRAP by a Measurement of the Mass Difference between ^{132}Xe and ^{131}Xe". In: *Proceedings of the Conference on Advances in Radioactive Isotope Science (ARIS2014)*.

[111] V. Mocko, W. Taylor, F. Nortier, et al. "Isolation of ^{163}Ho from dysprosium target material by HPLC for neutrino mass measurements". In: Radiochimica Acta 103 (2015), 577.

[112] R.T. Birge. "The Calculation of Errors by the Method of Least Squares". In: Phys. Rev. 40 (1932), 207.

[113] P. Filianin et al. "The decay energy of the pure s-process nuclide ^{123}Te". In: Physics Letters B 758 (2016), 407.

[114] C. Droese et al. "Investigation of the magnetic field fluctuation and implementation of a temperature and pressure stabilization at SHIPTRAP". In: Nuclear Instruments and Methods in Physics Research Section A: Accelerators, Spectrometers, Detectors and Associated Equipment 632 (2011), 157.

[115] M. Goncharov. "High-precision Penning-trap mass spectrometry at SHIPTRAP and PENTATRAP for neutrino physics research". PhD thesis. University of Heidelberg, Germany, 2014.

[116] C. Yazidjian. "A new detector setup for ISOLTRAP and test of the Isobaric multiplet mass equation". 2006.

[117] E. Kugler et al. "The new CERN-ISOLDE on-line mass-separator facility at the PS-Booster". In: Nuclear Instruments and Methods in Physics Research Section B: Beam Interactions with Materials and Atoms 70 (1992), 41.

[118] Herfurth F. et al. "A linear radiofrequency ion trap for accumulation, bunching, and emittance improvement of radioactive ion beams". In: Nuclear Instruments and Methods in Physics Research Section A: Accelerators, Spectrometers, Detectors and Associated Equipment 469 (2001), 254.

[119] R. N. Wolf et al. "ISOLTRAP's multi-reflection time-of-flight mass separator/spectrometer". In: International Journal of Mass Spectrometry 349-350 (2013), 123.

[120] F. Wienholtz et al. "Mass-selective ion ejection from multi-reflection time-of-flight devices via a pulsed in-trap lift". In: International Journal of Mass Spectrometry 421 (2017), 285.

[121] F. Wienholtz et al. "Towards ultrahigh-resolution multi-reflection time-of-flight mass spectrometry at ISOLTRAP". In: Physica Scripta 2015 (2015), 014068.

[122] S. Rothe et al. "Laser ion beam production at CERN-ISOLDE: New features – More possibilities". In: Nuclear Instruments and Methods in Physics Research Section B: Beam Interactions with Materials and Atoms 376 (2016), 91.

[123] E. Hagebo et al. "New production systems at ISOLDE". In: Nuclear Instruments and Methods in Physics Research Section B: Beam Interactions with Materials and Atoms 70 (1992), 165.

[124] W.J. Huang et al. "The AME2016 atomic mass evaluation (I). Evaluation of input data; and adjustment procedures". In: Chinese Physics C 41 (2017), 030002.

[125] A. Welker et al. "Precision electron-capture energy in ^{202}Pb and its relevance for neutrino mass determination". In: The European Physical Journal A 53 (2017), 153.

[126] G. Audi et al. "The Ame2012 atomic mass evaluation". In: Chinese Physics C 36 (2012), 1287.

[127] R. L. Brodzinski and D. C. Conway. "Decay of Rhenium-187". In: Phys. Rev. 138 (1965), 1368.

[128] E. Huster and H. Verbeek. "Das β-Spektrum des natürlichen Rhenium 187". In: Zeitschrift für Physik 203 (1967), 435.

[129] K. Ashktorab, J. W. Jänecke, and F. D. Becchetti. "Beta decay of ^{187}Re and cosmochronology". In: Phys. Rev. C 47 (1993), 2954.

[130] E. Cosulich et al. "Detection of 187Re beta decay with a cryogenic microcalorimeter. Preliminary results". In: Physics Letters B 295 (1992), 143.

[131] A. Alessandrello et al. "Bolometric measurements of beta decay spectra of 187Re with crystals of silver perrhenate". In: Physics Letters B 457 (1999), 253.

[132] M. Galeazzi et al. "End-point energy and half-life of the ^{187}Re β-decay". In: Phys. Rev. C 63 (2000), 014302.

[133] C. Arnaboldi et al. "Bolometric Bounds on the Antineutrino Mass". In: Phys. Rev. Lett. 91 (2003), 161802.

[134] E. Ferri et al. "The Status of the MARE Experiment with ^{187}Re and ^{163}Ho Isotopes". In: Physics Procedia 61 (2015), 227.

[135] A. Nucciotti, E. Ferri, and O. Cremonesi. "Expectations for a new calorimetric neutrino mass experiment". In: Astroparticle Physics 34 (2010), 80.

[136] J. Repp et al. "PENTATRAP: a novel cryogenic multi-Penning-trap experiment for high-precision mass measurements on highly charged ions". In: Applied Physics B 107 (2012), 983.

[137] A. Faessler and F. Šimkovic. "Improved description of one- and two-hole excitations after electron capture in ^{163}Ho and the determination of the neutrino mass". In: Phys. Rev. C 91 (2015), 045505.

[138] A. De Rújula and M. Lusignoli. "The calorimetric spectrum of the electron-capture decay of 163Ho. The spectral endpoint region". In: Journal of High Energy Physics 2016 (2016), 15.

[139] L. Gastaldo et al. "The electron capture in ^{163}Ho experiment − ECHo". In: The European Physical Journal Special Topics 226 (2017), 1623.

[140] B. Alpert et al. "HOLMES". In: The European Physical Journal C 75 (2015), 112.

[141] M. P. Croce et al. "Integration of Radioactive Material with Microcalorimeter Detectors". In: Journal of Low Temperature Physics 176 (2014), 1009.

[142] A. Alessandrello et al. "New limits on naturally occurring electron capture of ^{123}Te". In: Phys. Rev. C 67 (2003), 014323.

[143] M. Wang et al. "The Ame2012 atomic mass evaluation". In: Chinese Physics C 36 (2012), 1603.

[144] N. G. Saha. "Ionization in the solar chromosphere". In: Philosophical Magazine 40 (1920), 472.

[145] K. Takahashi, K. Blaum, and Yu. Novikov. "Synthesis of the s-only ^{122,123,124}Te Isotopes and the Selective Depletion of ^{123}Te by Electron Capture Process in Massive Stars". In: The Astrophysical Journal 819 (2016), 118.

[146] M. S. Basunia. "Nuclear Data Sheets for $A = 187$". In: Nuclear Data Sheets 110 (2009), 999.

[147] "Planck 2015 results - XIII. Cosmological parameters". In: Astronomy and Astrophysics 594 (2016), A13.

[148] D. Clayton. "Cosmoradiogenic Chronologies of Nucleosynthesis". In: Astrophysical Journal 139 (1964), 637.

[149] K. Takahashi. "The ^{187}Re-^{187}Os cosmochronometry - the latest developments". In: AIP Conference Proceedings 425 (1998), 616.

[150] M. Jung et al. "First observation of bound-state β^- decay". In: Phys. Rev. Lett. 69 (1992), 2164.

[151] Ch. Böhm et al. "An ultra-stable voltage source for precision Penning-trap experiments". In: Nuclear Instruments and Methods in Physics Research Section A: Accelerators, Spectrometers, Detectors and Associated Equipment 828 (2016), 125.

[152] S. Rainville et al. "A direct test of $E = mc^2$". In: Nature 438 (2005), 1096.

[153] F. Köhler et al. "Isotope dependence of the Zeeman effect in lithium-like calcium". In: Nature Communications 7 (2016), 10246.

[154] S. Eliseev, Y.N. Novikov, and K. Blaum. "Penning-trap mass spectrometry and neutrino physics". In: Annalen der Physik 525 (2013), 707.

List of the author's publications

1. **P. E. Filianin**, K. Blaum, S.A. Eliseev, L. Gastaldo, Yu. N. Novikov, V. M. Shabaev, I. I. Tupitsyn, and J. Vergados. "On the keV sterile neutrino search in electron capture". In: Journal of Physics G 41 (2014) 095004 – reference [65];

2. D. A. Nesterenko, S. Eliseev, K. Blaum, M. Block, S. Chenmarev, A. Dörr, C. Droese, **P. E. Filianin**, M. Goncharov, E. Minaya Ramirez, Yu. N. Novikov, L. Schweikhard, and V. V. Simon. "Direct determination of the atomic mass difference of ^{187}Re and ^{187}Os for neutrino physics and cosmochronology". In: Phys. Rev. C 90 (2014) 042501 – reference [37];

3. S. Eliseev, K. Blaum, M. Block, S. Chenmarev, H. Dorrer, Ch. E. Düllmann, C. Enss, **P. E. Filianin**, L. Gastaldo, M. Goncharov, U. Köster, F. Lautenschläger, Yu. N. Novikov, A. Rischka, R. X. Schüssler, L. Schweikhard, and A. Türler. "Direct measurement of the mass difference of ^{163}Ho and ^{163}Dy solves the Q-value puzzle for the neutrino mass determination". In: Physical Review Letters 115 (2015) 062501 – reference [38];

4. **P. Filianin**, S. Schmidt, K. Blaum, M. Block, S. Eliseev, F. Giacoppo, M. Goncharov, F. Lautenschlaeger, Yu. Novikov, and K. Takahashi. "The decay energy of the pure s-process nuclide 123Te". In: Physics Letters B 758 (2016) 407 – reference [65];

5. A. Welker, **P. Filianin**, N. A. S. Althubiti, D. Atanasov, K. Blaum, T. E. Cocolios, S. Eliseev, F. Herfurth, S. Kreim, D. Lunney, V. Manea, D. Neidherr, Yu. Novikov, M. Rosenbusch, L. Schweikhard, F. Wienholtz, R.N. Wolf, and K. Zuber. "Precision electron-capture energy in ^{202}Pb and its relevance for neutrino mass determination". In: The European Physical Journal A53 (2017) 153 – reference [125];

6. L. Gastaldo, K. Blaum, K. Chrysalidis, T. Day Goodacre, A. Domula, M. Door, H. Dorrer, Ch.E. Düllmann, K. Eberhardt, S. Eliseev, C. Enss, A. Faessler, **P. Filianin**, A. Fleischmann, D. Fonnesu, L. Gamer, R. Haas, C. Hassel, D. Hengstler, J. Jochum, K. Johnston, U. Kebschull, S. Kempf, T. Kieck, U. Köster, S. Lahiri, M. Maiti, F. Mantegazzini, B. Marsh, P. Neroutsos, Yu. N. Novikov, P. C. O. Ranitzsch, S. Rothe, A. Rischka, A. Saenz, O. Sander, F. Schneider, S. Scholl, R.X. Schüssler, Ch. Schweiger, F. Simkovic, T. Stora, Z. Szücs, A. Türler, M. Veinhard, M. Weber, M. Wegner, K. Wendt, and K. Zuber. "The electron capture in ^{163}Ho experiment – ECHo". In: The European Physical Journal Special Topics 226 (2017) 1623 – reference [139].

Acknowledgements